MISCIBILITY AND PHASE SEPARATION OF POLYMER BLENDS UNDER NORMAL AND PRESSURISED CONDITIONS

by

GUO WEIQING

A thesis submitted for the degree of Doctor of Philosophy
of the University of London

Department of Chemical Engineering
and Chemical Technology
Imperial College of Science, Technology and Medicine
London SW7

June 1989

To my late mother

ABSTRACT

This thesis examines the miscibility and phase separation of two polymer blends: Polystyrene with tetra–methyl bis–phenol A poly carbonate and poly(ether sulphone) with Poly(ethylene oxide). A quick–release pressure cell intended to perform pressure jumps and to study the pressure effects on polymer blends is also described. The subsequent use of this cell in the study of polymer blends is examined.

Measurements using techniques including DSC, light scattering and microscopy have confirmed the miscibility of these two blends. Lower critical solution temperature behaviour is noted in both mixtures. The effects of heating rates, molecular weights and the film thickness on the LCST of TMPC/PS mixtures are examined. The kinetics of crystallization behaviour of PEO in PES/PEO mixtures are studied. Using the melting depression method a negative interaction parameter is obtained.

The data from spinodal decomposition in both mixtures is analysed using the Cahn–Hillard theory. This theory satisfactorily predicts the observed exponential growth of the wavevector maximum during the early stages of spinodal decomposition, but fails to predict the wavevector cut–off, Q_c, and the apparent reverse temperature dependence. The C–H theory fails to account for the non–exponential growth of the wavevector maximum and its movement to smaller wavevectors during the later stages. The results are compared with the predictions made by other theories, such as Binder, Cook and Van Aartsen.

A diamond anvil quick–release pressure cell was designed and manufactured. The pressure calibration of the cell using three techniques including the ruby scale was conducted. A pressure calibration curve is produced for the cell. A special heater and a new light scattering apparatus was

made for the cell. Using the cell pressure effects on the cloud points of the polystyrene with poly(vinyl methyl ether) mixtures were studied. Phase separation processes in solution chlorinated polyethylene with ethylene–vinyl acetate copolymer under pressure are also examined.

ACKNOWLEDGEMENTS

I would like to thank my supervisor, Dr J.S. Higgins, for her constant support, supervision and constructive criticisms, without which this project may not have been possible to implement.

I would also like to thank:

Drs D.A. Young, M.D. Carabine (Chemical Engineering) and M.H.R. Hutchinson, J. Zhou (Physics) for their help with the ruby scale calibration.

Dr D.M. Adams (The University of Leicester) for the construction of the pressure cell.

Mr R.K.C. Oxenham, Mr M.Dix (Electronics) and the staff in the workshop for the construction of the laser light scattering instrument.

Mr I. Drummond (Analytical Services) for the elemental analysis of the solution chlorinated polyethylene.

Mr P. Armit and his colleagues of Postgraduate Services for general help in the course of the project.

Mrs E. Tustin for typing the thesis with great skill and patience.

I am also very grateful to my colleagues in the Polymer Group for their moral support and good cheer, which made my Ph.D. not merely an academic experience.

I am greatly indebted to my family for their encouragement, patience and love.

Finally, the financial support of The British Council and The Government of The People's Republic of China is greatly appreciated.

CONTENTS

Abstract		i
Acknowledgements		iii
Contents		iv
List of Figures		
List of Tables		
Chapter 1	**Introduction**	1
1.1	Basic thermodynamics of polymer miscibility	1
1.2	Ways of making miscible blends	5
1.3	Techniques of studying miscibility	8
1.4	A general survey of pressure effects on polymers and their mixtures	16
1.5	Studies of phase separation in polymer blends	19
1.6	Objective of this project	25
Chapter 2	**Thermodynamic theory**	26
2.1	The Flory–Huggins theory	26
2.2	The equation of state	32
2.3	Theoretical treatments of pressure effects on polymer miscibility	41
2.4	Melting point depression	44
Chapter 3	**Theories of kinetics of phase separation**	47
3.1	Introduction	47
3.2	Phase separation in polymer mixtures	47
3.3	Characteristics of spinodal decomposition	51

3.4	Kinetics of spinodal decomposition	52
3.5	Shortcomings of the Cahn–Hillard theory	57
3.6	The extended theories	58
Chapter 4	**Materials and Experimental**	63
4.1	Choice of system	63
4.2	Materials	65
4.3	Blend Preparation	67
4.4	Methods of establishing miscibility and cloud points	69
Chapter 5	**Results and Discussion**	80
5.1	TMPC/PS system	80
5.2	PES/PEO system	100
Chapter 6	**Optical quick release pressure cell**	119
6.1	Introduction	119
6.2	Design requirements	119
6.3	Pressure cells and the choice	124
6.4	Description of the cell	125
6.5	Some problems of the cell	128
6.6	Design of the heater	129
6.7	Pressure calibration of the DAC cell	130
6.8	Characteristics of the ring heater	140
6.9	Characteristics of the optical system	144
Chapter 7	**Preliminary experiments with the use of the DAC cell**	147
7.1	Pressure effects on the cloud points of PS/PVME system	147
7.2	Experiments on mixtures of SCPE/EVA system	148

Chapter 8 Conclusions and Recommendations 159

8.1 TMPC/PS system 159

8.2 PES/PEO system 160

8.3 Studies with the pressure cell 162

References 165

LIST OF FIGURES

Fig.1.1	Possible free energy of mixing diagrams for binary mixtures at temperature, To.	3
Fig.1.2	A schematic relation between various parameters in DMTA.	11
Fig.1.3	A schematic scattering diagram.	14
Fig.1.4	Ranges accessible to SANS, SAXS and SALS.	15
Fig.1.5	A schematic diagram of a temperature jump.	21
Fig.1.6	A schematic illustration of a pressure jump ($P_2 > P_1$).	24
Fig.2.1	Lattice diagrams used in the Flory–Huggins theory.	26
Fig.3.1	The spinodal defined by the locus of temperatures on the phase diagram at which $\frac{\partial^2 G}{\partial \phi^2} = 0$.	48
Fig.3.2	Schematic drawing of time evolution of composition profiles for nucleation and growth and spinodal decomposition.	49
Fig.3.3	Three stages of spinodal decomposition	51
Fig.4.1	The experimental set–up for freeze–drying.	68
Fig.4.2	A schematic drawing of the assembly frame of the He/Ne laser.	74
Fig.4.3	A schematic drawing of the assembly base of the diamond anvil pressure cell.	74
Fig.4.4	A schematic illustration of the newly–built heating block.	75

Fig.4.5	A schematic illustration of the light scattering equipment.	76
Fig.4.6	A typical plot of determination of cloud points.	77
Fig.5.1	Plots of DSC thermograms of heat capacities against temperature for blends of TMPC with PS.	81
Fig.5.2	Plots of glass transition temperature of TMPC/PS–5 mixtures.	81
Fig.5.3	Effect of heating rates on the cloud points of TMPC/PS (50/50) mixture.	84
Fig.5.4	Cloud point curves for TMPC/PS mixtures with different molecular weights of PS, determined by using the light scattering technique.	84
Fig.5.5	Effects of film thicknesses on the cloud points of TMPC/PS–5 (50/50) mixture.	85
Fig.5.6	Cloud points determined by microscopic methods.	87
Fig.5.7	Photographic pictures of the phase separated TMPC/PS–5 mixture at different temperatures and times.	88
Fig.5.8	A typical series of I(Q) plots at different times within the spinodal for TMPC/PS–5 (50/50) mixture at 242^{0}C.	89
Fig.5.9	A typical plot of intensity against time for TMPC/PS–5 (50/50) at 242^{0}C.	89
Fig.5.10	A plot of Ln (intensity) against time for the data shown in Fig. 5.9.	90

Fig.5.11	Plots of growth rate R(Q) against Q for TMPC/PS–5 (50/50) mixture at different temperatures.	91
Fig.5.12	Plots of $R(Q)/Q^2$ against Q^2 for TMPC/PS–5 mixture (50/50) at different temperatures.	93
Fig.5.13	The apparent diffusion coefficients D_{app} plotted as a function of temperature for TMPC/PS–5 (50/50) mixture.	95
Fig.5.14	Plot of intercepts $\left[\frac{\partial^2 G}{\partial \phi^2}\right]$ against 1/T obtained from Brereton's results.	99
Fig.5.15	Plot of slopes (= 2K) against temperature obtained from Brereton's results.	99
Fig.5.16	Plots of glass transition temperatures of PES/PEO mixtures.	102
Fig.5.17	The phase boundary of PES/PEO blend.	102
Fig.5.18	Typical plots of intensity against time in the vicinity of spinodal temperature.	104
Fig.5.19	The measured melting temperatures as a function of crystalization temperature.	105
Fig.5.20	A plot of equilibrium melting temperatures against concentration of the PES/PEO (10/90) mixture.	107
Fig.5.21	Plot of ΔT_m against ϕ_1^2.	109
Fig.5.22	Effects of PES on the crystallization behaviour of PEO in the mixture.	110
Fig.5.23	One typical plot of log[ln{–(1–Xn)}] against logt for the 70/30 PEO/PES mixture at different T_c.	111

Fig.5.24	A typical plot of scattered intensity against time for PES/PEO(10/90) mixture during phase separation.	113
Fig.5.25	A plot of ln(intensity) v. time for the plot shown in Fig. 5.24.	113
Fig.5.26	Plots of growth rate R(Q) against Q for the PES/PEO (10/90) mixture at different temperatures.	114
Fig.5.27	A typical plot of $R(Q)/Q^2$ against Q^2 at temperature 87.7°C.	115
Fig.5.28	The apparent diffusion coefficient D_{app} plotted against temperature of phase separation.	116
Fig.6.1	A schematic drawing of the diamond anvil cell.	125
Fig.6.2	The gas flow charter in the operation of DAC.	127
Fig.6.3	A schematic drawing of the ring heater.	130
Fig.6.4	A schematic diagram of the set–up used for the pressure calibration of DAC by the ruby scale.	135
Fig.6.5	The calibration curve provided by the manufacturer.	138
Fig.6.6	Plots of the transition ring size at different pressures.	141
Fig.6.7	The calibration curve obtained from phase transition measurements.	141
Fig.6.8	The relation between voltage applied and the temperature achieved in the ring heater.	142

Fig.6.9	The simulated environment for the measurements of temperature gradient in the ring heater.	142
Fig.6.10	A schematic diagram of temperature control mechanisms of the ring heater.	143
Fig.6.11	Temperature fluctuation after a pressure jump to zero pressure.	144
Fig.6.12	Distortion of scattering angles due to the presence of diamond anvils and a lens.	145
Fig.7.1	The determined cloud points of PS/PVME (50/50) at different pressures.	148
Fig.7.2	The glass transition temperature of SCPE at different chlorine contents.	149
Fig.7.3	The density of SCPE at different chlorine contents.	149
Fig.7.4	a) The cloud point curves of SCPE/EVA 45 mixtures at different chlorination level of SCPE. b) Cloud points of 50/50 SCPE/EVA 45 mixtures against chlorine contents.	151
Fig.7.5	A plot of scattered intensity against time at pressure 800 bar.	154
Fig.7.6	A ln (intensity) against time at pressure 800 bar.	154
Fig.7.7	A plot of R(Q) against Q at pressure 800 bar.	155
Fig.7.8	A plot of $R(Q)/Q^2$ against Q^2 at pressure 800 bar.	155

Fig.7.9 A plot of the apparent diffusion coefficient, D_{app}, against pressure. 157

Fig.7.10 A plot of MK against pressure. 157

Fig.7.11 A plot of D_{app}/MK against pressure . 159

LIST OF TABLES

Table 4.1	Characteristics of polystyrene used	67
Table 4.2	Characteristics of the BS photodiode	76
Table 4.3	Characteristics of the He–Ne laser	76
Table 5.1	Glass transition temperatures of TMPC/PS–5 blends	83
Table 5.2	Effects of heating rates, film thicknesses on cloud points of TMPC/PS–5 (50/50) blends	86
Table 5.3	Effects of molecular weights of PS on the cloud point of TMPC/PS blends	86
Table 5.4	Results obtained from the C–H theory for the spinodal decomposition of a TMPC/PS–5 (50/50) blend	92
Table 5.5	Glass transition temperatures, cloud points and spinodal temperatures for the PES/PEO blends	104
Table 5.6	Equilibrium melting temperatures of the PES/PEO mixtures	107
Table 5.7	Data of overall crystallization study of PES/PEO mixtures	112
Table 5.8	Data of kinetics of phase separation of PES/PEO(10/90) mixture	114
Table 5.9	Parameters used for the calculation of $\frac{\partial^2 G}{\partial \phi^2}$ from the equation of state	118
Table 6.1	Characteristics of window materials used in various optical pressure cells.	120
Table 6.2	Characteristics of chemicals used in the pressure calibration of the DAC	139

Table 7.1 Characteristics of SCPE's and EVA—45 150

Table 7.2 Data of kinetics of phase separation of SCPE51/EVA45(50/50) under pressure 156

Chapter 1

Introduction

Over the years there has been an ever increasing demand for extensive application of polymers, which has provoked the search for new polymeric materials. There are two ways which can be used to meet the increasing demands. One is to make new polymers through polymerisation of novel monomers. The other is to mix the existing numerous polymers to get the materials with desired properties. Due to the higher costs of producing new polymers, mixing of polymers would be a logical approach. Practically, totally miscible polymer blends may not be necessarily desirable. However, a certain amount of mixing between components in polymer mixtures is required in order to have good mechanical properties as discussed in several reviews[1,2]. The basic thermodynamic study of polymer miscibility and the study of phase separation could provide valuable information about these.

1.1 Basic thermodynamics of polymer miscibility

The earliest findings of Dobry and Boyer–Kawenski[3] and Kern and Slocombe[4] in later publications suggested that miscibility of polymers is the exception whilst immiscibility is the rule. Although the number of identified new miscible polymer pairs is increasing and comprehensive lists are presented in reviews by Olabisi[5] and Paul[6], many pairs of these miscible polymers can be simply classified into three categories:

a. polymers of very low molecular weight which no longer have a negligible entropy of mixing,

b. polymers which are chemically almost identical, having a very small unfavourable heat of mixing and

c. polymers which show specific interactions between the component monomers resulting in a favourable heat of mixing.

The last category in the above classification forms the most common and the most important group in the study of polymer miscibility. The importance of specific interaction in these systems has been extensively reviewed[7,8].

Polymer–polymer miscibility is thermodynamically governed by the free energy of mixing which can be described in terms of enthalpy and entropy contributions.

$$\Delta G_m = \Delta H_m - T\Delta S_m \qquad (1.1)$$

where ΔG_m is the free energy of mixing

ΔH_m the enthalpy of mixing

ΔS_m the entropy of mixing and

T is the temperature in Kelvin.

Miscible polymer blends can only occur if the free energy of mixing is less than zero. However, the phase relationship of a particular mixture is governed by the subtle details of the composition dependence of ΔG_m. In Figure (1.1), three typical curves of ΔG_m.v. composition at temperature T_0 are plotted. Curve A characterises the completely immiscible systems where a positive free energy of mixing over all the concentration and temperature range is found. Curve B, with a negative free energy of mixing over the whole concentration and temperature range characterises completely miscible polymer blends. Such systems are rare; a typical example is the blend of polystyrene with poly(phenylene oxide)[9]. Curve C has a negative free energy of mixing with

two minima. Polymer blends with such behaviour are partially miscible systems, which with increasing temperature will separate into two phases. This means that the system has a Lower Critical Solution Temperature (LCST). Most polymer blends exhibit this behaviour.

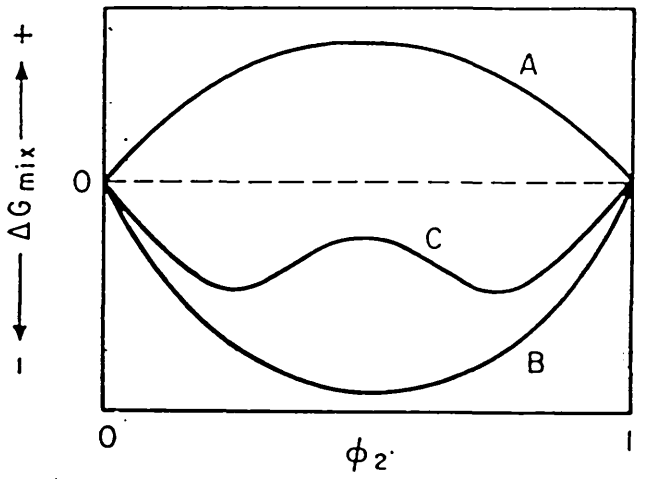


Fig.1.1 Possible free energy of mixing diagrams for binary mixtures at temperature, To.

Thermodynamic treatments of polymer miscibility are an extension of the treatment of polymer solutions. Flory[10,11] and Huggins[12,13] independently were the first to develop a statistical lattice model for calculation of the entropy change on mixing of polymers with solvents. In this model polymer chains are conceptually divided into segments with sizes equal to the lattice size. Through this model a free energy of mixing expression was derived.

$$\frac{\Delta G_m}{RT} = n_1 \ln\phi_1 + n_2 \ln\phi_2 + n_1\phi_2\chi_{12} \qquad (1.2)$$

where ϕ_1 and ϕ_2 are volume fractions of the components, n_1 and n_2 are the

numbers of molecule components and χ_{12} is the Flory–Huggins interaction parameter.

The first two terms in the R.H.S. of Equation (1.2) are entropic and the last term is enthalpic. Due to high molecular weights of polymers the entropic contribution to the free energy of mixing is very small (close to zero). Thus polymer miscibility is mainly determined by the interaction parameter, χ_{12}. Indeed, when this theory was applied to the mixing of polymers[14] one of the main criticisms of this theory was the use of χ_{12}. In the original theory this parameter was assumed only inversely dependent on temperature[10,11]. Experimental evidence has proved that it is concentration as well as temperature dependent. Tompa[14] and Konsingsveld[15] have tried to formulate an empirical concentration dependent interaction parameter in different approaches. These approaches have been widely used in describing binary mixtures.

On the whole, the lattice model was able to provide a qualitatively satisfactory description of the main thermodynamic behaviour of polymer solutions and polymer blends, such as the large deviation from Raoult's law and the Upper Critical Solution Temperature (UCST) behaviour of polymer solutions. However, because of the assumptions made, the theory is only applicable to certain systems[11]. It also failed to explain the LCST behaviour observed in most polymer blends. The failure of this model in those aspects resulted in the abandoning of the whole concept of the lattice model by Flory and his co–workers. The equation of state theory[16,17] was then developed.

In the equation of state theory, hard–core properties are introduced and each pure component is characterised by three reduced variables (V*, T* and P*). A temperature and concentration dependent interaction parameter, X_{12}, is also introduced.

Using the modified equation of state theory, McMaster[18] examined the importance of "free volume" effects on polymer miscibility, which has been neglected in the Flory–Huggins theory, while Patterson[19] demonstrated the importance of the interaction parameter X_{12}. The equation of state theory, being able to predict LCST as well as UCST, is an obvious improvement of the Flory–Huggins theory. Such an improvement was demonstrated by studies of McMaster[18] and Walsh[20,21] and others[22,23]. However, the complexity of the theory has hindered its widespread application and exploration of its potential.

1.2 Ways of making miscible blends

There are three main ways for making homogeneous blends of polymers: mechanical mixing, mixing in a common solvent and *in situ* polymerisation. Mixing in a common solvent has been the commonest method in academic studies, though this method would have very limited industrial application, while the other two methods are more commercially popular.

1.2.1 Mechanical mixing

Mechanical mixing of two polymers to form a blend is probably the most widely used method in industry and of greatest practical importance. However it usually does not make a homogeneous mixture due to the small diffusion coefficients of high polymers and low thermal stability of many polymers. Also many polymer mixtures exhibit phase separation on heating, which prevents molecular mixing at higher temperatures if the temperature used for mixing is above the phase separation temperature of the blend.

Many commercial polymer blends, such as poly(vinyl chloride) mixtures[24,25,26] are prepared in this way since complete homogeneity of a mixture may not be necessary or even desirable.

1.2.2 Mixing in a common solvent

Mixing polymers in a common solvent overcomes the difficulty of the extremely small diffusion coefficient of polymers in mechanical mixing. Thus it is generally assumed[6] that a polymer blend prepared by this method is more likely to be in its equilibrium state than prepared in mechanical mixing. In order to remove the solvent, three methods can be used.

1. **Evaporation:**

This is the commonest method of preparing homogeneous blends in academic studies. Due to the $\Delta\chi$ effect[27] careful selection of the common solvent and careful control of evaporation rate are required to ensure that no phase separation takes place during evaporation. In the case of polystyrene blends with poly(vinyl ether), two phase behaviour was found in blends from various chlorinated solvents whereas single phase behaviour was found for blends from toluene[28]. The disadvantages of this method are:

a. thick films of polymer blends cannot be prepared due to the difficulties of solvent evaporation in thick films and

b. solvents which sometimes bond to polymers are difficult to remove.

2. **Freeze–drying**

This is one of the alternative ways to remove the common solvent. It is assumed that more homogeneous polymer blends can be made by this method. Incompatible polymer blends of polystyrene and poly(methyl methyl acrylate)[29] have been prepared by freeze–drying of their co–solutions in naphthalene.

Normally this method produces finely divided or coarse particular samples which must be processed before testing.

3. **Coprecipitation**

Coprecipitation of polymers from a common solvent into a non–solvent is the quickest way to remove the common solvent. This method is useful when the common solvent has a very high boiling point. The resulting samples prepared from this method are normally particulates which must be pressed for further analysis.

1.2.3 *In situ* polymerisation

In situ polymerisation is the polymerisation of one monomer in the presence of another polymer with different monomer units. It has been extensively used in the preparation of two phase blends, for example high impact polystyrene[1], but has only recently been applied to the preparation of homogeneous blends. It does have many advantages for the preparation of blends where the base polymers are not very thermally stable and have a high T_g or show phase separation on heating which precludes the use of mechanical mixing. However, *in situ* polymerisation does not guarantee homogeneous blends because phase separation may take place during polymerisation.

Samples prepared from these three methods may show different behaviour in measurements due to the different thermodynamic processes involved.

1.3 Techniques of studying miscibility

Optical, mechanical, electrical, morphological and thermodynamic properties of various polymer mixtures are often used as evidence for establishing miscibility. Every method is unique in its approach and has its limitations. Thus normally more than one method are used in establishing miscibility.

1.3.1 Optical clarity

Optical clarity is usually the first indication that two polymers are miscible, though it is not itself a sufficient proof of homogeneity. For example, it can be deceptive in the following circumstances:

1. If the refractive indices of the components in the mixture are very close to each other, Bohn[30] has indicated that transparency by refractive index requires $\Delta n \leq 0.05 - 0.1$.
2. If the dispersed phase has a size smaller than the wavelength of visible light then the amount of scattering will be reduced to such an extent that the mixture appears to be clear. Rosen[31] indicated that the limit of the phase domain is in the order of 0.1 μm or less.
3. If the blend has phase separated into two separate layers or if the film prepared from a blend is too thin, then light will pass through the film without too much scattering from the system.

A clear homogeneous blend of two high molecular weight polymers may phase separate and become cloudy on heating. Therefore its transmission of light decreases and its scattering intensity increases. This can be used as a method of detecting the cloud point of a blend. The usefulness of this technique

is demonstrated by determination of phase boundaries of many polymer blends. Besides light, x–ray or neutron beams which have shorter wavelength can also be used when there is not enough refractive index contrast in the system for light scattering, or when the dispersed phase is very small.

1.3.2 Optical and electron microscopy

Both optical and electron microscopy are widely used in studies of polymer blends. Phase contrast microscopy is preferred in such studies due to its high resolving power for materials with similar refractive indices. It produces coloured pictures of the specimen with two phase blends showing two different colours. However, its resolving power is still limited by the wavelength of light. The minimum spacing which can be resolved by a good microscope is in the order of the wavelength of the light source used. Despite this optical microscopy has been successfully used to examine the miscibility and phase separation of several blends[32,33,34].

The transmission electron microscope (TEM) with a resolution of 10 ~ 20 Å has proved to be a more powerful tool for studies of polymer–polymer miscibility and phase separation. This technique was successfully used in the studies of polymer blends of poly(vinyl chloride) with poly(butyl acrylate)[34] and ethylene–vinyl acetate copolymers with chlorinated polyethylene[33]. However, the problem always exists that the image obtained from the machine may not be a correct reconstruction of the object due to the preparation of samples, the replication method and damage caused by the electron beam. Staining techniques[35] are often required to enhance the contrast of the system.

Scanning electron microscopy[36] can also be applied. In this case the preparation of samples is much easier than for TEM.

1.3.3 Glass transition temperature measurements

A miscible polymer blend which behaves as one homogeneous phase shows a single glass transition temperature, T_g, which is generally between the T_g's of the individual polymers. Thus the detection of a single intermediate glass transition temperature has been practically regarded as a criterion for miscible blends. However, this criterion can be inapplicable or even misleading in the following circumstances:

1. If the quantity of one component in the blend is too small to be detected in the glass transition measurements.
2. If the glass transition temperatures of the two components in the blend are too close to each other to be resolved by the measurements. Depending on the resolution of the technique used in the measurement, a 20°C difference in glass transition temperatures is usually required.

Many attempts have been made to correlate the T_g of the miscible polymer with the blend composition. Several expressions[37,38,39] have been deduced. Among them the Fox equation[37] cited below is the most widely used.

$$\frac{1}{T_g} = \frac{w_1}{T_{g1}} + \frac{w_2}{T_{g2}} \qquad (1.3)$$

where w_1 and w_2 are the weight fractions of the components, T_{g1} and T_{g2} are the glass transition temperatures of the components.

The Fox equation has not been able to quantitatively predict the glass transition temperatures of most miscible polymer blends. In most cases deviations from the theory are obtained. Positive deviations from the theory have been interpreted to be due to some strong specific interactions between components[6].

In the determination of glass transition temperatures, various techniques are available. All the techniques are developed from the nature of the glass transition of polymers. In the following section, some of the main techniques are briefly described.

a. Dynamic Mechanical Thermal Analysis[40] (DMTA)

This technique involves the determination of the dynamic properties of polymers and their mixtures, usually by applying a mechanical sinusoidal stress. Due to the linear viscoelastic behaviour the strain will alternate sinusoidally but will be out of phase with the stress (see Figure 1.2). The phase lag results from

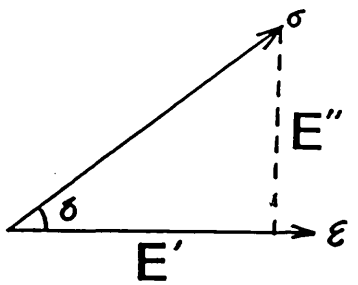


Fig.1.2 A schematic relation between various parameters in DMTA. σ is the stress, ϵ the strain.

the time required for molecular rearrangements and this is associated with the relaxation phenomena. The energy loss per cycle, or damping in the system, can be measured from the loss, defined by

$$\tan \delta = E''/E' \qquad (1.4)$$

where E' is the storage modulus and E'' the loss modulus. A peak in the value of tan δ occurs around the glass transition temperature.

Dynamic mechanical analysis can provide strong evidence of blend homogeneity when a single T_g is detected or inhomogeneity when two T_g's are

detected. It can also be used to estimate the position of phase diagram by examining the samples quenched from different temperatures. Such experiments have been successfully conducted by several authors[32,33].

b. **Dielectric relaxation measurements[41]**

This method is similar to dynamic mechanical measurements except that it exploits the dipole electrical properties of the blend. It is, therefore, inapplicable to a blend of polymers without dipole moments. Inclusions of dipole moments can cause frequency conductivity in the blend while measuring the glass transition temperature. This is more pronounced when the heating scan programme is used. The advantage of dielectric over dynamic relaxation measurements is the easy availability of different frequencies in the machine.

c. **Differential scanning calorimetry (DSC) and differential thermal analysis (DTA)[42]**

DSC and DTA show similar traces for T_g measurements although the property being measured is different. DSC measures the amount of heat required to increase the sample temperature over that required to heat up a reference material (normally an empty pan) to the same temperature. The variation in power necessary to maintain this level during a transition is monitored. DTA measures the difference in temperature between the sample and the reference material when both are heated at the same temperature rate. The merits of DSC over other techniques are the tiny amount of specimen required (about 10 mg) and the easier sample preparation.

DSC has been extensively used in studying polymer–polymer miscibility. It has been particularly useful for measuring the melting point depression of crystalline polymer components in some blends[43,44]. It can also, in principle, be used to study the phase diagram of a mixture as described in the dynamic mechanical measurements.

Among the techniques discussed above, DMTA has the highest resolution. It is believed[45] that DMTA can detect a domain structure at molecular level (~ 100Å).

1.3.4 Other methods

The techniques discussed above are very useful for establishing whether polymers are miscible and observing the structures of polymer blends. However, further detailed information related to the blend may have to rely on other methods.

With the application of Hess's law cycle, inverse gas chromatography[46], vapour absorption[47] and calorimetry[48] can be used to determine the heat of mixing of polymer mixtures, In calorimetric measurements oligomeric polymers are often applied. However all these methods are not very accurate. Reliable results for interaction parameters, χ_{12}, in polymer mixtures were not obtained before the application of scattering techniques, mainly small angle x–ray scattering (SAXS) and small angle neutron scattering (SANS). By using these techniques, dimensions of polymer chains or the second virial coefficient of the mixture can be obtained, from which the interaction parameter, χ_{12}, can be deduced. The details of these applications are discussed by several authors[49,50,51].

Fourier Transform Infra–red spectroscopy (FTIR)[52] and NMR[53] have occasionally been used to examine the molecular nature of specific interaction being responsible for the miscibility of many polymer mixtures, through the observation of band shift of interacting groups involved. Here no particular thermodynamic parameter is measured.

In the study of phase separation of polymer blends, scattering techniques in conjunction with microscopic techniques are widely used. Numerous excellent reviews of small angle light scattering (SALS)[54,55], SAXS[57] and SANS[56] have been published. Here the concept of scattering is described.

If radiation is scattered from two points in a medium a distance D apart (Figure 1.3) then the path difference between the two scattered rays is

$$2\mathrm{Psin}\left[\frac{\theta}{2}\right]$$

where $\mathrm{P} = \mathrm{Dsin}\left[\psi - \frac{\theta}{2}\right]$ is the projection of D on to the plane bisecting the incident and scattered rays and θ is the scattering angle.

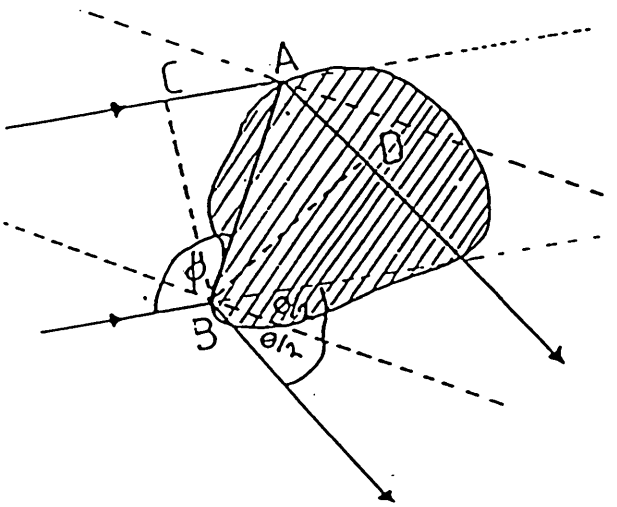


Fig.1.3 A schematic scattering diagram.

If there are two phases present and their scattering properties are different then an interference pattern will be formed. The interference can come from the same particle or two and more particles. The condition for interference to occur is that the path length $2\mathrm{Psin}\left[\frac{\theta}{2}\right]$ must correspond to approximately the diameter of the particle or the interparticle spacing and

should be approximately the magnitude of the wavelength of the incoming radiation.

It is usual to describe the scattering events in terms of the wavevector Q of the radiation. For light, Q can be calculated from

$$Q = \frac{4\pi n}{\lambda} \sin\left[\frac{\theta}{2}\right]$$

where n is the refractive index of the medium and λ the wavelength of the radiation.

Two major differences between SALS, SAXS and SANS are their wavelength of radiation and the contrast required. SALS requires a difference in refractive index, SAXS a difference in electron density and SANS the neutron scattering length. The wavelength of the radiation determines the size of domains which can be resolved by each technique. The range of domain size accessible to each radiation is shown in Fig. 1.4.

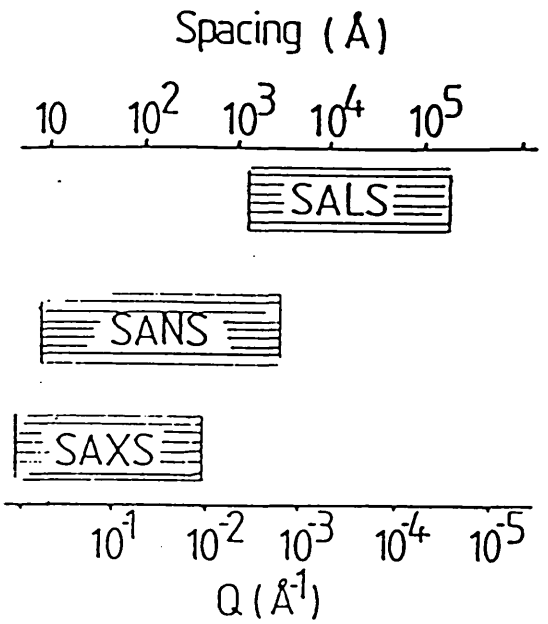


Fig.1.4 Ranges accessible to SANS, SAXA and SALS.

1.4 General survey of pressure effects on polymers and their mixtures

Studies of pressure effects on polymers have been scarce and incomplete. No coherent reviews on this subject exist. In the following section a very broad and general survey of pressure effects on polymers and polymer mixtures is conducted. The pressure effects on polymer solutions and polymer blends are emphasised.

1.4.1 Pressure effects on various transitions of polymers

Studies of pressure effects on glass transitions of polymers and other similar transitions have been vigorous with publications of much experimental[58-65] and theoretical work[66] on this subject. It has been observed that with increasing pressure, the glass transitions of polymers increase with a limiting value of T_g at certain sufficiently high pressure. The increase results mainly from the decrease of free volume of the polymer with increasing pressure. A good review on this subject was conducted by Ferry[67].

Polymer scientists were fascinated by the discovery of extended chain polyethylene crystals under pressurised conditions. Over the years studies on crystalline polymers under pressure flourished. Many research papers and reviews have been published, a few of them are cited here[68-71]. It is generally observed that the equilibrium melting temperature increases with increasing pressure. The high pressure has been linked to the particular ease of chain extension on crystallisation, thus changes of lattice parameters at high pressure are expected, especially in the crystallographic a axis and the c axis – the chain axis. Accordingly the densities, the heats of fusion of crystals formed at high pressures are also different from the ones formed at atmospheric pressure. A

general review on pressure effects on crystalline polymers can be found in the reference[72].

1.4.2 Pressure effects on polymer solutions and polymer blends

Due to academic as well as commercial interests, pressure effects on polymer solutions and polymer blends have been vigorously investigated with many publications[73-93].

For polymer solutions the experimental results have indicated that viscosities of polymer solutions increase with increasing pressure. This increase may be attributed in part to the improvement in the quality of the solvent with pressure, which results in closer interaction between solvents and polymers. Apart from this the free volume difference between polymers and solvents also plays an important role. The application of pressure normally compresses the solvent to a much greater extent than the polymer, thus reducing the free volume difference between them. Since the internal molecular forces are inversely proportional to a high power of the intermolecular radii which decreases as the free volume reduces, the work required to move the liquid molecules past one another, the viscosity, must rise. With the improvement in quality of solvent and the decrease in free volume with pressure, the second virial coefficient, A_2, will change accordingly. The pressure dependence of the second virial coefficient depends on whether the free volume contribution is dominant. Where the free volume is dominant, such as at higher temperature or in systems where the disparity of intermolecular forces between polymers and solvents is small, the second virial coefficient, A_2, should increase with pressure. This was observed for the polyisobutylene/2–methylbutane solution[76]. Under different conditions, such as at lower temperature, A_2 could decrease with

increasing pressure. This was found in the system of polystyrene/transdecalin[73].

All the changes discussed above under pressure are fundamentally related to the pressure effects on volume of mixing and interaction parameters between polymers and solvents. Thus, phase behaviour of polymer solutions will undoubtedly be affected by pressure. The pressure effects on critical temperatures of polymer solutions are given by

$$\left[\frac{\partial T}{\partial p}\right]_c = \left[\frac{\partial^2 \Delta V}{\partial \phi_2^{\,2}}\right] \Big/ \left[\frac{\partial^2 \Delta H}{\partial \phi_2^{\,2}}\right] \simeq T \frac{\Delta V_m}{\Delta H_m}$$

where ΔV is the volume of mixing, ΔH the enthalpy of mixing and ϕ_2 the volume fraction of component 2 in the mixture.

The occurrence of an LCST requires the curvature of ΔH_m, i.e. $\left[\frac{\partial^2 \Delta H}{\partial \phi_2^{\,2}}\right]$, to be positive, while ΔV_m has been observed to be negative, corresponding to a positive curvature of $\Delta V_m(\phi)$. Thus, pressure will raise the LCST of polymer mixtures and polymer solutions. This prediction is experimentally verified by many studies[86,87,89]. However, in the case of poly(ethylene glycol) and water systems, the LCST is almost constant over a pressure range of 1 ~ 50 atm[83]. This is due to the existence of strong hydrogen bonding in the system.

In the case of an upper critical solution temperature (UCST), things become more complicated. For the occurrence of a UCST $\left[\frac{\partial^2 \Delta H}{\partial \phi_2^{\,2}}\right]$ is necessarily negative (corresponding to positive ΔH_m), while $\left[\frac{\partial^2 \Delta V}{\partial \phi_2^{\,2}}\right]$ can be either sign, depending on the values of volume mixing. When the positive values of volume of mixing occur, the $\left[\frac{\partial^2 \Delta V}{\partial \phi_2^{\,2}}\right]$ will be negative, then the UCST will increase with increasing pressure. If negative values of the volume of mixing occur, $\left[\frac{\partial^2 \Delta V}{\partial \phi_2^{\,2}}\right]$ will be positive, then the UCST will decrease with

increasing pressure. Experimentally all these phenomena were observed in several systems[81,82,84-87].

The studies of pressure effects on polymer blends are not as extensive as for polymer solutions. Only limited experimental work[90-93] has been conducted. The lower critical temperatures of polymer blends were found to increase with pressure at a rate ranging from 20°C/Kbar for PS/PVME systems[93] to about 40°C/Kbar for PES/PEO systems[92].

1.5 Studies of phase separation in polymer blends

Under thermodynamically unfavorable conditions, partially miscible polymer mixtures will separate into two phases. The phase separation process can proceed by two distinctly different mechanisms: nucleation and growth and spinodal decomposition. Academic interests and possible commercial application of the interconnected phase structures resulting from spinodal decomposition have inspired the increasing study of spinodal decomposition in polymer blends.

Scattering techniques, mainly SALS, together with the use of microscopic methods, are the major techniques in the investigation of spinodal decomposition. Polymer mixtures which have been studied include polystyrene/poly(vinyl methyl ether[94-103]), poly(methyl methylacrylate)/Poly(α–methyl styrene – acrylonitile)[104-106], solution chlorinated polyethylene/poly(methyl–methylacrylate)[104,107,108], solution chlorinated polyethylene/ethylene–vinylacetate copolymer[107,109], polystyrene/poly(o–chlorostyrene)[110] and polystyrene/poly-(styrene–co–4–bromostyrene)[111,112].

The Cahn–Hillard theory[113,114] (the C–H theory), being widely applied in the treatments of spinodal decomposition, has been found to be capable of qualitatively predicting the phase separation behaviour in the early stages of spinodal decomposition. For a quantitative description of spinodal decomposition, variables, such as thermal fluctuation force[115], might have to be included in the C–H theory. Several theoretical approaches[116-119] aiming at a quantitative description of spinodal decomposition are developed.

In the later stages of spinodal decomposition, involvements of non–linear terms and the surface energy complicated the treatments of the process. There are several theories[120-123] but none of them is good enough to describe quantitatively this process. Experimentally, it is believed[124] that the whole process of spinodal decomposition in polymer blends has no fundamental difference from small molecular mixtures.

The phase separation process is normally initiated by transferring polymer blends from the initial equilibrium one phase state to the final state within the miscibility gap. This transfer is usually accomplished by a temperature jump (see Figure 1.5). The jump is theoretically assumed to be instantaneous; however, such an infinite jump rate can never be experimentally realised. The effects of non–ideal temperature jump on the spinodal decomposition has been discussed by Carmesin *et al*[125]. In practice, these effects are practically neglected in experimental analysis. The temperature jump, on the one hand, limits the time range accessible for observation of early stages of spinodal decomposition where theories exist, on the other, being a continuous process, the consecutive temperatures in the process will make the mixtures separate before the final temperature has been reached. This will affect the subsequent phase separation.

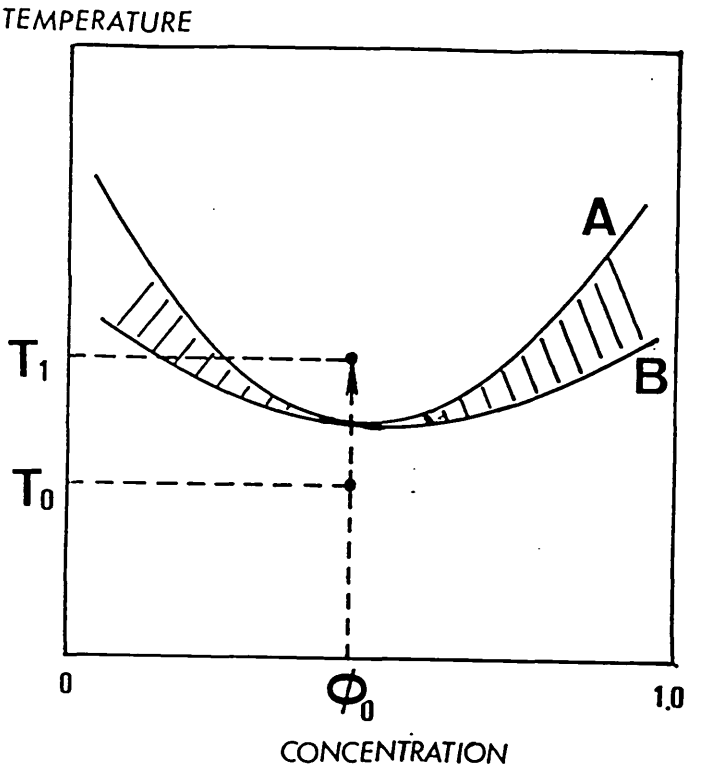


Fig.1.5 A schematic diagram of a temperature jump.

In order to be able to neglect the effects of non–ideal temperature jump, the phase separation has to be reasonably slow. The rate of spinodal decomposition is governed both by the diffusional coefficient of molecules involved and the thermodynamic driving force, $\frac{\partial^2 \Delta G}{\partial \phi_2{}^2}$, for the phase separation (for details see Chapter 3). Thus three methods could be utilised to slow down the phase separation in polymer blends.

1. Working close to the spinodal curve

In this case a shallower temperature jump could be used, which will reduce the time required for the temperature jump. The driving force, $\frac{\partial^2 \Delta G}{\partial \phi_2{}^2}$, is also small since it is linked to the depth of jump by

$$\frac{\partial^2 \Delta G}{\partial \phi_2{}^2} \propto \frac{\Delta T}{T}$$

where $\Delta T = T - T_s$ is the depth of the jump, T the phase separation temperature and T_s the spinodal temperature of the system. Although this method has been practiced in experiments, "close" is a system–dependent term and has to be experimentally verified. The presence of both spinodal decomposition and nucleation and growth in the vicinity of the spinodal curve may make the analysis difficult and even misleading. Moreover it is also believed that thermal fluctuation force plays an important role in the spinodal decomposition when it takes place in a shallow jump. The involvement of the thermal fluctuation force complicates the analysis.

2. Working close to the glass transition temperature of the system

Spinodal decomposition is a diffusional process which is closely dependent on the mobilities of the components in the mixture. The mobilities of polymers before and after the glass transition temperature are strikingly different due to the difference of free volumes on two sides of the glass transition. The relation between temperature and the diffusional coefficients of polymers is expressed[126] by

$$D \propto T$$

D being the mobility of polymers.

Thus a slower spinodal decomposition is expected in the vicinity of the glass transition temperature. This method, however, can not be practically used since any change of the glass transition temperature may not be possible without changing the phase behaviour of the system.

3. Using higher molecular weight polymers

Polymer mobilities, D, are inversely proportional to the square of the molecular weight of polymers, written[127] as

$$D \propto N^{-2}$$

where N is the degree of polymerisation of polymers. Thus, slower phase separation can be achieved when higher molecular weight polymers are used. Moreover, increasing molecular weights of a component in a mixture could decrease the LCST, which in turn slows down the mobility of polymers because it moves closer to T_g. However, the danger here is that polymer mixtures may become immiscible with increasing molecular weights.

The effects of the non–ideal temperature jump in the above three conditions may become relatively trivial so that they can be neglected in practical treatments, but they are not entirely eliminated. For systems with a high rate of phase separation such methods may hardly be applicable. Thus a new approach is required. A pressure jump seemingly offers a better alternative to a temperature jump. A schematic pressure jump is shown in Figure 1.6 in the case of LCST behaviour. A polymer mixture, being at equilibrium conditions of P and T, is in the initial one phase region, while keeping the temperature constant and releasing the pressure from P_1 to P_2, the polymer mixture will be in the final state inside the miscibility gap.

Reasons for pursuing the study of spinodal decomposition via a pressure jump are as follows:

1. A pressure jump offers a new spectrum of studies on spinodal decomposition in polymer blends and an unknown area of research.

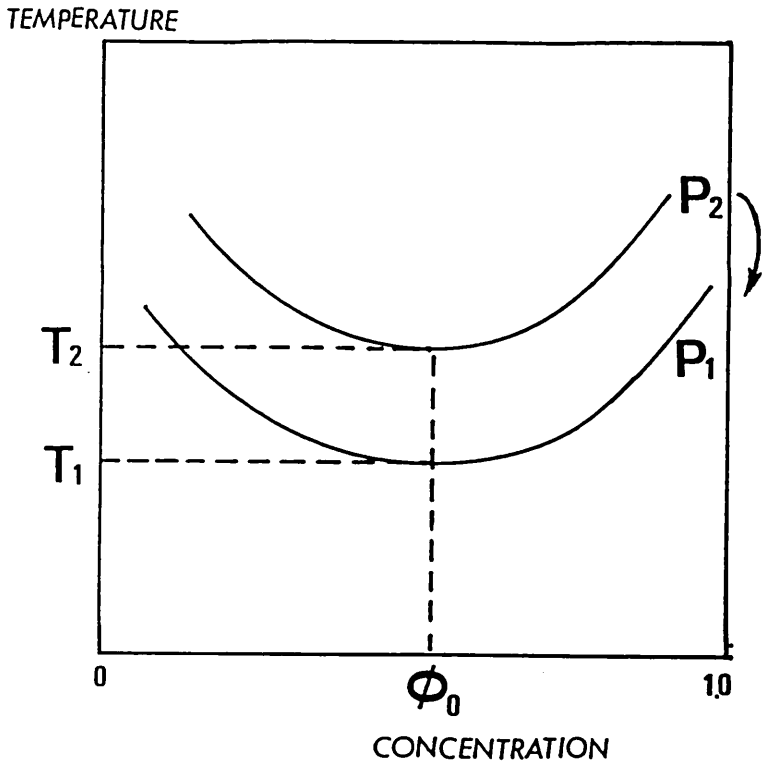


Fig.1.6 A schematic illustration of a pressure jump ($P_2 > P_1$).

2. A pressure jump can be implemented more quickly than a temperature jump. Kiepen's experiments[128] have demonstrated that a pressure jump can be performed 20 times quicker than a temperature jump. Thus the effects of temperature jump can be eliminated. Early stages of spinodal decomposition may then be studied, even for systems with a high rate of phase separation.

3. Pressure is involved in various processing techniques of polymer blends, such as injection molding. The study may enable us to fully understand the pressure effects on polymer mixtures and the final phase structures. The microscopic structures of polymer mixtures bear great importance to mechanical properties.

1.6 Objective of this study

The miscibility and phase separation of polymer blends, after all, depends on experimental results. In this study we present detailed investigation of two polymer mixtures: polystyrene with tetra–methyl bis–phenol–A poly carbonate, poly(ethylene oxide) with poly(ether sulphone). The information sought from this study is: firstly, we wish to know the internal and external parameters affecting miscibilities of polymers and secondly we wish to know the parameters affecting the dynamics of phase separation.

In this study we also present the design of a quick–release diamond anvil pressure cell and its subsequent application in the study of pressure effects on phase boundaries and kinetics of phase separation in systems of polystyrene/poly(vinyl methyl ether) and solution chlorinated polyethylene/ethylene vinyl acetate copolymer. Here we wish to explore the factors contributing to the effects of pressure on polymer mixtures.

Chapter 2

Thermodynamic Theory

In the past few decades two major thermodynamic theories have been developed; there are the Flory–Huggins theory[10-13] and the equation of state[16,17]. In this chapter these two theories will be briefly described and inclusion of pressure in the theories is also considered.

2.1 Flory–Huggins theory

This theory was independently developed by Flory[10,11] and Huggins[12,13] for polymer solutions. Polymer blends were treated as an extension of polymer solutions, in which a long chain polymer is dissolved in another chain length polymer. In their treatment a polymer chain was conceptionally divided into segments of the same size as the lattice sites (Figure 2.1), and the site size was

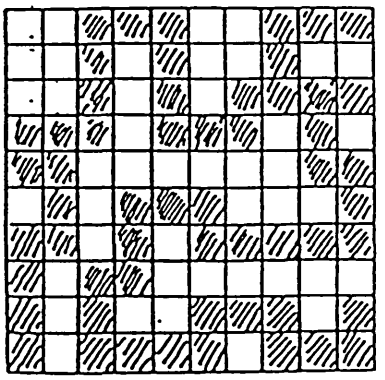


Fig.2.1 Lattice diagrams used in the Flory–Huggins theory.

set equal to that of the solvent molecules. They also assume:

1. lattice sites are equal in size for solvent and polymer segments,
2. the distribution of segments in a polymeric chain is uniform in the lattice,
3. every lattice site has an equal interaction site number (Z) with the others, where Z is the co–ordinate number of the model lattice (both pure liquids and the mixture have the same Z number) and
4. molecules are randomly distributed in the lattice.

Based on these assumptions the enthalpy of mixing and the entropy of mixing can be calculated.

2.1.1 The entropy change on mixing (ΔS_m)

For two monodisperse polymers, each consisting of N_i molecules with x_i segments with an arbitrary common segmental volume, V_r, the entropy of mixing can be obtained by assuming that the segments occupy sites on a three dimensional lattice with a total number of sites equal to the total number of segments.

The entropy directly depends on the randomness of the system. If we assign $\Omega(1)$ and $\Omega(2)$ as the total number of ways of putting all N_i segments of polymer 1 and polymer 2 in the lattice, the total number of ways of putting polymer 1 and 2 in the mixture would be the product of $\Omega(1)$ and $\Omega(2)$. By Boltzman's law, the entropy of mixing would be:

$$S_m = k \ln[\Omega(1).\Omega(2)] = k[\ln\Omega(1) + \ln\Omega(2)] \qquad (2.1)$$

Therefore the entropy change on mixing polymer 1 and 2 would be:

$$\Delta S_m = S_m - (S_1 + S_2)$$

$$= S_m - [(S_m)_{N_1=0} + (S_m)_{N_2=1}] \qquad (2.2)$$

Through various complex mathematical manipulation it results that:

$$\Delta S_m = -k\left\{N_2 \ln\left[\frac{N_2X_2}{N_1X_1 + N_2X_2}\right] + N_1 \ln\left[\frac{N_1X_1}{N_1X_1 + N_2X_2}\right]\right\} \qquad (2.3)$$

where $\frac{N_2X_2}{N_1X_1 + N_2X_2}$ is the volume fraction of component 2 in the mixture.

Hence $$\frac{N_2X_2}{N_1X_1 + N_2X_2} = \phi_2 \text{ and } \phi_1 = 1 - \phi_2 \qquad (2.4)$$

k is the Boltzman's constant

$$k = R/N_A \qquad (2.5)$$

R being the gas constant and N_A Avogadro's constant.

Substituting Equations (2.4) and (2.5) into (2.3) yields:

$$\Delta S_m = -R\left\{\frac{N_2}{N_A} \ln\phi_2 + \frac{N_1}{N_A} \ln\phi_1\right\} \qquad (2.6)$$

$$= R(n_2 \ln\phi_2 + n_1 \ln\phi_1)$$

Here n_i is the molar number of each component.

2.1.2 The enthalpy change on mixing (ΔH_m)

The enthalpy of mixing comes from the replacement of some of the contacts between like species in the pure components with contacts between unlike species in the mixture. If we assume the contact energy (attractive energy) between like segments of polymer 1 and 2 to be ϵ_{11} and ϵ_{22} and the contact energy between unlike segments to be ϵ_{12}, then the energy change for the formation of one unlike contact will be:

$$\Delta\epsilon_{12} = \epsilon_{1\,2} - \frac{1}{2}(\epsilon_{11} + \epsilon_{22}) \tag{2.7}$$

while the change of enthalpy on mixing would be

$$\Delta H_m = \Delta\epsilon_{12}.P_{12} \tag{2.8}$$

P_{12} is the number of pairs of unlike segments in the mixture and equals

$$P_{12} = ZN_1X_1\phi_2 \tag{2.9}$$

Thus $$\Delta H_m = Z.\Delta\epsilon_{12}N_1X_1\phi_2 = n_1\phi_2[Z.\Delta\epsilon_{12}X_1\ N_A] \tag{2.10}$$

If we define $$\chi_{12} = Z\ X_1\Delta\epsilon/kT$$

Equation (2.10) will become

$$\Delta H_m = n_1\phi_2RT\chi_{12} \tag{2.11}$$

Here χ_{12} is known as the Flory–Huggins interaction parameter.

2.1.3 The Gibb's free energy of mixing (ΔG_m)

Provided that the derived combinatorial (configurational) entropy change (ΔS_m) represents the total entropy change on mixing, the Gibb's free energy of mixing for a total volume V of two polymers can be calculated from

$$\Delta G_m = \Delta H_m - T\Delta S_m \tag{2.12}$$

By substituting the corresponding equation of ΔS_m and ΔH_m we have:

$$\Delta G_m = RT(n_1 \ln\phi_1 + n_2 \ln\phi_2 + n_1\phi_2\chi_{12}) \tag{2.13}$$

The above equation is derived at atmospheric pressure (p = 0). At high pressure, $P.\Delta V_m$, ΔV_m being the volume change on mixing, has to be included in the equation.

2.1.4 Extended F–H theories

Disagreements between the F–H theory and experimental results were found in the use of the theory. This theory failed to predict the LCST behaviour observed in most polymer mixtures. It also could not explain the interaction parameters which were observed to be not only temperature, but also concentration dependent. No molecular interpretation of the bimodality of phase diagrams observed in several systems[129,130] was given by the theory. The theory cannot be applied to a system with strong specific interaction because there is a possibility of an ordered structure and only combinatorial entropy is considered in the theory. The assumption of random distribution in mixing also

neglects the influence of preferential interaction between unlike segments which may make the distribution of unlike segments non–random.

Attempts at modifying the F–H theory have been made in the past years. Orr[131] and Guggenheim[132] have tried to calculate the entropy of mixing due to non–randomness of mixing, though the results made no significant change to the original theory. Refinements made by Huggins[133] and Miller[134] resulted in a complicated expression, but without improved agreements with practical results.

The interaction parameter which has drawn much of the criticism of the F–H theory was also modified to take the effects of concentration as well as temperature into account. Koningsveld and his co–workers[130,135] developed an expression for the free energy of mixing written as

$$\frac{\Delta G_m}{RT} = \frac{\phi_1}{m_1} \ln\phi_1 + \frac{\phi_2}{m_2} \ln\phi_2 + g\phi_1\phi_2 \qquad (2.14)$$

where m_1 and m_2 are the polymer chain lengths and the term $g\phi_1\phi_2$ is used for any correction for fitting the experimental data. The difference between this semi–empirical term and the original term in F–H theory is that the g–function here is assumed to be concentration dependent.

i.e. $$g = g_0 + g_1\phi_2 + g_2\phi_2^2 + \ldots . \qquad (2.15)$$

Furthermore g could also be assumed to be pressure dependent.

Similar efforts were also made by Tompa[14].

2.2 The equation of state theory

In the equation of state, Flory and his co–workers[16,17] abandoned the whole concept of the lattice model. Each pure component was characterised by the equation of state parameters, V*, T*, P*, which would be evaluated from pure component data: thermal expansion coefficient, density and thermal pressure coefficient. An interaction term, X_{12} was introduced to characterise the difference in chemical nature of the components.

2.2.1 The pure component

Following the assumption of Prigogine[136], Flory developed a partition function whose lattice energy is inversely related to volume.

$$Z_{tr} = \left[\frac{2\pi MikT}{h^2}\right]^{3N_iC_iV_i/2}.Q \tag{2.16}$$

$$Q = \Omega_{comb}.(\gamma v_i^*)^{N_iC_iV_i}.(\tilde{v}_i^{1/3} - 1)^{N_iC_iV_i}.\exp(U_{0i}/kT) \tag{2.17}$$

Here Z_{tr} is the partition function, Q is the configurational integral, Ω_{comb} is the combinatorial factor, $\tilde{v}_i$ is the reduced volume per segment and γ is the geometrical factor. 3C is taken to be the number of external degrees of freedom for one segment, v_i is the number of segments per chain and the lattice energy, U_{0i}, can be defined as a function of reduced temperature, $\tilde{T} = T/T^*$, T^* being the characteristic temperature

$$-U_{0_i}/kT = V_i C_i N_i / \tilde{\nu}_i \tilde{T}_i \qquad (2.18)$$

The corresponding equation of state is

$$\tilde{p}_i \tilde{\nu}_i / \tilde{T}_i = \tilde{v}_i^{1/3}/(\tilde{v}_i^{1/3} - 1) - \frac{1}{\tilde{v}_i \tilde{T}_i} \qquad (2.19)$$

where $\tilde{P}_i = P/P_i^*$, pressure, p, is the total hydrostatic pressure and p* is the characteristic pressure.

Parameters in Equation (2.27) are associated with the thermal expansion coefficient, $\alpha = \left[\left[\frac{\partial V}{\delta T}\right]_p\right]/v$, and the thermal pressure coefficient, $\beta = \left[\frac{\partial V}{\delta T}\right]_v$ through the following equations.

$$\left[\frac{\tilde{p}\tilde{v}^2 - 1}{\tilde{p}\tilde{v}^2 + 1} + \frac{1}{3(\tilde{v}^{1/3} - 1)}\right] = \frac{1}{\alpha T} \qquad (2.20)$$

$$\frac{\tilde{v}}{p^*} = \frac{1}{T}\left[\frac{1}{\tilde{v}_v} + \tilde{p}\tilde{v}\right] \qquad (2.21)$$

From Equations (2.19), (2.20) and (2.21), parameters p*, T* and v*, characterising pure components can be obtained.

The above equations are derived in a general form. In specific conditions, such as p = 0, they can be simplified.

2.2.2 Monodisperse binary mixtures

The above equations are formally the same for pure components as for mixtures. However, in the case of mixtures, Ω_{comb} becomes the Flory–Huggins

combinatorial factor, N is the sum of all N_i, $\bar{r}$ is the number average chain length, while, C, being used to characterise the volume dependent degree of freedom is equal to

$$C = C_1\psi_1 + C_2\psi_2 - \psi_1\psi_2 C_{12} \tag{2.22}$$

Here C_{12} is the quadratic correction coefficient and ψ_i is the segment fraction of each component in the mixture.

For the derivation of segment fraction, the assumption is used that the mixture has only one characteristic hard–core volume per segment which is arbitrarily taken to correspond to a monomer unit. For a binary mixture the segment ratio is arbitrarily set equal to the ratio of the pure component hard–core volume per mole:

$$\frac{r_2}{r_1} = \frac{V_2^*}{V_1^*} = \frac{M_2 V_2^*{}_{spec}}{M_1 V_1^*{}_{spec}} \tag{2.23}$$

M_i being the molecular weight of substance i. If V^* is the hard–core volume per mole of the mixture, then

$$r_1 V^* = V_1^* \text{ or } r_2 V^* = V_2^* \tag{2.24}$$

Since $\frac{r_2}{r_1}$ can be obtained from V_1^* and V_2^*, either r_1 or r_2 must be arbitrarily chosen to determine V^*. In terms of this, the component segment fraction is:

$$\psi_1 = \frac{r_1 x_i}{r_1 x_i + r_2 x_2} = \frac{r_1 x_1}{\bar{r}} = \frac{N_1 r_1}{\bar{r}} \tag{2.25}$$

and $$\psi_2 = 1 - \psi_1 \tag{2.26}$$

where x_i is the mole fraction.

The calculation of U_0 is based on the assumption that the intermolecular attraction energy depends on the surface area of contacts between adjoining segments.

$$-U_0 = [A_{11}(\eta_{11}/v) + A_{22}(\eta_{22}/v) + A_{12}(\eta_{12}/v)] \tag{2.27}$$

where A_{ij} is the number of nearest neighbour contacts with energy η_{ij}/v.

A_{ij} is related to the intermolecular contact sites per segment, S_i, through the following:

$$2A_{11} + A_{12} = S_1 r_1 N_1 \tag{2.28}$$

$$2A_{22} + A_{12} = S_2 r_1 N_2 \tag{2.29}$$

Combining Equations (2.27), (2.28) and (2.29) yields

$$-U_0 = \frac{1}{2}\left[S_1 r_1 N_1\left[\frac{\eta_{11}}{\nu}\right] + S_2 r_2 N_2\left[\frac{\eta_{22}}{\nu}\right] - A_{12}\frac{\Delta\eta}{\nu}\right] \tag{2.30}$$

where $\Delta\eta = \eta_{11} + \eta_{22} - 2\eta_{12}$. If it is assumed that the probability of finding a species of type "2" next to a given site is equal to the segment surface fraction, θ_2

$$\theta_2 = 1 - \theta_1 = \frac{S_2 r_2 N_2}{S_1 r_1 N_1 + S_2 r_2 N_2} = \frac{S_2\psi_2}{S_1\psi_1 + S_2\psi_2} = \frac{S_2\psi_2}{S} \tag{2.31}$$

Then $$A_{12} = S_1 r_1 N_1 \theta_2 = S_2 r_2 N_2 . \theta_1 \tag{2.32}$$

and $$-U_0 = \frac{S}{2v}\left[\theta_1 \eta_{11} + \theta_2 \eta_{22} - \theta_1 \theta_2 . \Delta\eta\right] \tag{2.33}$$

The equations defining various pure component characteristic parameters are

$$P_i^* = S_i \eta_{ii} / 2 v_i^{*2} \tag{2.34}$$

$$N_i C_i k T_i^* = P_i^* v_i^{*2} \tag{2.35}$$

$$X_{ij} = S_i \Delta\eta_{ij} / 2 v_i^{*2} \tag{2.36}$$

Thus the corresponding P* for the mixture is

$$P^* = \psi_1 P_1^* + \psi_2 P_2^* + \psi_1 \theta_2 X_{12} \tag{2.37}$$

where $X_{12} = S_1 \Delta\eta / 2 v^{*2}$ is the interaction term and T for the mixture is

$$T^* = P^* / \left[\frac{\psi_1 P_1^*}{T_1^*} + \frac{\psi_2 P_2^*}{T_2^*}\right] \tag{2.38}$$

Knowing the above values, the free energy of mixing can be calculated.

2.2.3 The free energy of mixing

The Helmoholtz free energy of mixing can be calculated from

$$\Delta F_m = -RT\ln(Z/Z_1Z_2)$$

$$= RT(n_1\ln\psi_1 + n_2\ln\psi_2)$$

$$+ 3\bar{\gamma}Nv^*\{\psi_1P_1^*\tilde{T}_1\ln[(\tilde{v}_1^{1/3}-1)/(\tilde{v}_1^{1/3}-1)]$$

$$+ \psi_2P_2^*\tilde{T}_2\ln[(\tilde{v}_2^{1/3}-1)/(\tilde{v}_2^{1/3}-1)]\}$$

$$+ \bar{r}Nv^*(\psi_1P_1^*/\tilde{v}_1 + \psi_1P_1^*/\tilde{v}_1 - P^*/v^* \qquad (2.39)$$

The first two terms on the R.H.S. of the equation are the entropy of mixing in which combinatorial entropy is included. In the later development Flory[18] introduced an additional term, $-\bar{r}Nv^*\psi_1\theta_2Q_{12}$, where Q_{12}, being the empirical interaction entropy parameter, reflects the change of entropy due to the interaction of unlike segments during mixing. Thus

$$-T\Delta S_m = RT(n_1\ln\psi_1 + n_2\ln\psi_2)$$

$$+ 3\bar{r}Nv^*\{\psi_1P_1^*\tilde{T}_1\ln[(\tilde{v}_1^{1/3}-1)/(\tilde{v}_1^{1/3}-1)]$$

$$+ \psi_2P_2^*\tilde{T}_2\ln[(\tilde{v}_2^{1/3}-1)/(\tilde{v}_2^{1/3}-1)]\} - \bar{r}Nv^*\psi_1\theta_2Q_{12}$$

(2.40)

The second term on the R.H.S. of Equation (2.40) is the energy of mixing, ΔE_m. Thus the enthalpy of mixing is

$$\Delta H_m = \Delta E_m + P\Delta V_m \tag{2.41}$$

Here ΔV_m is the excess volume of mixing and can be obtained from

$$\frac{\Delta V_m}{V_0} = \frac{\tilde{v} - \tilde{v}^0}{\tilde{v}^0} = \frac{\tilde{v}}{\tilde{v}^0} - 1 = \frac{\tilde{v}}{\psi_1 v_1 + \psi_2 v_2} - 1$$

$$= \frac{1}{\left[\frac{w_1}{d_1} + \frac{w_2}{d_2}\right] d_m} - 1 \tag{2.42}$$

where w_i is the weight fraction and d_1, d_2 and d_m are densities. V_0 is the total volume of the mixture.

Knowing $-T\Delta S_m$ and ΔH_m, the Gibb's free energy of mixing can be calculated using the usual thermodynamic equation

$$\Delta G_m = \Delta H_m - T\Delta S_m \tag{2.43}$$

By using equations for phase equilibria, the binodal, spinodal and critical points can be calculated.

For the spinodal $$\frac{\partial^2 \Delta G_m}{\partial \phi_2^2} = 0$$

$$-\frac{1}{\psi_1} + \left[1 - \frac{r_1}{r_2}\right] - (P_1^* v_1^*/RT_1^*)\left[\frac{\partial \tilde{v}}{\partial \psi_2}\right] / [\tilde{v}^{2/3}(\tilde{v}^{1/3} - 1)]$$

$$+ \left[\frac{P_1^* v_1^*}{RT}\right]\left[\frac{1}{\tilde{v}^2} + \tilde{P}_1\right]\frac{\partial \tilde{v}}{\partial \psi_2} + \left[\frac{V_1^* X_{12}}{RT}\right][2\theta_1\theta_2^2/\tilde{v}\psi_1\psi_2$$

$$-(\theta_2^2/\tilde{v}^2)\frac{\partial \tilde{v}}{\partial \psi_2}] - v_1^* Q_{12}/R)[2\theta_1\theta_2^2/\tilde{v}\psi_1\psi_2] = 0 \tag{2.44}$$

where

$$\frac{\partial \tilde{v}}{\partial \psi_2} = \left[\frac{\partial \tilde{v}}{\partial \psi_2} - \left[\frac{1}{\tilde{T}}\right]\left[\frac{1}{\tilde{v}} + \tilde{P}\right]\frac{\partial \tilde{T}}{\partial \psi_2}\right] / \left\{\frac{2}{\tilde{v}^3} - \tilde{T}(\tilde{v}^{1/3} - \frac{2}{3})[\tilde{v}^{5/3}(\tilde{v}^{1/3} - 1)^2]\right\} \tag{2.45}$$

$$\frac{\partial \tilde{p}}{\partial \psi_2} = [p_1^* - p_2^* + X_{12}\theta_2(\theta_1/\psi_2 - 1)]P/P^{*2} \tag{2.46}$$

$$\frac{\partial \tilde{T}}{\partial \psi_2} = \left[\frac{p_2^*}{T_2^*} - \frac{p_1^*}{T_1^*}\right]\frac{T}{p^*} + [p_1^* - p_2^* + X_{12}\theta_2\left[\frac{\theta_1}{\psi_1} - 1\right]]\frac{T}{p^*} \tag{2.47}$$

and for the critical point is

$$\frac{\partial^3 \Delta G_m}{\partial \phi_2^{\tilde{3}}} = 0$$

$$-\frac{1}{\psi_1} + (P_1^* v_1^*/RT_1^*)\left\{\left[\frac{\partial \tilde{v}}{\partial \psi_2}\right]^2\left[1 - \frac{2}{2\tilde{v}^{1/3}}\right]/[\tilde{v}^{4/3}(\tilde{v}^{1/3} - 1)^2]\right.$$

$$\left. - \left[\frac{\partial^2 \tilde{v}}{\partial \psi_2^2}\right]/\left[\tilde{v}^{2/3}(\tilde{v}^{1/3} - 1)\right]\right\} + \left[\frac{P_1^* v_1^*}{RT}\right]\left[\left[-\frac{2}{\tilde{v}^3}\right]\left[\frac{\partial \tilde{v}}{\partial \psi_2}\right]^2\right.$$

$$\left. + \left[\frac{1}{\tilde{v}^2} + \tilde{P}_1\right]\left[\frac{\partial^2 \tilde{v}}{\partial \psi_2^2}\right]\right]$$

$$+ \left[\frac{v_1^* X_{12}}{RT}\right]\left\{\frac{1}{\tilde{v}}\left[2\left[\frac{\partial \theta^2}{\partial \psi_2}\right]^2 + 2\theta_2\left[\frac{\partial^2 \theta^2}{\partial \psi_2^2}\right]\right] - \frac{1}{\tilde{v}^2}\right\}\left[4\theta_2\left[\frac{\partial \theta^2}{\partial \psi_2}\right]\left[\frac{\partial \tilde{v}}{\partial \psi_2}\right]\right.$$

$$\left. + \theta_2^2\left[\frac{\partial^2 \theta^2}{\partial \psi_2^2}\right]\right] + \left[\frac{\theta_2^2}{\tilde{v}^3}\right]\left[\frac{\partial \tilde{v}}{\partial \psi_2}\right]^2\Bigg\} = 0 \tag{2.48}$$

Equally, the binodal can also be obtained.

The above equations are derived from the perfect chemical potential. They should be applicable to the cases where pressure is involved. At pressure P = 0, the equation should give the same results as the equations given by Flory[137].

2.2.4 Shortcomings of the equation of state theory

Over the years many attempts have been made to apply the equation of state in describing the thermodynamic behaviour of polymer blends.

McMaster[18] examined the contribution of the pure and binary state parameters to the miscibility of hypothetical polymer–polymer mixtures. He observed that the theory was capable of predicting both lower and upper critical solution temperature behaviour individually or simultaneously. Olabisi[22] has applied McMaster's treatment to a real mixture of poly(ϵ–caprolactone) with poly(vinyl chloride) and indicated that the bimodality of phase diagrams may be a consequence of the odd combinations of large differences in the pure component properties with rather large negative X_{12}. Using a simpler form of McMaster's derivation, ten Brinke *et al*[23] studied the effect of binary parameters on the asymmetrical shape of the spinodal curves. Walsh *et al*[20,21] have simulated the phase diagrams of several real polymer blends from the measurements of heats of mixing of their corresponding oligomers. In most cases flatter phase diagrams were obtained from the simulation.

Undoubtedly the equation of state theory is more powerful than the F–H theory in their predictive capability. However, only qualitative agreements between experiments and the equation of state theory have so far been obtained. The complexity of the theory and difficulties of obtaining various paramters

needed in the theory have hampered the efforts of assessing the real potential of the theory. Many studies are still greatly required.

2.3 Theoretical treatment of pressure effects on polymer miscibility

Pressure effects on polymer mixture are mainly due to the volume change on mixing. The original F–H theory does not consider the volume change on mixing, so it cannot be used to explain the effect of pressure on polymer mixtures. The extended F–H theories[135] where the interaction parameter χ_{12} is assumed to be temperature, concentration and pressure dependent, are successful in explaining some odd behaviour of polymer mixtures, such as, bimodality of phase diagram, their use in the treatment of pressure effects on polymer mixture has been attempted by Koningsveld[138].

In Koningsveld's treatment it was assumed that in the Flory–Huggins equation the effect of pressure on ΔG_m is confined to g (Equation 2.19).

$$\left[\frac{\partial\left[\frac{\Delta G_m}{RT}\right]}{\partial P}\right]_T = \Delta V = \phi_1\phi_2\left[\frac{\partial g}{\partial P}\right]_T \qquad (2.49)$$

It was also assumed that all volumes occurring in ΔV, the volume of mixing, depends on pressure in the usual way:

$$V = V_{P_0}\exp[-k(P - P_0)] \qquad (2.50)$$

where V_{P_0} is the volume at reference pressure, P_0, and k is the isothermal compressibility (taken to be independent of P). Introduction of Equation (2.50)

into Equation (2.49), integration and subsequent approximation of the exponential by means of the first terms of its expansion, leads to

$$g = g_0 + (p - p_0)\Delta V_{P_0}/RT\phi_1\phi_2 \qquad (2.51)$$

Now if we choose ΔV_{P_0} proportional to $\phi_1\phi_2$ and assume each term V in ΔV_{P_0} to be linearly dependent of T, some mathematical calculation then leads to a relation between cloud point pressure and temperature

$$\frac{1}{T} = B + \frac{D}{P + K} \qquad (2.52)$$

Within the assumption made, B, D and K are determined by the nature of the mixture and only D depends on composition.

The above Equation (2.56) can be used to fit the experimental cloud point–pressure data very well[139]. However, such empiricism provides little understanding of the underlying causes of observe thermodynamic behaviour.

The equation of state theory is very powerful in regards to the theoretical explanation of pressure effect on polymer mixtures since volume change on mixing is accounted for in the theory. The usefulness of this theory in the treatment of pressure effects on polymer mixtures is demonstrated by the work of Walsh[91,92], McMaster[18] and Patterson[19,87].

The main assumptions made in Walsh's treatments are that the equation of state theory in the simplified form can be used with constant values of P*, T* and V* and that the effect of pressure on X_{12} and Q_{12} can be neglected. X_{12} used in the calculation was obtained from heat of mixing measurements using low molecular mass analogues, Q_{12} was used as an adjustable parameter to fit the minimum of the spinodal to the minimum of the experimental cloud point

curve. Then the full spinodal curve was calculated and compared with the measured cloud point curve. The results showed that the theory could satisfactorily predict the positive value of $\left[\frac{dT}{dp}\right]$ at the critical point, but it failed to predict the shape of the curve correctly. It was also discovered that the shape of the phase diagrams did not change with increasing pressure.

In Patterson's treatments of pressure effects on phase equilibria equations derivated from the F–H theory and the equation of state were combined to give

$$\frac{\chi_{12}}{M_1 v_1^*} = \frac{C_1}{M_1 v_1^*}\left[\frac{1}{\tilde{v}_1 \tilde{T}_1}\frac{X_{12}}{P_1^*} + \frac{1}{2}C_{p,1}\left\{\tau + \frac{\tilde{p}_1\tilde{v}_1}{1 + \tilde{p}_1\tilde{v}_1^2}\pi\right\}\right] \qquad (2.53)$$

where τ is a term used to characterise the free volume difference between two components in the system and equals to $1 - T_1^*/T_2^*$, π a term characterised as $\pi = 1 - P_1^*/P_2^*$.

Here C_1 is the number of "segments" in the component 1 molecule and

$$\frac{C_1}{M_1 v_1^*} = \frac{P_1^*}{RT_1^*} \qquad (2.54)$$

$C_{\tilde{P}_1}$ the reduced heat capacity of component 1 and equals

$$C_{\tilde{P}_{11}} = (1 - \frac{2}{3}\tilde{v}^{-1/3}) - \frac{2(1 - \tilde{v}^{-1/3})}{1 + p\tilde{v}^2} \qquad (2.55)$$

The equation of state is still the same as Equation (2.23), written as

$$\frac{\tilde{P}\tilde{V}}{\tilde{T}} = \frac{\tilde{v}^{1/3}}{\tilde{v}^{1/3} - 1} - \frac{1}{\tilde{T}\tilde{v}} \qquad (2.56)$$

Based on the above equations, critical temperatures at different pressures can be calculated.

The pressure dependence of the critical temperature $\left[\frac{dT}{dP}\right]_{crit}$ is given[87] by the relation

$$\left[\frac{dT}{dP}\right]_{crit} = -\frac{(\partial x/\partial p)_T}{(\partial x/\partial T)_p} \simeq \frac{T\Delta V_m}{\Delta H_m} \qquad (2.57)$$

where ΔV_m and ΔH_m are the volume change of mixing and the enthalpy of mixing.

The present theoretical treatments of pressure effects on phase diagrams are far from complete and satisfactory. Assumptions of pressure independent X_{12} used in the analysis[91,92] are hardly realistic. Pressure effects on the equation of state coefficient, such as thermal expansion coefficient, are also neglected. Moreover, the simple monotonic dependence of the lattice energy with distance ($E_i(0) \propto 1/v^n$, $1.0 < n < 1.5$), assumed in the equation of state theory is also inadequate. Thus efforts are greatly required in these aspects of thermodynamics of polymer–polymer miscibility.

2.4 Melting point depression

There is no comprehensive theoretical model available to explain the crystalline behaviour of crystallisable components in a polymer mixture. Sanchez *et al*[140] offered a theoretical model with various degrees of approximations for crystallisation behaviour from a dilute solution. Flory[141] related the observed melting point depression to an entropy and enthalpy of the crystalline units in the mixtures. Based on the equation of state, Rostami[142]

also attempted to resolve this problem. In this paragraph the treatment of Nishi and Wang[44] is outlined.

The thermodynamic mixing of two polymers was treated by Scott using the Flory–Huggins approximation[21]. For this system the chemical potential, μ_{zu}', per mole of crystalisable polymer units in the mixture relative to its chemical potential, μ_{zu}^0, in the pure liquid can be expressed as

$$\mu_{zu}' - \mu_{zu}^0 = \frac{RTV_{zu}}{V_{iu}}\left[\frac{\ln \phi_2}{m_2} + \left[\frac{1}{m_2} - \frac{1}{m_1}\right]_x (1 - \phi_2) + \chi_{12}(1 - \phi_2)^2\right] \tag{2.58}$$

where the subscript 1 identifies the amorphous polymer and 2 with the crystalline polymer, V_u is the molar volume of the repeating units, m is essentially the degree of polymerisation, χ_{12} the polymer–polymer interaction parameter, R the gas constant and T the absolute temperature. The difference in the chemical potential between a crystalline polymer unit, μ_{zu}^c, and the same unit in the pure liquid state, μ_{zu}^0, can be written as

$$\mu_{zu}^c - \mu_{zu}^0 = -(\Delta H_{zu} - T\Delta S_{zu})$$

$$= \Delta H_{zu}(1 - (T/T^0)) \tag{2.59}$$

where ΔH_{zu} and ΔS_{zu} are the enthalpy and entropy of fusion per mole of repeating unit and the ratio $\frac{\Delta H_{zu}}{\Delta S_{zu}}$ is assumed to be independent of temperature and equal to T_m^0, the equilibrium melting temperature.

On the condition that at melting point, T_m, of the mixture, the chemical potential of the crystalline component in the mixture is equal to the chemical potential of the amorphous phase, the melting point lowering will be given by

$$\frac{1}{T_m} - \frac{1}{T_m^0} = -\frac{RV_{zu}}{\Delta H_m V_{in}}\left[\frac{\ln \phi_2}{m_2} + \left[\frac{1}{m_2} - \frac{1}{m_1}\right](1-\phi_2) + \chi(1-\phi_2)^2\right] \tag{2.60}$$

Since m_1 and m_2 are large, then

$$\frac{1}{T_m} - \frac{1}{T_m^0} = -\frac{RV_{zu}}{\Delta H_m V_{in}}\chi(1-\phi_2)^2$$

$$= -\frac{RV_{zu}}{\Delta H_m V_{in}}\chi(\phi_1)^2 \tag{2.61}$$

Therefore

$$\frac{1}{\phi_1}\left[\frac{1}{T_m} - \frac{1}{T_m^0}\right] = -\frac{RV_{zu}}{\Delta H_m V_{in}}\chi(\phi_1) \tag{2.62}$$

According to Equation (2.62), the plot of $\frac{1}{\phi_1}\left[\frac{1}{T_m} - \frac{1}{T_m^0}\right]$ against ϕ_1 should be a straight line. From the slope of the straight line an interaction parameter, χ_{12}, can be calculated.

Chapter 3

Theories of kinetics of phase separation

3.1 Introduction

Due to the growing importance of studies on phase separation in polymer blends both academically and practically, much theoretical work[113,114,116-119] on the kinetics of phase separation have been conducted in the past few decades. Among these the Cahn – Hillard theory[113,114] is the most widely used.

In this chapter the basic thermodynamics of phase separation is discussed. The Cahn – Hillard theory is reviewed, followed by discussion and various extended theories.

3.2 Phase separation in polymer mixtures

For partially miscible polymer blends at any given temperature, T_0, inside the temperature gap, we can expect the free energy of an undecomposed mixture to vary with concentration as depicted in Figure 3.1. The points of common tangency (A's) define the concentration of the two coexisting phases (binodal) at T_0, where the chemical potentials of the two phases are equal.

$$\left[\frac{\partial G}{\partial \phi}\right]_A = \left[\frac{\partial G}{\partial \phi}\right]_{A'}$$

$$\left[\frac{\partial G}{\partial \phi}\right]_B = \left[\frac{\partial G}{\partial \phi}\right]_{B'} \qquad (3.1)$$

Here A(B) and A′(B′) represent the two coexisting phases.

The two inflection points on the curve correspond to the spinodal points where $\frac{\partial^2 G}{\partial \phi^2} = 0$. The region between them, with a negative curvature of $\frac{\partial^2 G}{\partial \phi^2}$, is the unstable region. The region between the inflection points and minimum points is the metastable region.

In the metastable region a small change in concentration will result in an increase of free energy (the inset in Figure 3.1). Thus all the small

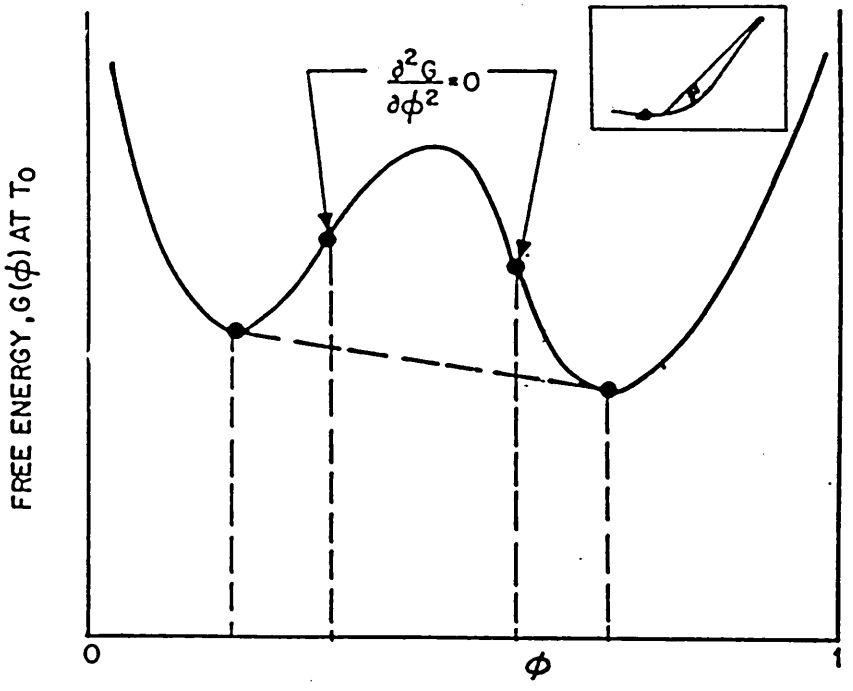


Fig.3.1 The spinodal defined by the locus of temperatures on the phase diagram at which $\frac{\partial^2 G}{\partial \phi^2} = 0$. Inside the spinodal it is negative and outside it is positive.

concentration fluctuations tend to decay. Hence, phase separation can only proceed by overcoming the energy barrier with a larger fluctuation in concentration. This larger concentration fluctuation is called a nucleus. Once such a nucleus is formed it grows by a normal diffusion process. This is called the nucleation and growth mechanism.

In the unstable region (Figure 3.1) any small concentration fluctuation will result in phase separation because it lowers the free energy. Since there is no energy barrier to phase separation, the phase separation should occur by a continuous and spontaneous process. This process is called spinodal decomposition.

The major difference between the two mechanisms lies in the directions in which like molecules move in a concentration gradient, which is shown in Figure 3.2. In nucleation and growth the new phase starts from small nuclei,

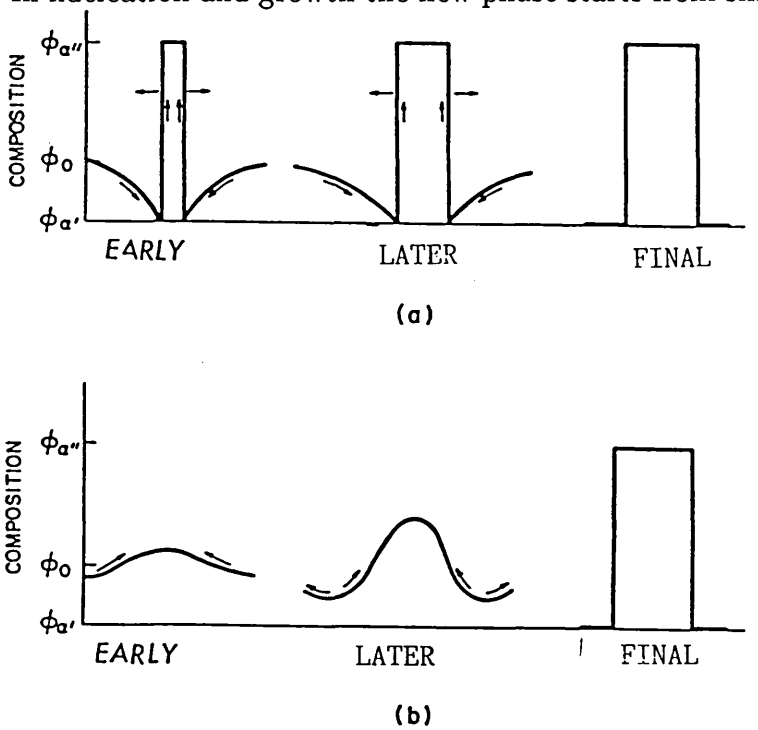


Fig.3.2 Schematic drawing of time evolution of composition profiles for nucleation and growth and spinodal decomposition.
a) nucleation and growth, b) spinodal decomposition.

then proceeds to grow in extent. The molecules that feed the new phase follow the ordinary transport phenomena by downhill diffusion (Figure 3.2a). In the spinodal decomposition the new phase is formed by a continuous flux of like molecules against the direction of a concentration gradient created by small

concentration fluctuations which therefore has an uphill diffusion with a negative diffusion coefficient.

Studies of phase separation have been mainly concentrated on spinodal decomposition, while the nucleation and growth mechanism seems to be forgotten. There are three reasons for this.

Firstly, spinodal decomposition is one of the few solid state transformations for which there is any plausible quantitative theory. This is due to the inherent simplicity of the transformation. It can be treated purely as a diffusional problem and moreover many of the characteristics of the decomposition can be described by an approximate analytic solution to the diffusion equation. In contrast, theories for nucleation and growth have to invoke the thermodynamics of fluctuations, and the diffusional problem involved in the growth of the nucleus is far more difficult to solve because it is unrealistic to linearise the diffusion equation.

Secondly, from the practical point of view, spinodal decomposition is of interest because it affords a means of producing an interconnected structure that may enhance the properties of a material.

Thirdly, studies of nucleation and growth mechanisms require the elimination of foreign particles from the system, which makes the study difficult to do, especially for polymer mixtures.

Spinodal decomposition can be divided into three stages according to the development of wavelength and amplitude of the concentration fluctuations (see Figure 3.3). In the early stage (a), the wavelength of concentration is kept constant while the amplitude of concentration fluctuation increases with time. In the later stage (b), both the amplitude and wavelength of the concentration fluctuations increase with time. In the final stages the amplitude and

wavelength reaches an equilibrium value but the phase size is increasing with time. Such classification depends on the system studied.

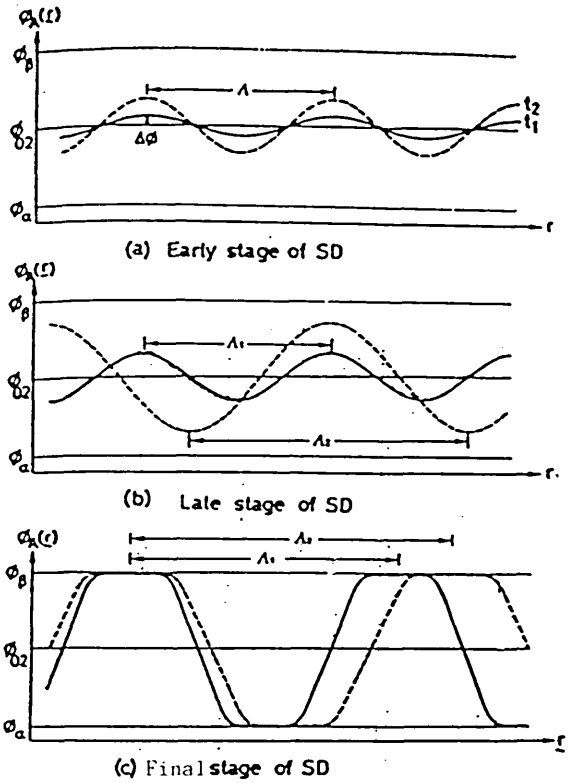


Fig.3.3 Three stages of spinodal decomposition:

a) early stages b) later stages. and

c) Final stages

3.3 Characteristics of spinodal decomposition

The characteristics of spinodal decomposition are as follows:

1. It is an unstable process; it requires no activation energy.
2. The local concentration which describes the spinodal system obeys a continuity equation. Thus the decomposition process is limited by diffusion. The diffusion is uphill and therefore the diffusion coefficient is negative.

3. The process starts by a continuous concentration fluctuation. Thus the two phases start out coherent with one another and a completely interconnected two phase structure results.

4. This process is an isothermal one, which implies no energy is needed or released.

3.4 Kinetics of spinodal decomposition

The dynamics of phase separation can be described by using the standard relations between thermodynamic variables and dynamic flux equations.

$$J(r) = - M \nabla(\mu_A - \mu_B) \qquad (3.2)$$

In this equation $J(r)$ is the interdiffusional flux. M, simply being the ratio of the diffusional flux to gradient in chemical potential, is defined as the diffusional mobility.

Thermodynamic considerations show that M must be positive if the diffusion which results spontaneously from the chemical potential gradient is to result in a decrease in free energy.

In the development of the theory Cahn[113] considered the free energy of an inhomogeneous system whose composition is slightly different from the average composition. For such a mixture the free energy is given as:

$$\overline{G} = \int [G(\phi) + K(\nabla\phi)^2] dv \qquad (3.3)$$

where $G(\phi)$ is regarded as free energy density of the homogeneous mixture with a composition ϕ and $K(\nabla\phi)$ describes the change in free energy density when a

composition gradient is introduced. ϕ is the volume fraction of one of the components in the mixture.

In the early stage of spinodal decomposition the stability of an initially homogeneous mixture to infinitesimal composition fluctuation is the only concern. Thus the gradient will also be infinitesimal and the second term in Equation (3.3) is sufficient to describe the contribution from the incipient surface between regions differing in composition. Taking the variational derivative of Equation (3.3), leads to:

$$(\mu_A - \mu_B) = \frac{\partial \overline{G}}{\partial \phi} = \frac{\partial G}{\partial \phi} - 2K\nabla^2\phi \tag{3.4}$$

Substituting Equation (3.4) into Equation (3.2), the following diffusion equation is obtained:

$$-J = M\nabla\left[\frac{\partial G}{\partial \phi} - 2K\nabla^2\phi\right] \tag{3.5}$$

While the relation between the free energy functional and continuity is given by

$$\frac{\partial \phi}{\partial t} = -\nabla J \tag{3.6}$$

By solving Equations (3.5) and (3.6) the following equation was obtained

$$\frac{\partial \phi}{\partial t} = -M\frac{\partial^2 G}{\partial \phi^2}\nabla^2\phi - 2MK\nabla^4\phi + \text{non linear term} \tag{3.7}$$

Equation (3.7) is the phenomenological Cahn – Hillard diffusion equation that forms the basis of the interpretation of spinodal decomposition. By comparison

with the normal diffusion equation $\left[\frac{\partial\phi}{\partial t} = M\nabla^2\phi)\right]$, the quantity $\left[-M\frac{\partial^2 G}{\partial\phi^2}\right]$ is identified as a Cahn – Hillard apparent diffusion coefficient, D_{app}.

If the non–linear term is ignored the solution to Equation (3.7) can be written, in terms of the growth in amplitude of concentration fluctuation, as:

$$\phi - \phi_0 = \sum_q [\exp [R(q).t][A(q) \cos(q.t) + B(q) \sin(q.t)] \tag{3.8}$$

Here A(q) and B(q) are the Fourier coefficients of a component of concentration fluctuation. q is the wave vector ($= 2\pi/\lambda m$). R(q), being the growth rate of each Fourier component of concentration fluctuation, is given by:

$$R(q) = M\left[-\frac{\partial^2 G}{\partial\phi^2}\right]q^2 - 2MKq^4 \tag{3.9}$$

According to the scattering theory the scattered intensity from such a system grows exponentially as:

$$I = I_0 \exp [R(q).t] \tag{3.10}$$

From Equation (3.9) the following characteristics can be seen:

1. Because K is restricted to non negative values, the sign of R(q) is governed by $\frac{\partial^2 G}{\partial\phi^2}$. Since within the spinodal region $\frac{\partial^2 G}{\partial\phi^2}$ is negative, R(q) will be positive for some wave vectors. Thus the phase separation should proceed spontaneously as expected. While within the metastable region, $\frac{\partial^2 G}{\partial\phi^2}$ is positive. Negative R(q) is obtained, thus no phase separation proceeds with a small concentration fluctuation.

2. Inside the spinodal there is a critical wave number, q_c, which forms the boundary between positive and negative R(q). This means at this critical wave number all the contributions to the free energy cancel each other out. Concentration fluctuation with q smaller then q_c can grow because R(q) will have a positive value, while the one with q larger than q_c cannot grow. q_c is given by:

$$q_c^2 = -\frac{\partial^2 G}{\partial \phi^2}/2K \tag{3.11}$$

3. For $q < q_c$ the growth rate R(q) has a maximum at

$$q_m^2 = -\frac{\partial^2 G}{\partial \phi^2}/4K \tag{3.12}$$

The maximum R(q) at q_m is equal to:

$$R(q) = M\left[\frac{\partial^2 G}{\partial \phi^2}\right]/8K \tag{3.13}$$

It can be seen that the growth rate, R(q), is governed by both the thermodynamic term, $\frac{\partial^2 G}{\partial \phi^2}$, and the transport property, M, of the system, while q_m is only determined by the thermodynamics of the system.

4. Because of the exponential nature of the concentration fluctuation (Equation (3.8)), the scale of the phase separation should be dominated by the most rapidly growing wave vector, q_m, so the correlation length is given by:

$$\lambda_m = \frac{2\pi}{q_m} = 2\sqrt{2}\pi\left[-\frac{1}{2K}\left[\frac{\partial^2 G}{\partial \phi^2}\right]\right]^{-\frac{1}{2}} \tag{3.14}$$

Based on F – H theory, Van Aaartsen[143] derived an equation which can be used to estimate λ_m. The equation is written as:

$$\lambda_m = 2\pi\ell\left[3(1-\frac{T}{T_s})\right]^{-\frac{1}{2}} \tag{3.15}$$

where ℓ is the range of molecular interaction

T_s is the spinodal temperature of the mixture.

5. The plot of $R(\phi)/q^2$ against q^2 should be a straight line with an intercept D_{app} and a slope of 2MK. The ratio of the intercept to the slope is given as:

$$\frac{D_{app}}{2MK} = \frac{-M\dfrac{\partial^2 G}{\partial \phi^2}}{2MK} = -\frac{\partial^2 G}{\partial \phi^2}/K = 2q_m^2 \tag{3.16}$$

At the spinodal point $\left[\dfrac{\partial^2 G}{\partial \phi^2}\right]_{T=T_s} = 0$, so that:

$$D_{app} = R(q_m) = 0 \tag{3.17}$$

From this simple relation the spinodal temperature can be obtained by extrapolating D_{app} to zero.

In summary, four of the main predictions of the C – H theory are:

1. Intensity increases exponentially with time with a growth rate 2R(q).
2. I(q) and R(q) have maxima at $q_m = \frac{1}{2}\left[-\dfrac{\partial^2 G}{\partial \phi^2}/K\right]^{\frac{1}{2}}$.

3. $R(q)/q^2$ varies linearly with q^2. The intercept is $D_{app} = -M.\frac{\partial^2 G}{\partial \phi^2}$ and the slope is $-2MK$, so that $q_m = (-\text{intercept}/2 \times \text{slope})^{\frac{1}{2}}$.

4. The intensity does not grow above a cut off, $q_c = \sqrt{2}q_m$.

3.5 Shortcomings of the Cahn – Hillard theory

Experimental results[96-99] have proven that the Cahn – Hillard theory is able to qualitatively predict the phase separation behaviour in the early stage of spinodal decomposition, but fails to quantitatively predict the behaviour of spinodal decomposition in the following aspects.

1. As the phase separation proceeds the q_m moves to smaller values, which were observed in several experiments[96-99]. This is not predicted by Cahn – Hillard theory.
2. Curved $\frac{R(q)}{q^2}$ plots against q^2 were obtained in experiments[96,97] in contradiction to the straight lines predicted by Cahn – Hillard theory.
3. The ratio of q_c/q_m observed in experiments are not in agreement with the theory, and in some cases the q_m obtained from $R(q)/q^2$ with q^2 plot shows reverse (week) temperature dependence[105].

The failures of Cahn – Hillard theory arise from its neglect of the thermal fluctuation force[115,144] and the non linear terms[145] as well as other effects such as the influence of other variables of motion[117] and wave number dependent mobility[116,118]. All these factors contributing to the failure of the Cahn – Hillard theory have been considered in several extended theories.

3.6. The extended theories

Following Cahn's linearised model, attempts have been made to describe the phase separation process by taking the neglected factors into consideration. In Langer *et al*'s treatment[145] the neglected non linear terms in C – H theory were taken into account. The phase separation process was described by using power law relations. The LBM theory[145] predicts the time (t) dependence of the average concentration correlation length (d_m) as:

$$d_m \propto t^{\phi} \quad (\phi = 0.212) \tag{3.18}$$

and the time dependence of the maximum scattering intensity as:

$$I_m \propto t^{\phi} \, (\phi = 0.81) \tag{3.19}$$

However these predictions are unfortunately not in agreement with experimental resuts[124] throughout the entire phase separation process. Kawaski and Ohta[123] (KO approach) included hydrodynamic and non–linear effects into their model. It eventually resulted in the same power law relation as LBM theory at short times when concentration gradients are small, and a linear relation between d_m and t at longer times when hydrodynamic effects may become important. Experimental results[124] have seemed to indicate that the KO approach is the most consistent.

Although the C – H theory has been used to interpret the results of unmixing in polymer blends, it was originally developed to treat unmixing phenomena in metal alloys and inorganic glasses which are characteristically different from polymers. Based on the repetitive model for the motion of

polymer chains and the extended F – H theory, De Gennes[118] and Pincus[119] formulated theories for spinodal decomposition. They derived an equation which can be regarded as the growth rate of the concentration fluctuation, R(q).

$$R(q) = \lambda(q)\left[\frac{1}{N\phi(1-\phi)} - 2\chi + \frac{\sigma^2 q^2}{36\phi(1-\phi)}\right] q^2 \qquad (3.19)$$

Here $\lambda(q)$ is the wave vector dependent Onsager coefficient. σ^2 is set equal to $6Rg^2/N$ with Rg as an apparent radius of gyration of the blend.

In fact, with K value equal to $\sigma^2/36\phi(1-\phi)$, Equation (3.19) is identical to Equation (3.9) except that the diffusional term in Equation (3.19) is wave vector dependent. This reflects the existence of long chains in polymer mixtures.

Wave vector dependent diffusional coefficients have been suggested as one of the reasons for the failure of Cahn – Hillard theory. Pincus[119] and Binder[116] have independently considered this problem. By considering the dynamic properties of one labeled chain in an entangled melt which undergoes rapid small amplitude local motions and slow large amplitude creep, the following form for the wave vector dependent diffusional coefficient of the Onsager coefficient, $\Lambda(q)$, was obtained.

$$\Lambda(q) = \phi(1-\phi)\frac{W d^2}{q^2 R_g^2}\left[1 - \exp(-q^2 R_g^2)\right] \qquad (3.20)$$

where W is the rate of motion of a subunit in the melt and d is the tube diameter in the reptation model[118]. Equation (3.20) has been derived for the symmetric case where $W_A = W_B$, $Rg_A = Rg_B$ and $d_A = d_B$ for the blend.

Binder[116] has obtained a slightly different $\Lambda(q)$, though the limiting behaviour at large and small q is the same. The equation is given by:

$$\Lambda(q) = \phi(1-\phi)\frac{2CWd^2}{q^2 R_g^2}\{1 - \frac{1}{q^2R_g^2}[1 - \exp(-q^2R_g^2)] \qquad (3.21)$$

where C is a constant of order unity.

The above two treatments were used by Higgins *et al*[105] in the analysis of data from spinodal decomposition in SCPE with PMMA blends. The results have indicated that Pincus's treatment seems to be the most satisfactory as far as this mixture is concerned.

The thermal fluctuation forces are dealt with by Cook[115]. In his approach an extra thermal noise term is added in Cahn – Hillard's model which implies that in addition to a flux produced by the gradient of a local chemical potential, there is an additional flux arising from the random thermal motion of atoms. Experimental results have not favoured Cook's treatment.

Following Cook's model, Binder[116] derived the following equation for the concentration fluctuation, written as:

$$\frac{d\delta\phi_q(t)}{dt} = \Lambda(q)\left[\frac{1}{N\phi(1-\phi)} - 2\chi + \frac{\sigma^2q^2}{36\phi(1-\phi)}\right]\delta\phi_q(t)q^2 + \eta_q(t) \qquad (3.22)$$

where $\eta_q(t)$ is the thermal noise.

The solution of the above equation yields the equation of motion for the structural factor, S(q,t), as:

$$\frac{d}{dt}S(q.t) = 2\Lambda(q)\left[\left\{\frac{1}{N\phi(1-\phi)} - 2x + \frac{\Sigma^2q^2}{18\phi(1-\phi)}\right\}S(q.t) - 1\right]q^2 \qquad (3.23)$$

However, this equation is valid only in the small q range where $q << Rg^{-1}$.

Subsequently Binder generalised the De Gennes's equation of motion[118] and extended Equation (3.23) to a larger q range yielding:

$$\frac{d}{dt}S(q.t) = -2\Lambda(q)S_x^{-1}(q)[S(q.t) - S_x(q)]q^2 \qquad (3.24)$$

where $S_x(q)$, known as the "virtual structural factor", is defined by:

$$S_x^{-1}(q) = \frac{1}{N\phi(1-\phi)} f_0^{-1}(q^2Rg^2) - 2\chi \qquad (3.25)$$

where f_0 is the Debye structure factor of non − interacting ideal chains, given as:

$$f_0 = \frac{2}{q^2Rg^2}\left[1 - \left[1 - \exp^{(q^2Rg^2)}\right]/q^2R_g^2\right] \qquad (3.26)$$

The solution to Equation (3.23) has the typical form of an irreversible equation of motion given by:

$$S(q.t) = S_x(q) + [S(q.o) - S_x(q)]\exp^{[2R(q)t]} \qquad (3.27)$$

where
$$R(q) = -\Lambda(q)S_x^{-1}(q).q^2 \qquad (3.28)$$

Equation (3.27) describes the behaviour of the system from an arbitrary initial state, S(q.o), away from the equilibrium to the final state, $S_x(q)$. In the one phase region $S_x(q)$ represents the structure factor in thermal equilibrium. In the spinodal region it corresponds to a "virtual structural factor"; unlike the true equilibrium structure factor which has to be always positive, the "virtual structure factor" can take negative values. Through numerical calculations

Strobl[146] has shown that $S_x(q)$, given by Equation (3.25), is negative for smaller wave vectors, $q < q_c$, and positive for larger wave vectors, $q > q_c$. It shows a singularity at $q = q_c$.

Experimentally the virtual structural factor has been determined by an extrapolation procedure[104] and numerical methods[94]. The results from these two methods give a qualitative agreement.

Chapter 4

MATERIALS AND EXPERIMENTAL

4.1 Choice of system

There is an increasing interest in being able to mix high temperature thermoplastics with cheap and low temperature thermoplastics in order to achieve some cost effective, easily processable polymer blends. Two blends of polystyrene (PS) with tetra methyl bisphenol–A polycarbonate (TMPC) and poly (ether suphone) (PES) with poly (ethylene oxide) (PEO) studied in this project are well placed in this catalogue.

4.1.1 TMPC/PS system

The miscibility of polystyrene with tetramethyl bisphenol–A polycarbonate (TMPC) was first reported by Shaw[147] who observed features which suggested LCST behaviour. In a more extensive study, Casper and Morbitzer[148] constructed a complete phase diagram for this system. Yet again by using DSC and thermal analysis a complete cloud point curve was established and LCST behaviour was noted. Yee and Maxwell[149] reported results of DSC, density and dynamic mechanical measurements for this blend. Similar measurements were also made by Fernandes[150] *et al.* In the study of interaction parameter by neutron scattering, Brereton[151] noticed some rather peculiar behaviour for the interactions between TMPC and PS, which were interpreted as arising from a spatial structure existing in the system.

The main reasons for studying this blend are as follows.

1. The mechanism of miscibility between polystyrene and TMPC is not very well understood. Further studies would enable us to elaborate this mechanism.
2. Our preliminary experiments had shown that the phase separation process in this blend was slow enough to experimentally study the early stages of spinodal decomposition in this blend, through which further information about the blend can be obtained.
3. TMPC is a high temperature, expensive polymer. The blending of PS with TMPC may result in polymer blends with good mechanical properties and low costs.

4.1.2 PES/PEO system

The miscibility of PES with PEO was suggested in a patent[152]. At some compositions the two polymers form clear films when cast from a mixed solvent of N–methyl–2–pyrrolidone/methylene chloride. At other compositions the mixtures were cloudy. The clear film became cloudy on heating which suggested LCST behaviour of the blend. In another patent[153] it was shown that when blends of PES and PEO were cast from dimethylformamide at 50^{0}C a two phase blend was obtained. Singh[154] was the first to study this blend in detail. The results showed that PES/PEO when cast from dimethyl formamide gave a transparent film in the whole concentration range if crystallisation of PEO is absent. LCST behaviour was observed with a critical point at 10% of PES. A negative interaction parameter was obtained from heats of mixing measurements as well as from melting point depression and water absorption. DSC results also indicated that intermediate glass transition temperatures

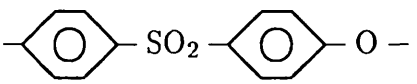
existed between two components, which supported the assumption of miscibility of PES and PEO. In all the work done, no explanation was given for the miscibility of PES with PEO. It could be postulated that miscibility may be due to the specific interaction between ether groups in PEO and aromatic rings in PES, for example, n $-$ π interactions.

There are two main reasons for wanting to study this blend. Firstly, PES is a new high temperature engineering plastic and blends with PEO may open some novel applications such as in ultrafiltration, reverse osmosis and medical dose release etc. Since in all these applications the microstructure of the blends are essential, a study of kinetics of phase separation of the blend would be desirable. Secondly, PEO is a crystallisable polymer, when mixed with PES, the crystallisation behaviour changes. Understanding the thermodynamics of this behaviour may be useful to envisage the miscibility of the system.

4.2 Materials

Poly (ether sulphone), PES

PES is a high temperature engineering plastic with a repeat unit.



Because of its aromatic character and the presence of the sulphone group which increases the stiffness of the chain, the polymer has very good mechanical and electrical properties even at high temperatures (up to 200^{0}C). PES is used in the electrical, mechanical, automobile and aircraft industries. It is also used

for ultrafiltration membranes, medical appliances and in food processing industries.

PES used in this study was kindly supplied by ICI (Victrex 200p). It has a quoted reduced viscosity of 0.41 $cm^3\ g^{-1}$ in a 1% solution in dimethyformamide (DMF) at 25°C, a density of 1.37 g/cm^3 at 25°C, a refractive index of 1.65 and a Tg of 226°C. The quoted number average molecular weight was 1765 g $mole^{-1}$ and thus the degree of polymerisation was approximately 76. It was dried in an oven before use (150°C, 5 hrs.)

Poly (ethylene oxide)(PEO)

PEO is a liquid or wax at low molecular weight and a crystalline low melting point solid at higher molecular weight. It has a repeat unit of $(-CH_2 - CH_2 - O-)_n$. The PEO used in this work was obtained from BP Chemicals (Carbowax M20) with a quoted molecular weight of 15,000 to 20, 000 g/mole and a density of 1.065 g/cm^3.

Tetramethyl bis–phenol–A polycarbonate, (TMPC)

TMPC was kindly supplied by BASF (West Germany) with a quoted reduced viscosity of 1.296 $cm^3\ g^{-1}$ in 0.5% CH_2Cl_2 solution at 25°C. The molecular weights measured by GPC in THF solvent are

$$M_n = 1.79 \times 10^4, \quad M_w = 5.26 \times 10^4, \quad \frac{M_w}{M_n} = 2.94$$

Polystyrene (PS)

Polystyrene with different molecular weights was used in the study. Their characteristics are listed in Table 4.1.

Table 4.1 Characteristics of polystyrene used

Sample Code	M_w	M_n	$\frac{M_w}{M_n}$	Tg
PS-3	3.18×10^5	1.36×10^5	2.34	99°C
PS-5	2.89×10^5	1.13×10^5	2.56	99°C
PS-7	1.02×10^5	6.37×10^4	1.60	99°C

4.3 Blend preparation

Various methods are available to prepare a homogeneous blend and each method is unique in its approach to mixing polymer components. In this study solvent casting was mainly used.

4.3.1 Preparation of TMPC/PS blends

TMPC/PS blends were prepared by dissolving a desired amount of the two components (in the required proportions) in CH_2Cl_2 to form a 5% (W/V) solution. The solution made was centrifuged for 30 min. in an angle head centrifuge (Galenkamp). Several drops of centrifuged solution were placed on cover slips excluding dust and grease. The cover slips were put in a petri dish which excludes dust and allows slow evaporation of the solvent. When most of the solvent was evaporated, the petri dish was transferred into a vacuum oven at 80°C for 48 hrs and then 130°C for 24 hrs. to ensure the complete removal of all traces of solvent. The removal of solvent was checked by repeated weighing of the petri dish over a period of time. Different thicknesses of films were

prepared by using solutions of different concentrations. Typically, films used in kinetic studies were of 0.2 – 0.3 mm in thickness. In the beginning of the preparation benzene and THF were also tried as solvents. Freeze–drying and co–precipitation of benzene solution of this blend were also utilised. Freeze–drying was conducted with the use of 2% (W/V) benzene solution in the set–up shown in Figure 4.1. The resulting powder was further dried in vacuum

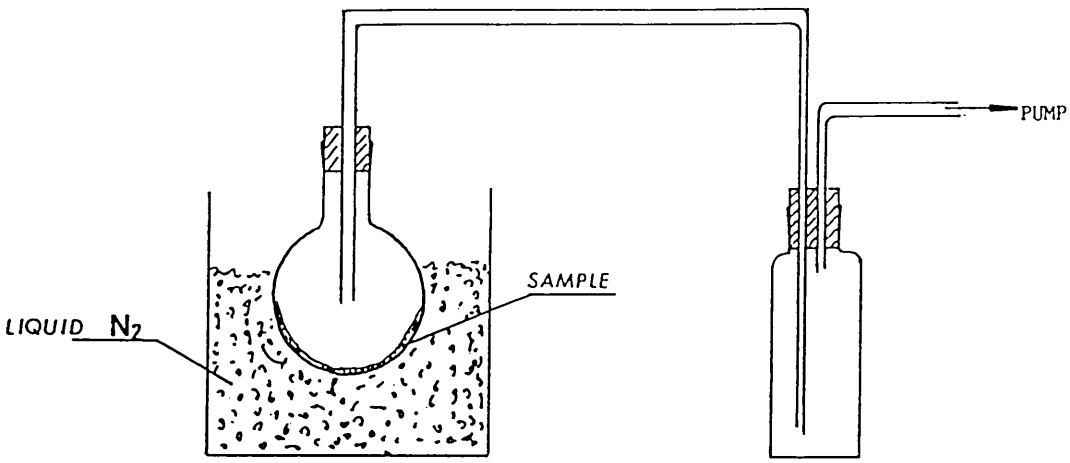


Fig.4.1 The experimental set–up for freeze–drying.

at 80°C for 24 hrs. In the co–precipitation of 5% (W/V) benzene solution methanol was used as a non–solvent. The powder mixture from the precipitation was dried in vacuum at 80°C for 24 hrs.

4.3.2 Preparation of PES/PEO

Before the preparation, poly(ethylene oxide) and PES were dried under vacuum for 7 days. Dried PES and PEO were dissolved in dimethylformamide with the desired amount of each component to form a 5% (w/v) solution. The solution was centrifuged for 30 min. Several drops of the solution were placed on cover slips which were put inside a petri dish. Due to the higher absorption

of moisture of PEO, which could result in cloudy films, the petri dish was directly transferred into a vacuum oven at 60°C in order to exclude the moisture and to dry the film. This also prevented the PEO from crystallisation. After three days in the oven the film was dried. This was confirmed by the stabilisation of weight of the petri dish. The typical thickness of the film was $0.2 - 0.3$ mm.

4.4 Methods of establishing miscibility and cloud points

Several different techniques, such as the presence of single glass transition temperature and optical clarity, can be used to establish the miscibility and phase separation of polymer blends. In some cases one method can give misleading information and therefore more than one method should be used to confirm the miscibility and phase separation phenomenon.

4.4.1 Optical clarity

Films made from solution casting of polymer blends were firstly assessed for optical clarity by visual observation as well as optical microscopy. This is the first indication of miscibility but not a sufficient proof. In practice it is always advantageous to place the film on a dark surface in the visual observation in order to enhance contrast.

4.4.1 Differential scanning calorimetry (DSC)

The blends were examined by differential scanning calorimetry (Perkin–Elmer DSC–II) in order to obtain their glass transition temperatures

and melting temperatures. For TMPC/PS blends sample weights were about 10 mg. A nitrogen flow was maintained through the sample chamber. An empty aluminium sample pan was used as a reference. The samples were scanned from 40^{0}C to 300^{0}C. The Tg was arbitrarily taken to be the temperature at which the change in heat capacity is one half of the transition. For each composition three samples were run and the average of the three values was taken. The estimated error of the value is ±2^{0}C. For all the experiments done here a heating rate of 20^{0}C/min was used.

The glass transition measurements of PES/PEO blends were conducted in a similar way as for the TMPC/PS system. In the study of crystallisation behaviour of this blend by DSC, weighed samples (= 10 mg) were heated, after melting at 80^{0}C for 10 mins, then quickly cooled down to various crystallisation temperatures, T_c, and crystallised for different times. The melting heat of the crystal formed at T_c was determined as a function of crystallisation time. The fraction of crystallised polymer after time t was determined by means of the relation

$$x_t = \int_0^t \left[\frac{dH}{dt}\right] dt / \int_0^\infty \left[\frac{dH}{dt}\right] dt \qquad (4.1)$$

where the first integral is the heat generated at time t and the second is the total heat of melting at $t = \infty$.

The integrals above correspond to areas of the individual melting peak above the baseline of the graph. The area of the melting peak was measured by cutting the peak and weighing. For each sample three measurements were made. Due to various errors involved in the measurements the accuracy of the measured value was estimated to be 5%.

The observed melting temperature T_m of the isothermally crystallised blends were measured by heating the sample from T_c to 80^0C with a heating rate of 10^0C/min. The peak temperature was taken as the melting temperature. The DSC was calibrated with Indium before measurements.

4.4.3 Optical microscopy

An optical microscope (Olympus BHB), fitted with a hot stage, was used to determine cloud points and study the phase structure on heating and cooling. For TMPC/PS, samples were placed in the hot stage at a pre–determined temperature for 30 minutes and then taken out for observation under the microscope. The pre–determined temperature was increased by 5^0C each time. This procedure was repeated until a temperature was found at which a mixture just started to phase separate. Phase separated structures at different temperature and different times were also taken by using the camera on the microscope.

4.4.4 Light scattering

Light scattering experiments were conducted in a modified light scattering equipment which is described below.

4.4.4.1 The modified light scattering equipment

In order to accommodate the quick pressure–release diamond anvil cells, described in Chapter 6, into the equipment and allow more flexibility in the use

of the equipment, modifications of the previous light scattering equipment designed by Hill[107] were made.

A. **The previous design**

Basically the design consists of three parts: the optical system, the detection system and the data collecting system. The beam from a horizontally mounted He–Ne laser (5mW) is turned into vertical by using a prism. The laser beam passing vertically through the sample, which is held at a controlled temperature, is scattered at different angles. The scattered light is detected by using photodiodes mounted over a 60^0 angle range with 2^0 intervals. The signals from the photodiodes are converted into digital values through a multi–channel A/D convertor and collected by a BBC computer. The optical system and the detection system are fixed in one frame and placed inside a light–proof box.

B. **Modifications made**

The main modifications involved the optical system and the sample block. These are separately described below.

B.1 **The optical system**

The following modifications were made in the optical system.

1. The horizontal laser assembly in the previous design was changed to a vertical laser assembly. Thus no prisms were used in this optical system. This arrangement could reduce the parasitic scattering from the optical system and allow easier alignment.

2. In order to reduce the beam size to smaller than the size of the diamond anvil (details in Chapter 6) in the pressure cell, a lens was used together with a diagrapham. The diagrapham was introduced to eliminate unwanted scattered light from the optical system.

3. The optical system assembly was separated from the detection system. This allows more flexible use of the expensive detection system.

4. The change from the horizontal assembly to the vertical assembly of the optical system was accomplished by a new design of the supporting base for the laser and the pressure cell. The vertical assemby was accomplished by clamping the laser onto a frame connected to the supporting base. The supporting base was mounted onto two vertical steel bars fixed on a heavy base that could be moved upwards or downwards as required. For the sake of easy optical alignment, three dimensional positioning mechanisms were introduced into the laser clamping frame. The whole assembly is schematically shown in Figure 4.2. The base, shown in Figure 4.3, was designed to hold the pressure cell and the three screws along the ring and could be used to position the pressure cell in optical alignment with the laser beam. The base was assembled on the vertical bars and could be fixed in any required position along them.

B.2 Heating system

Poor insulation of the previous sample block had prevented higher maximum temperatures being achieved. The maximum temperature obtained in the block is 200^{0}C, which is below the phase separation temperature of TMPC/PS blends. Thus a new sample block was constructed. In the new design a sample block with a smaller heating mass was made and

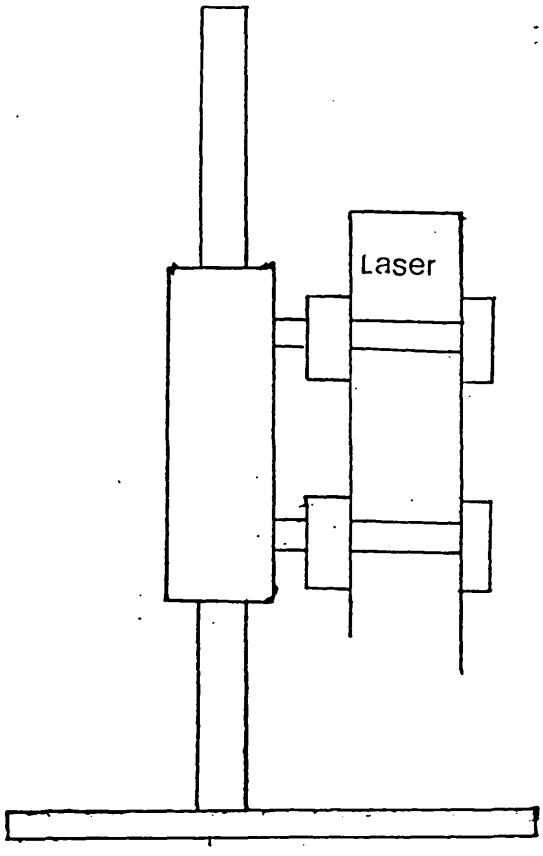


Fig.4.2 A schematic drawing of the assembly frame of the He/Ne laser.

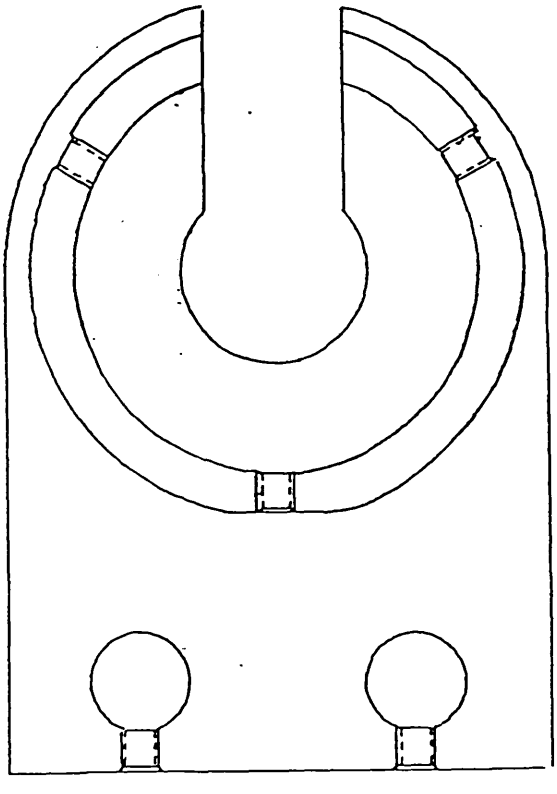


Fig.4.3 A schematic drawing of the assembly base of the diamond anvil pressure cell.

poly(tetrafluroethylene)(PTFE) was used to insulate the sample block as it has a higher utilisation temperature and better insulation properties than the previous insulation material, Tefnon. In order to prevent distortion of PTFE at high temperature the constructed block was attached to a strong stainless steel base. Nitrogen gas could also be introduced into the block to prevent polymer degradation via oxidation at higher temperatures. The constructed sample block is schematically shown in Figure 4.4. The maximum temperature achieved in the block is 300^{0}C.

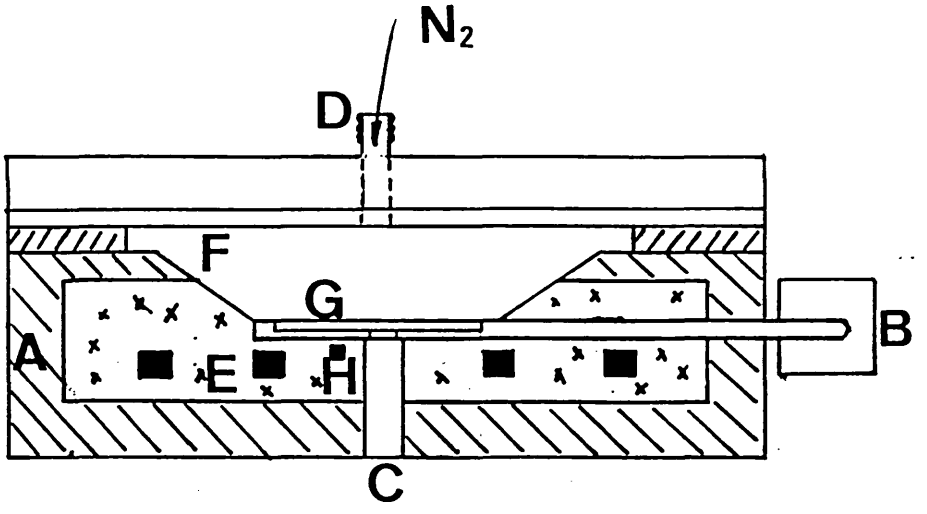


Fig.4.4 A schematic illustration of the newly–built heating block.
A: PTFE insulation layer, B: Sample holder, C: Laser inlet,
D: Nitrogen gas inlet, E: Iron heating smoulder,
F: Insulation layer, G: Sample, H: Thermocouple.

For the construction of the modified LS equipment a new 5 mw laser (Aerotech Ltd) and photodiodes (RS Ltd) were purchased. Their characteristics are listed in Table 4.2 and Table 4.3 The constructed equipment is schematically shown in Figure 4.5 To comply with safety regulations and prevent dust from entering the optical system, the apparatus is enclosed in a light–proof box.

Table 4.3 Characteristics of the He-Ne laser

Parameter	Typical Value
Minimum output power at 6328 Å	5 mw
Beam Diameter	0.64mm
Output power drift in 24 Hrs	< ± 5%
Spatial mode	TEMoo

Table 4.2 Characteristics of the BS photodiode

Parameter	Typical value
Sensitivity	60mv/μw/cm
Rise time	50 μs
Fall time	50 μs
Dark level temperature coefficient	150 μv/°C
O/P noise voltage	1mv.rms

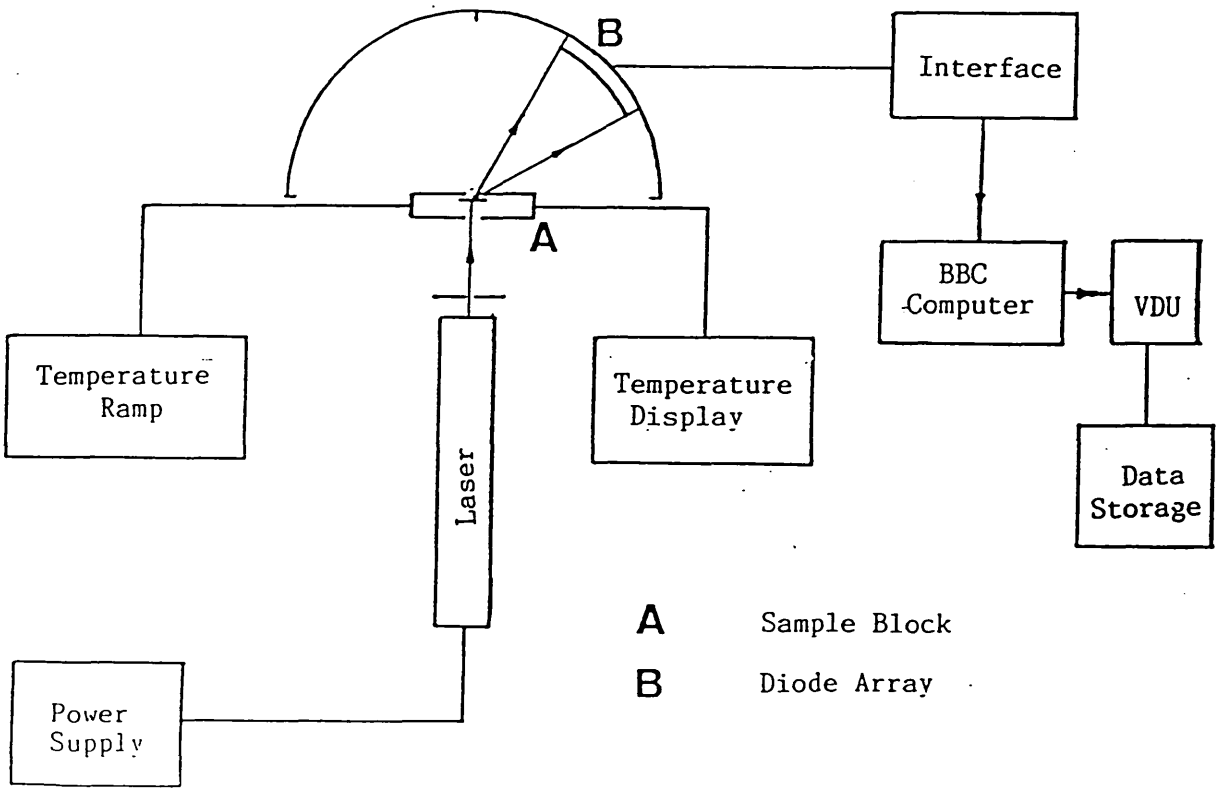


Fig.4.5 A schematic illustration of the light scattering equipment.

4.4.4.2 Experimental procedures

Phase boundaries of the blends were obtained by measuring scattered light intensity from the sample using the above described equipment. Films of the blend were placed in a sample holder which is thermostatically controlled. The intensity of scattered light was measured over a range of 60^0 degrees using a photodiode array.

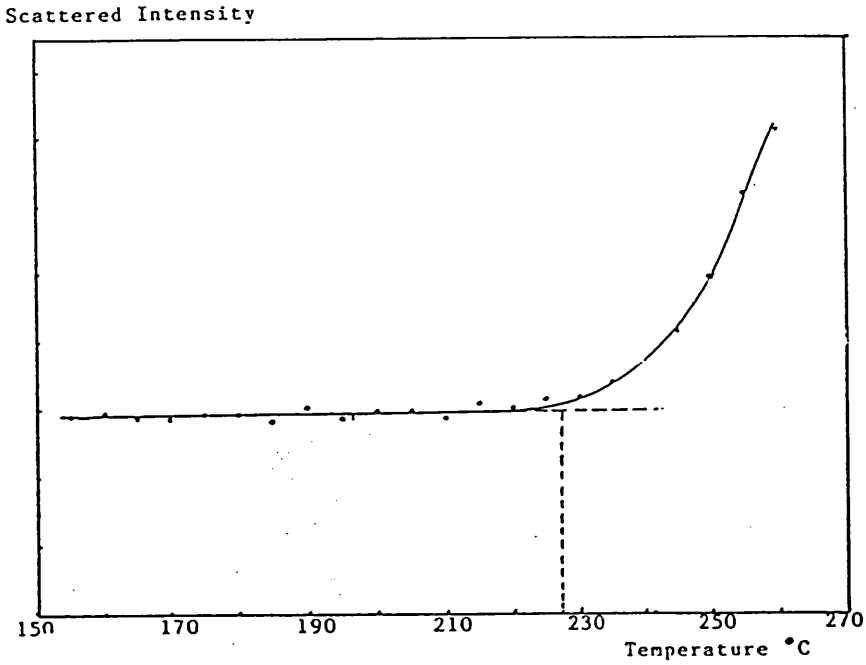


Fig.4.6 A typical plot of determination of cloud points.

The temperature of the sample holder was altered at a controlled rate and a plot of scattered light intensity against temperature was obtained. At the cloud point the intensity increases. The onset of the intensity increase in the plot was taken as the cloud point, as shown in Fig. 4.6. Repeated experiments show that the cloud points determined could vary within $\pm 2^0$C.

The scattered light intensity of PES/PEO mixtures was also examined as a function of time at a constant temperature. Different scattering behaviour in nucleation and growth and spinodal decomposition was utilised to roughly

determine the spinodal temperature of the system. The temperature was altered at 0.5^{0}C intervals. The temperature where the transition from gradual intensity increase (nucleation and growth mechanism) to exponential (spinodal decomposition) increase occurs was taken as the spinodal temperature. The observed spinodal temperature may vary within ±0.5^{0}C due to the various errors involved.

In kinetic experiments, dried films of TMPC/PS (50/50) with a thickness of about 0.3 mm were preheated at 230^{0}C for 30 minutes and then quickly transferred into the sample block. The temperature of the sample block was controlled at the phase separation temperature with an error of ±0.5^{0}C. From our preliminary experiments an effect of the pre–heating temperature on phase separation was noticed, so the pre–heating temperature in the experiment was carefully controlled within an error of ±2^{0}C. In order to prevent PS degradation at high temperatures N_2 was introduced in the sample block with a controlled flow rate. The time needed to reach the phase separation temperature from 230^{0}C was estimated to be about 20 secs. for a temperature jump of 10^{0}C. From the experimental data the region between 20 secs. to 100 secs. was taken as the early stages of spinodal decomposition. The data were analysed using a Fortran programme on an IBM–PC.

In the experiments of PES/PEO (10/90) a pre–heating temperature of 75^{0}C was used in order to shorten the temperature jump and prevent crystallisation of PEO. It is estimated that 5 secs. is required to reach the phase separation temperature. The region of 5 – 30 secs. was taken as the early stage of spinodal decomposition.

The wavevector, q, was calculated from the equation:

$$q = \frac{4\pi n \sin \frac{\theta}{2}}{\lambda} \tag{4.2}$$

with $\lambda = 6328$Å and n the refractive index of the mixture (1.60 for the TMPC/PS mixture and 1.58 for the PES/PEO mixture), $\frac{\theta}{2}$ is the scattering angle.

CHAPTER 5

RESULTS AND DISCUSSION

In this chapter results obtained for the TMPC/PS system and PES/PEO system are presented and discussed.

5.1 TMPC/PC system

5.1.1 Thermodynamic miscibility

A. Film clarity

In the initial experiments, THF, benzene and ethylene chloride were used as common solvents for the mixture. Films prepared from ethylene chloride and benzene solution are all clear, while films made from THF solution are cloudy. This observation is in agreement with Paul's results[150]. The occurrence of cloudy films prepared from THF solution is thought to be due to the crystallisation of TMPC during the drying process. The absence of crystallisation in films prepared from ethylene chloride solution may have resulted from the lower boiling point of the solvent. The clarity of films prepared from ethylene chloride indicates that TMPC and PS may be miscible.

B. Glass transition temperature of the mixture

The glass transition temperatures measured in DSC are plotted in Fig. 5.1 and Fig. 5.2. In Fig. 5.1, DSC thermograms of the mixture are shown. For all the mixtures tested a single intermediate T_g is observed as has been seen by

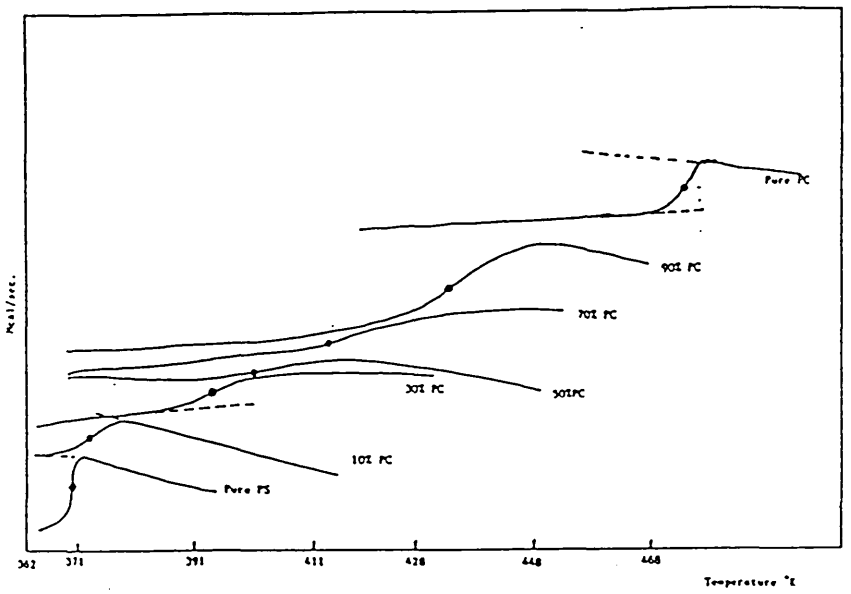


Fig.5.1 Plots of DSC thermograms of heat capacities against temperature for blends of TMPC with PS.

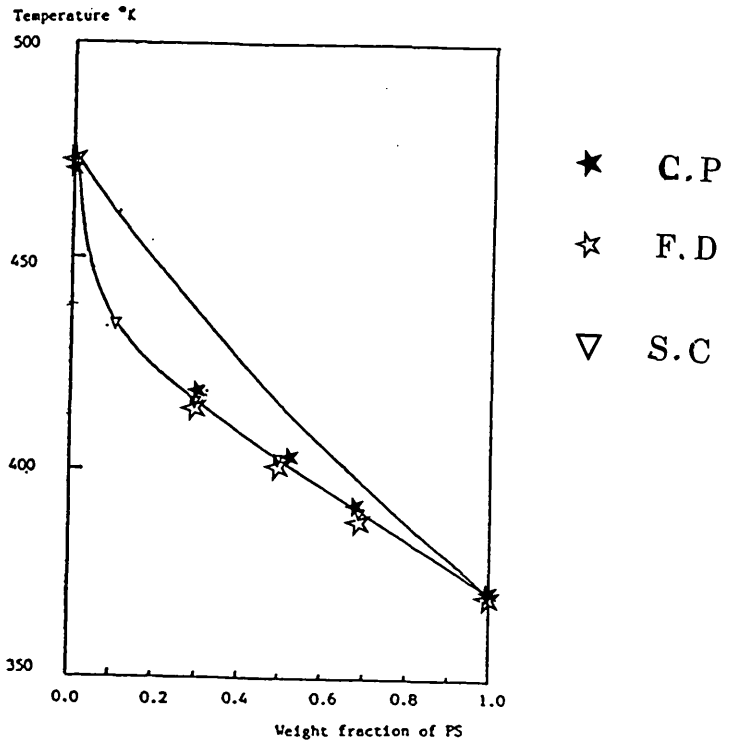


Fig.5.2 Plots of glass transition temperature of TMPC/PS–5 mixtures. The solid curve is plotted according to the Fox equation. △ experimental results.

other authors[148-150]. This again indicates the miscibility of these two polymers. The predicted values of T_g, using the Fox equation[37], written as

$$\frac{1}{T_g} = \frac{w_1}{T_{g1}} + \frac{w_2}{T_{g2}} \tag{5.1}$$

are plotted together with the experimental value in Fig. 5.2.

The predicted values are not in agreement with the experimental results. Similar observations are also noted in other mixtures. The disagreement indicates the invalidity of the Fox equation predicting T_g's of miscible polymer blends.

Also shown in Fig. 5.2 are the results obtained from samples prepared by freeze–drying and coprecipitation. Within experimental error no difference in the glass transition temperature among three preparation methods is observed. This may indicate that the miscibility of TMPC and PS is independent of the preparation method.

In Fig. 5.1, broadening of the width of the glass transition zone in the mixture may also be seen. The width of the glass transition of the pure TMPC and PS is about 10K, while about 20K is observed for mixtures. This may be indicative that miscibility does not occur at the molecular level[6]. It may also be due to micro heterogeneities where local composition fluctuations are in excess of normal density and temperature fluctuation[5].

It has been speculated that the interactions between PS and TMPC resulting from the electric effects of methyl groups in TMPC may be similar to those for PS and poly(phenylene oxide) whose structure is similar to that of TMPC. Spectroscopic data[155] has indicated that special conformational changes as a consequence of the interaction between the phenyl ring of the PS and the phenylene ring in the PPO have occurred in the mixture, while the absence of a

minimum T_g in Fig. 5.2 may indicate that such specific interaction may not be very strong.

All the results discussed above are listed in Table 5.1.

Table 5.1 Glass transition temperatures of TMPC/PS-5 blends

Concentration	Experimental (^{0}K)			Theoretical (Fox equation) (^{0}K)
	S.C*	F.D*	C.P*	
pure TMPC	473	473	473	473
90% TMPC	434	-	-	460
70% TMPC	418	418	416	437
50% TMPC	403	406	404	416
30% TMPC	391	403	400	396
10% TMPC	375	372	374	379
Pure PS	370	370	370	370

* S.C--Solution Casting,F.D--Freeze Drying,C.P-- Coprecipation

C. Cloud point curves

C.1 The effect of heating rate

Cloud points of 50/50 TMPC/PS–5 mixtures, determined using the light scattering equipment at different heating rates, are depicted in Fig. 5.3. Clearly the cloud points increase almost linearly with the increasing heating rates. This is caused by small diffusional coefficients of highly viscous polymer molecules. By extrapolation the cloud point at isothermal conditions (zero heating rate) may be obtained. The resulting temperature of 234^{0}C is in good agreement with the value determined by microscopic methods (235^{0}C) and the spinodal temperature 233^{0}C by kinetic experiments (Figs. 5–13).

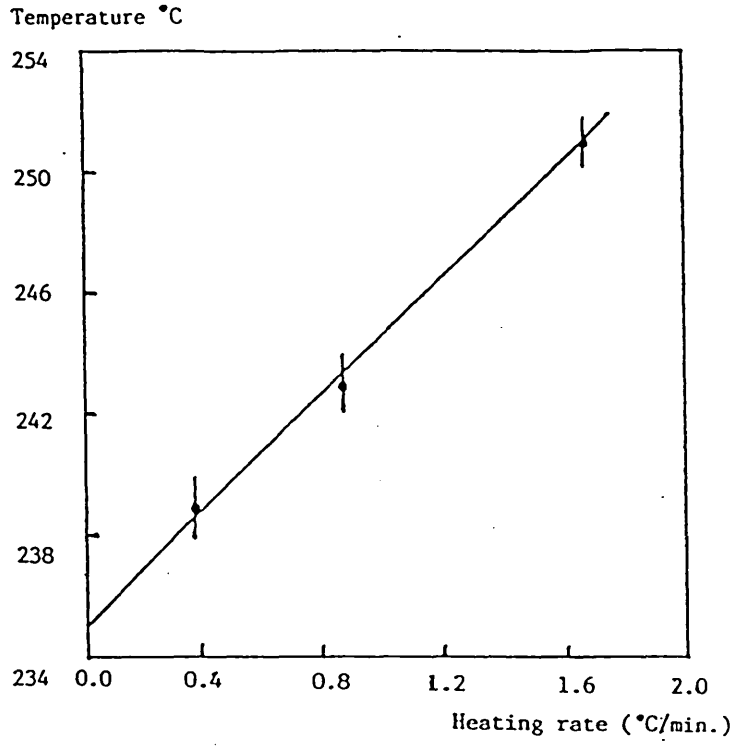


Fig.5.3 Effect of heating rates on the cloud points of TMPC/PS (50/50) mixture.

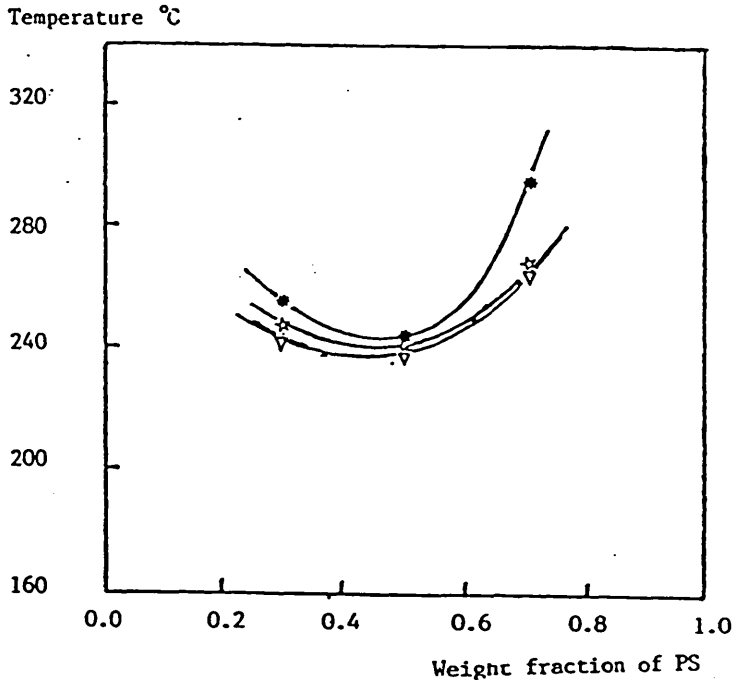


Fig.5.4 Cloud point curves for TMPC/PS mixtures with different molecular weights of PS, determined by using the light scattering technique. * ——PS–3 ☆——PS–5 ▽——PS–7 (heating rate = 0.4°C/min).

C.2 Effect of molecular weights

Cloud point curves of mixtures having different molecular weights of PS are plotted in Fig. 5.4. Owing to the degradation of PS at higher temperatures the extremes of molecular weights of PS are not used. From the figure a small decrease of cloud point is observed as the molecular weight of PS increases. This is due to the decrease of the combinatorial entropy term in ΔG_m and the free volume with the increase of molecular weights. The relatively small effects of molecular weights observed here may suggest that entanglements between different chains are involved to such an extent that they have hindered the phase separation process, although phase separation is favoured on thermodynamic grounds.

C.3 Effects of the film thickness

The effect of the film thickness on experimental results in light scattering has been noted[96]. However, no experimental evidence is available until the present. The cloud points measured on 50/50 TMPC/PS–3 films of different thicknesses are presented in Fig. 5.5. With the increase of the film

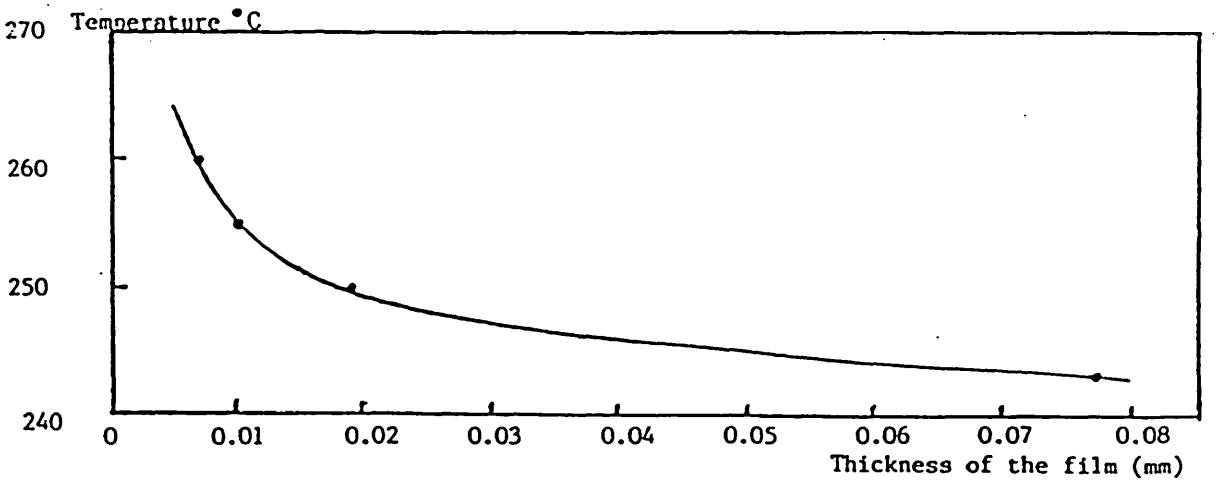


Fig.5.5 Effects of film thicknesses on the cloud points of TMPC/PS–5 (50/50) mixture.

thickness the cloud point decreases dramatically at first and then levels off. This may be caused by the existence of more scattering particles in thicker films. A significant signal (needed to observe cloud point) can be achieved in earlier times with a thicker films. The cloud points obtained in various conditions are tablulated in Table 5.2 and Table 5.3.

Table 5.2 Effects of heating rates, film thicknesses on cloud points of TMPC/PS-5 (50/50) blends

Heating Rate (°C/min)	Film thickness (mm)	Cloud points (°C)
1.67	> 0.08	251 ± 2
0.87	> 0.08	243 ± 2
0.38	> 0.08	239 ± 2
0.38	0.007	260 ± 2
0.38	0.01	255 ± 2
0.38	0.019	250 ± 2
0.38	0.077	244 ± 2

Table 5.3 Effects of molecular weights of PS on the cloud point of TMPC/PS blends

Code of PS	Concentration TMPC %	Cloud points (°C) by Scattering	By Microscopy
PS-3	70	267 ± 2	250 ± 2
	50	240 ± 2	235 ± 2
	30	244 ± 2	242 ± 2
PS-5	70	264 ± 2	250 ± 2
	50	241 ± 2	235 ± 2
	30	250 ± 2	240 ± 2
PS-7	70	255 ± 2	260 ± 2
	50	243 ± 2	235 ± 2
	30	>285	240 ± 2

D. Optical microscopy

Differential interference microscopy was used to measure the phase boundary and to observe the phase separated structures of this blend. The phase boundary determined is shown in Fig. 5.6. Despite the fact of different

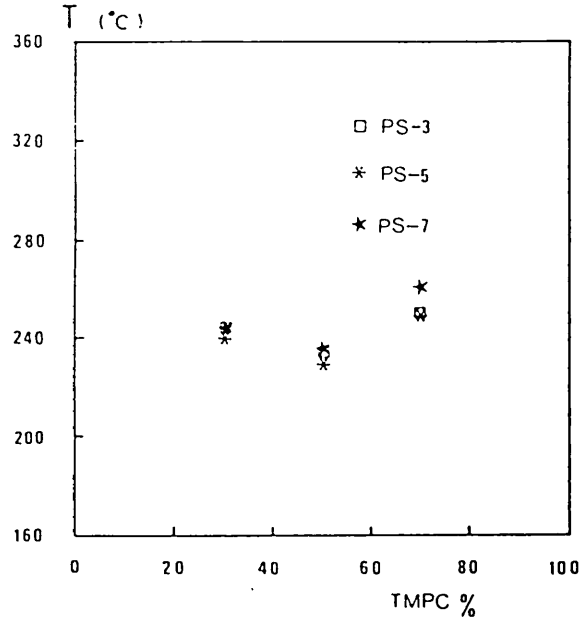
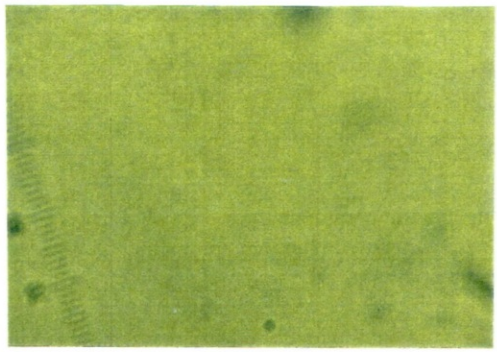


Fig.5.6 Cloud points determined by microscopic methods.

techniques being used the phase boundary determined by optical microscopy and light scattering gives a fairly good agreement.

In the study of phase separated structures of the blend an interconnected morphology with a diffuse interface was observed at early times(Fig. 5.7)

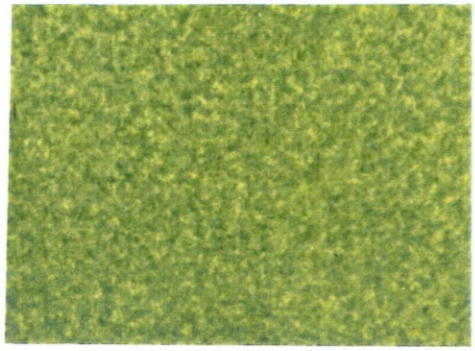
Later the wavelength of the system becomes longer and the interface sharper. An interconnected structure has often been cited as evidence for spinodal decomposition having taken place. During the time period that the exponential increase of scattered intensity starts to deviate (see Fig. 5.9 in section of kinetics of phase separation) the interconnected morphology can still be seen. The observation may indicate that the power law relation describing the later stages of spinodal decomposition may not apply.



240°C 10 mins.



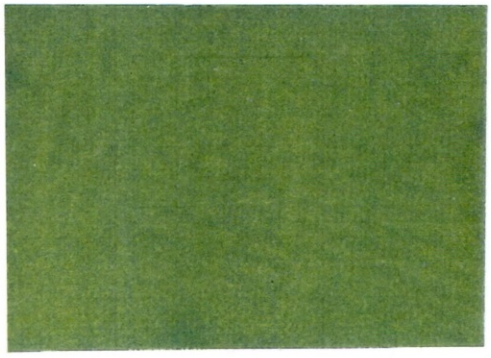
250°C, 10 mins.



260°C 10 mins.



270°C, 10 mins.



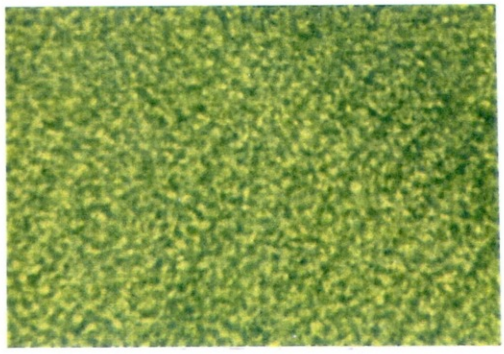
250°C, 8mins



250°C, 13mins



250°C, 20mins.



250°C, 27mins.

Fig.5.7 Photographic pictures of the phase separated TMPC/PS–5 mixture at different temperatures and times.

5.1.2 Kinetics of phase separation

Fig. 5.8 shows the evolution of the scattered intensity from a TMPC/PS–5 (50/50) sample after a temperature jump into the two phase

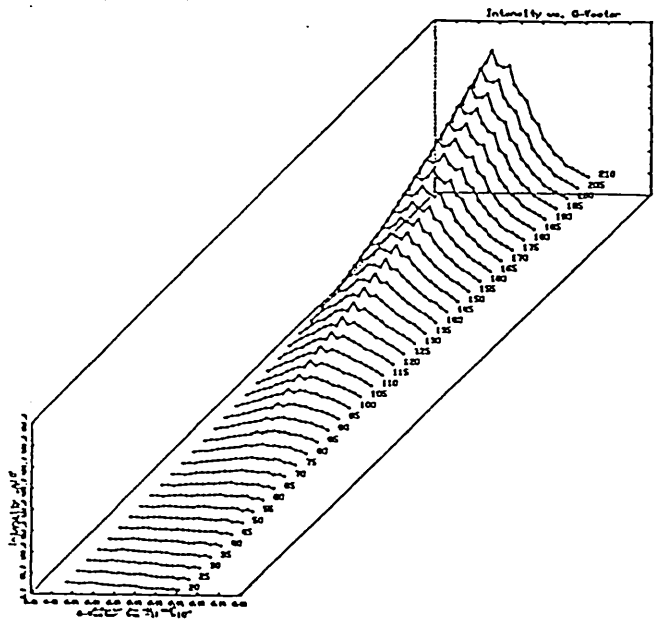


Fig.5.8 A typical series of I(Q) plots at different times within the spinodal for TMPC/PS–5 (50/50) mixture at 242°C.

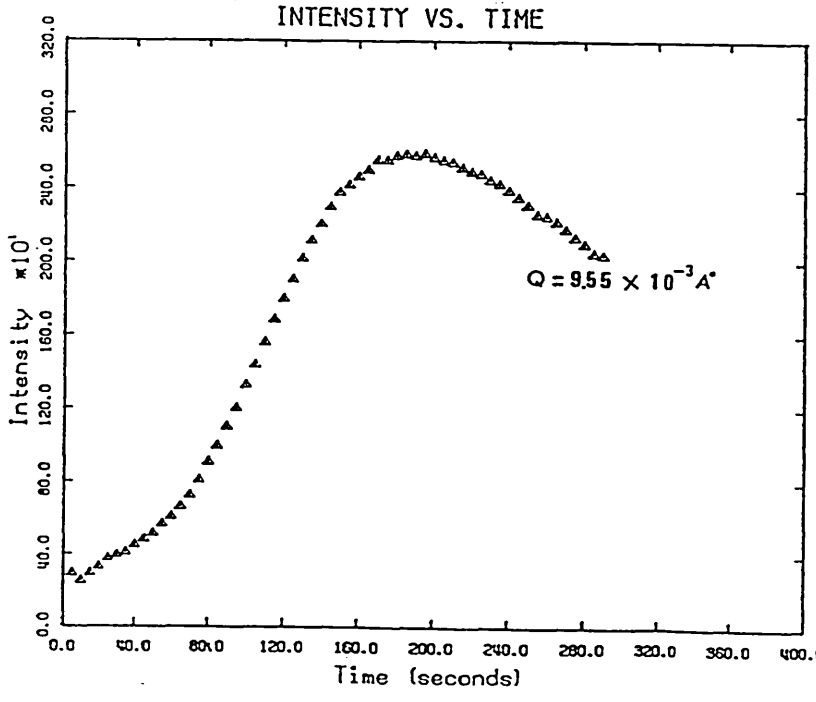


Fig.5.9 A typical plot of intensity against time for TMPC/PS–5 (50/50) at 242°C ($Q = 9.55 \times 10^{-4}$A).

region at T = 234°C. In the early stages of spinodal decomposition, intensity increases over the whole Q–range, but eventually a maximum appears as predicted by the C–H theory. The growth rate of the scattered intensity is exponential at each Q–value in the early stages, in accordance with the prediction of the C–H theory. A typical plot of intensity vs time is shown in Fig. 5.9. Corresponding to Fig. 5.9, lnI vs time is plotted in Fig. 5.10. The linearity of such a plot in the early stages is obvious and is taken as a sign that the early stages of spinodal decomposition have been observed and that the C–H theory[15,16] would be expected to apply.

In the later stages of the phase separation a decline of the scattered intensity is observed (Fig. 5.9). This is caused by the decrease of the transmitted intensity, as in this stage the sample has become very cloudy, and by the shift of the peaks towards smaller wavevectors due to a coarsening mechanism[120-122].

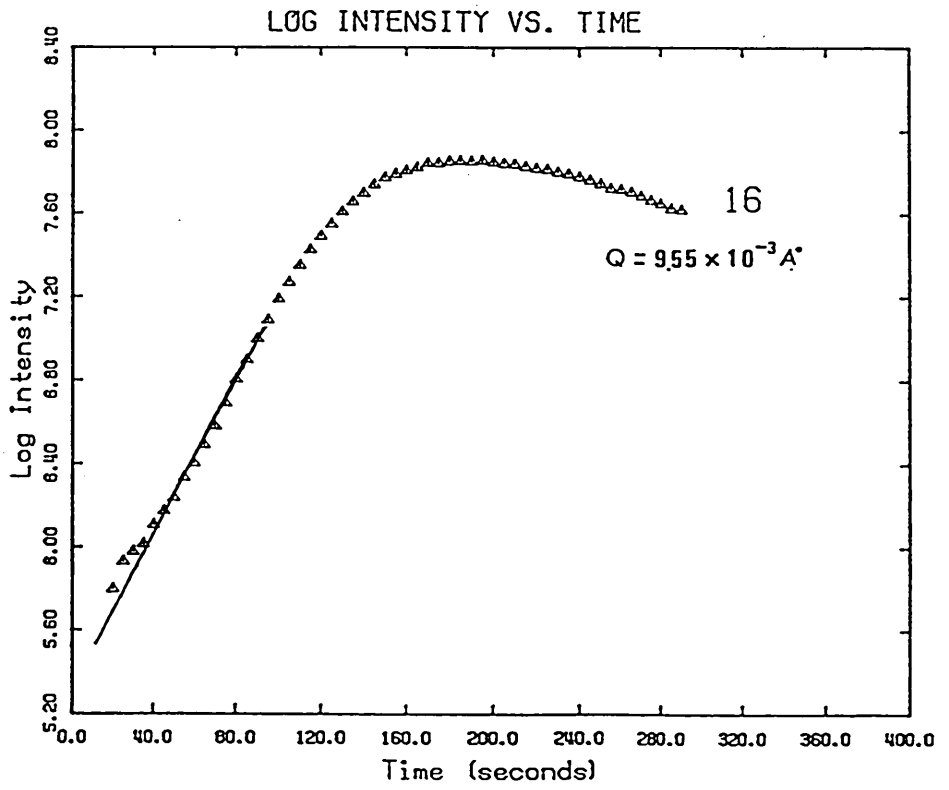


Fig.5.10 A plot of Ln (intensity) against time for the data shown in Fig. 5.9.

From the initial slope of the lnI vs time plot, values of the growth rate R(q) can be obtained (slope = 2R(q)). In Fig. 5.11, R(q) is shown as a function of Q at different temperatures. A maximum is observed at Q_m as predicted by the C–H theory. Some temperature dependence of Q_m caused by the temperature dependence of $\frac{\partial^2 G}{\partial \phi^2}$ can also be seen from this plot and in Table 5.4.

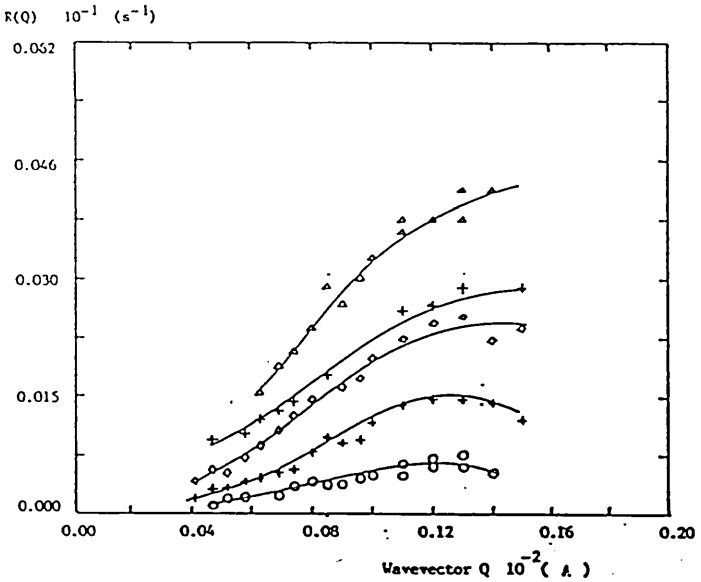


Fig.5.11 Plots of growth rate R(Q) against Q for TMPC/PS–5 (50/50) mixture at different temperatures, o ——234°C, ✦——236 C, o ——238°C, + ——240°C, Δ ——242°C.

Due to the exponential increase of concentration fluctuation in spinodal decomposition the domain size of the phase separated structure is dominated by Q_m. The domain sizes listed in Table 5.4 are obtained from the equation

$$d_0 = 2\pi/Q_m \tag{5.2}$$

In the Table the domain sizes calculated from Van Aartsen's equation[143]

$$d_0 = 2\pi l[3(\frac{T}{T_s} - 1)]^{-\frac{1}{2}} \tag{5.3}$$

are also included. Here T and T_s are the phase separation temperature and the spinodal temperature. l is the range of molecular interaction and normally equal to $R_g/\sqrt{3}$. R_g being the radius of gyration of polymer components. In this calculation the R_g of PS is used and equals 150Å.

Table 5.4 Results obtained from the C-H theory for the spinodal decompostion of a TMPC/PS-5 (50/50) blend

Temperature (°C)	Dapp (cm^2/sec) 10^{-13}	Qm[a] (cm^{-1}) 10^5	dexp[c] (cm) 10^{-5}	dtheo[d] (cm) 10^{-5}	Qm'[b] (cm^{-1}) 10^5	Qc (cm^{-1}) 10^5	Qc/Qm
234	1.52	1.25	5.02	4.80	1.71	2.42	1.94
236	3.44	1.30	4.83	2.80	1.57	2.22	1.71
238	6.62	>1.30	-	2.10	1.51	2.14	<1.65
240	8.30	>1.30	-	1.80	1.26	1.78	<1.37
242	12.10	>1.30	-	1.60	1.31	1.85	<1.42

a. From R(Q) vs Q plots
b. From $R(Q)/Q^2$ vs Q^2 plots
c. dexp = $2\pi/Qm$
d. From Van Aartsen equation

The clear disagreements between the experimental value and the predicted value of Van Aartsen are hardly surprising since the assumption of a simple temperature dependence of the interaction parameter χ_{12} used in the derivation of Van Aartsen's equation cannot describe this mixture where a strong deviation from this assumption has been observed[151].

The validity of the C–H theory is also tested via the linear dependence of $R(Q)/Q^2$ on Q^2 predicted by Equation 3.9. For all the data reported here, $R(Q)/Q^2$ does apparently vary linearly with Q^2 which again supports the use of the linear C–H theory. From the intercepts of such plots, shown in Fig. 5.12, values of the C–H diffusion coefficient D_{app} are obtained. From the slopes of the plots and the intercepts a third value of Q_m can be calculated through Q_m =

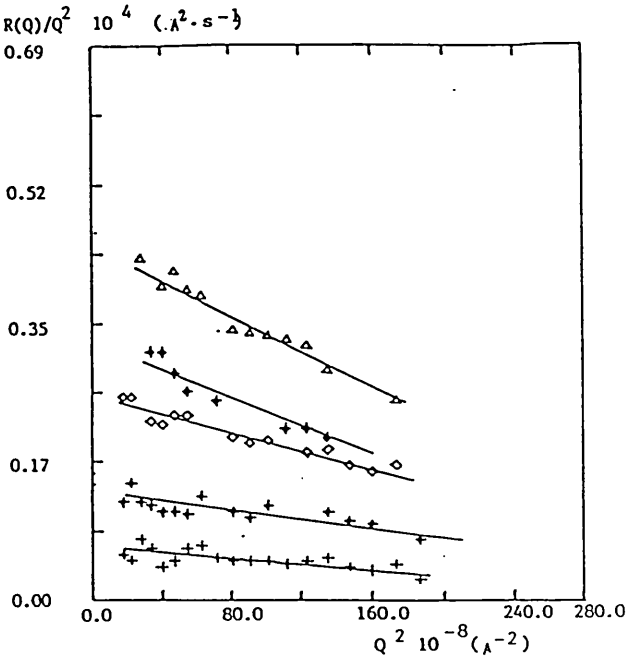


Fig.5.12 Plots of R(Q)/Q against Q for TMPC/PS–5 mixture (50/50) at different temperatures, + ——234°C, ✦——236°C, ◇——238 C, ✦——240°C, Δ——242°C.

$\frac{1}{\sqrt{2}}$ (intercept/slope)$^{\frac{1}{2}}$. The value obtained can give an internal consistency check on the use of C–H theory. The Q_m obtained is listed in Table 5.4. It is obvious from the table that although the values of Q_m agree well with each other in the order of magnitude, the values obtained form $R(Q)/Q^2$ vs Q^2 plots show a weak reverse temperature dependence.

In Figure 5.12, the change of slopes described as 2MK at different temperatures is also noticed. Such change may have been caused by the change of M with temperature.

The D_{app} values obtained (in the order of 10^{-15}) are fairly small compared with those obtained for other systems[96,100,105]. However, this may not be very surprising if we carefully consider the delicate combination of the mobility term M and the thermodynamic term $\frac{\partial^2 G}{\partial \phi^2}$ in D_{app} expressed as

$$D_{app} = -M\frac{\partial^2 G}{\partial \phi^2} \qquad (5.4)$$

From C–H theory, we know the thermodynamic driving force $\frac{\partial^2 G}{\partial \phi^2}$ can be obtained from the following equation, providing K is known

$$-\frac{\partial^2 G}{\partial \phi^2} = 4KQ_m^2 \tag{5.5}$$

K being the gradient coefficient which is related to the radii of gyration (R_g's) of components in the mixture[156] through

$$K = \frac{M_A}{6}\left[\frac{(R_g^2/M_w)_A}{\phi_A} + \frac{(R_g^2/M_w)_B}{\phi_B}.\frac{M_B}{M_A}\right] \tag{5.6}$$

Here M_A, M_B are the monomer mass of components, being 104 and 298 respectively for PS and TMPC. $\left[\frac{R_g^2}{M_w}\right]^{\frac{1}{2}}$ for PS has been obtained by many authors, here a value of 0.275Å[105] is taken for the calculation. Such values for TMPC are not available in the literature, thus $\left[\frac{R_g^2}{M_w}\right]^{\frac{1}{2}}$ for bisphenol–A polycarbonate is used, which is 0.359[30]. The densities of PS and TMPC, being 1.05 g/cm^3 and 1.09 g/cm^3 respectively are used in the calculation of the volume fraction. Substituting all the values into the equation we have K = 15.62Å^2. Applying K in equation 5 the $\frac{\partial^2 G}{\partial \phi^2}$ at T = 235^{0}C is estimated to be

$$-\frac{\partial^2 G}{\partial \phi^2} = 9.76 \times 10^{-5}$$

M, being the mobility constant, should be of the same order as D_T, the transport coefficient which can be described by either the "fast theory"[157] or the "slow theory"[158]. In the case of the "fast theory" we have

$$D_T = D_{PS}^{*}.\phi_{PS}.N_{PS} \tag{5.7}$$

Here D_{PS}^*, being the tracer diffusion coefficient, is in the order of 10^{-13} at 234^0C[159] and N_{PS}, the degree of polymerisation, is in the order of 10^3. Thus D_T should be in the order of $10^{-10} \sim 10^{-11}$, and D_{app} will be in the order of $10^{-15} \sim 10^{-16}$, as observed in the experiments.

As indicated in the earlier chapters, $\frac{\partial^2 G}{\partial \phi^2}$ is equal to zero at the spinodal, so is D_{app}. From this the spinodal temperature of the mixture could be determined. Such a plot is shown in Fig. 5.13. Here a good linearity is found and the extrapolated value of T_s (= 233°C) is obtained. The obtained spinodal temperature agrees with the cloud point determined (Fig. 5. 3) within experimental errors.

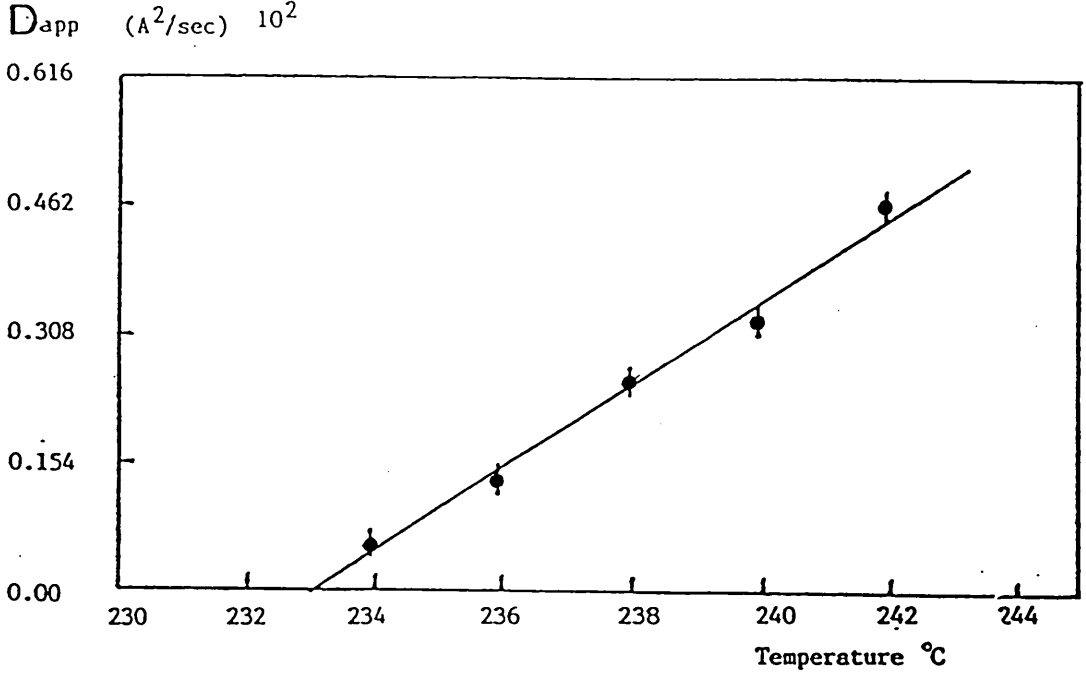


Fig.5.13 The apparent diffusion coefficients D_{app} plotted as a function of temperature for TMPC/PS–5 (50/50) mixture.

The C–H theory also predicted a cut off wavevector Q_c where R(Q) reduces to zero. Since this value is difficult to obtain experimentally we have calculated Q_c from the $R(Q)/Q^2$ against Q^2 plot at $R(Q)/Q^2 = 0$. The values obtained are listed in Table 5.4. Clearly the ratio of Q_c/Q_m is larger than the

predicted value of 1.414. Similar observations were also made in other mixtures[105,108].

In explaining this disagreement Park *et al*[160] have pointed out the $\frac{Q_c}{Q_m} = \sqrt{2}$ is only valid when thermal fluctuations are included in the C–H theory at T = 0°K. By taking account of thermal fluctuations considered by Cook[115]. Park derived an expression:

$$\frac{Q_c}{Q_m} = \left[\frac{2T_s}{T_s - T}\right]^{\frac{1}{2}} \tag{5.8}$$

Here T equals 273K. By substituting the value of T_s into the equation, a value of 2.08 is obtained for Q_c/Q_m, comparing with the experimental values which range from 1.93 to less than 1.37. The agreement is obviously far from satisfactory. Moreover, the observed temperature dependence of Q_c/Q_m cannot be described by this equation.

In the treatment of spinodal decomposition in polymer mixtures Binder[116] derived some rather different equations for Q_c and Q_m, from which the ratio of Q_c/Q_m is expressed as

$$\frac{Q_c}{Q_m} = \sqrt{2} \quad \text{for } \frac{\chi}{\chi_s} - 1 \ll 1 \tag{5.9}$$

$$\frac{Q_c}{Q_m} = \frac{\left[\frac{2\chi}{\chi_s} - 1\right]^{\frac{1}{2}}}{\left[\frac{2\chi}{\chi_s}\right]^{1/4}} \quad \text{for } \frac{\chi}{\chi_s} >> 1 \tag{5.10}$$

The above two equation may be able to describe the temperature dependence of Q_c/Q_m through χ/χ_s, however the calculated value of Q_c/Q_m from these equations is not in agreement under any circumstances with the

present experimental value. The two conditions of $\frac{\chi}{\chi_s} - 1 >> 1$ and $\frac{\chi}{\chi_s} >> 1$ for the above two equations can be interpreted as corresponding to "shallow quenches" and "deep quenches" respectively. If we believe that the crossover of shallow quench and deep quench is smooth rather than clear–cut, it is difficult to see how the above two equations will match. When we actually solve the two equations above, two unrealistic values of $\frac{\chi}{\chi_s}$, $\frac{\chi}{\chi_s} = 2.91$ and $\frac{\chi}{\chi_s} = 0.086$ were obtained.

In summarising the above discussion, one can see that the data reported here are in quite good agreement with the first two of the predictions described in Chapter 3, but while $R(Q)/Q^2$ does apparently vary linearly with Q^2, values of Q_m obtained from these plots neither agree with those observed directly in $R(Q)$ nor show the correct temperature dependence. Nor, moreover, is $Q_c = \sqrt{2}\, Q_m$. Such discrepancies with the simple C–H theory are also found in other measurements. Reasons for such failure of the simple C–H theory are various. Several major factors will be discussed below.

5.1.3 Possible reasons for the disagreements observed

On the experimental side, the rate of temperature jump is one of the major concerns. Carmesin *et al*[125] explored the effect of a non–instantaneous temperature jump via computer simulations and found dramatic deviations from the C–H behaviour which included non–linear $R(Q)/Q^2$ against Q^2. Experimentally we also noticed a similar effect when the pre–heating temperature was lowered about 40^0C, hence giving a long jump time. The linear plots observed here may indicate that it is not the rate of temperature quenching which is causing the problem.

In recent experiments, Han *et al*[102] have applied a new technique of data analysis in spinodal decomposition by taking account the thermal fluctuation and the refraction of samples in the experiments. Due to the equipment limitation, such analysis cannot be utilised in this treatment. However, from the comparison of the new technique and the normal method (lnI vs t) conducted by the author, one finds that a rather flat plot of $R(Q)/Q^2$ against Q^2 is obtained from the new technique. This could mean that an even greater Q_c will results, while Q_m may change little. Thus it seems that this new data analysis method would give even bigger Q_c/Q_m.

Thermodynamically the peculiar behaviour of the interaction between TMPC and PS observed by Brereton *et al*[151] also causes concern since both Q_c and Q_m are closely associated with $\frac{\partial^2 G}{\partial \phi^2}$. By using Brereton's results we have calculated $\frac{\partial^2 G}{\partial \phi^2}$ at different temperatures, shown in Fig. 5.14 as well as K values shown in Fig. 5.15. These were obtained from the slopes and the intercepts of S(Q) against Q^2 using

$$\frac{1}{S(Q)} = 2(\chi - \chi_s) + l^2Q^2 = \frac{\partial^2 G}{\partial \phi^2} + 2KQ^2 \qquad (5.11)$$

Clearly the $\frac{\partial^2 G}{\partial \phi^2}$ vs temperature plot is not linear, contrary to previous observations for other mixtures[105,108]. Thus it is not possible to extrapolate $\frac{\partial^2 G}{\partial \phi^2}$ from the one phase region to the two phase region although such values would be of great value in interpreting the observed disagreements. However, looking at the development of $\frac{\partial^2 G}{\partial \phi^2}$ and K in Figs. 5.14 and 5.15, it is very likely that both K and $\frac{\partial^2 G}{\partial \phi^2}$ will further decrease and $\frac{\partial^2 G}{\partial \phi^2}$ will eventually become negative as the temperature increases. Since Q_m is proportional to the absolute value of $\frac{\partial^2 G}{\partial \phi^2}$ and inversely to K (Equation 3.12), a decrease of Q_m with increasing temperature, as seen in column 4 of Table 5.4, is not expected. Thus

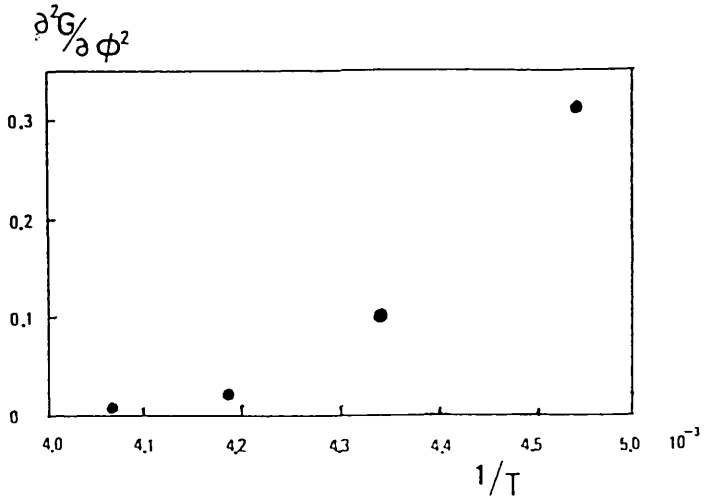


Fig.5.14 Plot of intercepts $\left[\frac{\partial^2 G}{\partial \phi^2}\right]$ against 1/T obtained from Brereton's results.

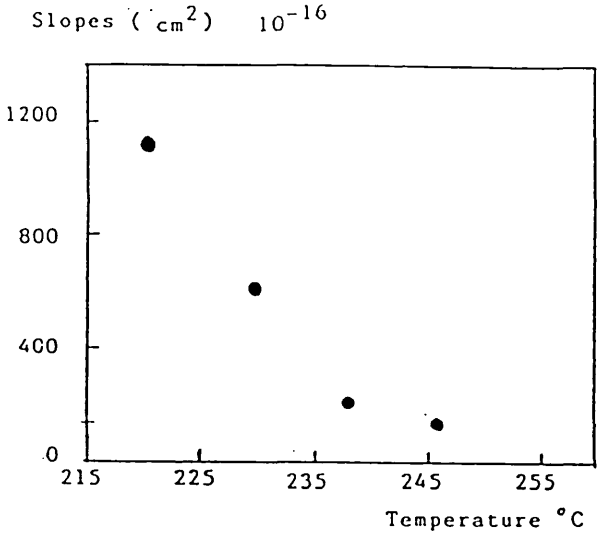


Fig.5.15 Plot of slopes (= 2K) against temperature obtained from Brereton's results.

the peculiar interaction behaviour in this system is not to blame for the reversed temperature dependence of Q_m observed in Table 5.4.

Besides the factors discussed above, Binder[117] has recently shown numerically that the slow relaxing variables of polymer mixtures undergoing phase separation near a glass transition may also affect the phase separation process. Such slow relaxing variables are mainly associated with T_g's of the components. However, we do not consider this to be a major concern since our

experiments were performed at about 50°C above the T_g of TMPC, at least until other possible reasons are ruled out.

The neglect of the non–linear term in the C–H theory and the effect of thermal fluctuation have been dealt with recently by Higgins *et al* [105]. Here it was shown that discrepancies such as observed here with simple C–H theory could be explained by the inclusion of thermal fluctuations in the equations, despite the fact that the temperature quench used here is much bigger than 0.48°C, below which, as indicated by Han, thermal fluctuations are effective for PS/PVME systems. However, one has to bear in mind that such a limit may be system dependent.

From the above discussion it may be concluded that the disagreements between the simple C–H theory and the experimental results are most probably caused by the neglect of the thermal fluctuation force in the analysis.

5.2 PES/PEO system

5.2.1 Miscibility study

A. Film clarity

Films with PEO concentration less than 50% are clear at room temperature, while they are cloudy when PEO concentration in the mixture is larger than 50%. This is due to the crystallisation of PEO in the mixture with higher PEO component. The existence of crystals in the film at room temperature is confirmed by the observation of crystal structures under an optical microscope and by the fact that films become clear when the temperature of the film is over 65°C where crystals have melted. The observation here supports the earlier conclusion that PES/PEO is a miscible

system in the amorphous state. Due to moisture absorption of PEO, films may become cloudy after being stored in the atmosphere for a long time.

B. The glass transition temperature

Fig. 5.16 shows the measured glass transition temperatures of PES/PEO blends. Due to crystallisation of PEO the glass transition temperatures of mixtures with PEO concentration larger than 50% by weight were not obtained. For all the mixtures examined here an intermediate glass transition temperature is noted. While the width of the transition is not very different from the pure PES, which may indicate intimate mixing between PES and PEO. The solid line drawn using the Fox equation[37] is also shown in Fig 5.16. The glass transition temperature of PEO has not been universally agreed. Here a value of -75^0C is used in the calculation[154]. The positive deviation of experimental results from the prediction may suggest the existence of specific interactions between the two components. Such interaction has been proposed to be between the –o– group in PEO and the benzene ring in PES. However, studies of infrared spectroscopy for this mixture conducted in this study have failed to confirm this speculation.

C. Phase boundary of the mixture

The cloud point curve of the mixture obtained using the newly designed light scattering equipment is depicted in Fig. 5.17. A minimum point is found in the mixture with 90% PEO, as seen in Singh's[154] experiments. Disagreements between this observation and Singh's experiments are noticed in high PES concentration range. Contrary to Singh's observation, cloud points higher than the glass transition temperature of the mixture are found. This disagreement may have been caused by the use of different techniques. The use of a hot stage in the measurement of cloud points by Singh may have introduced larger errors in the measurements.

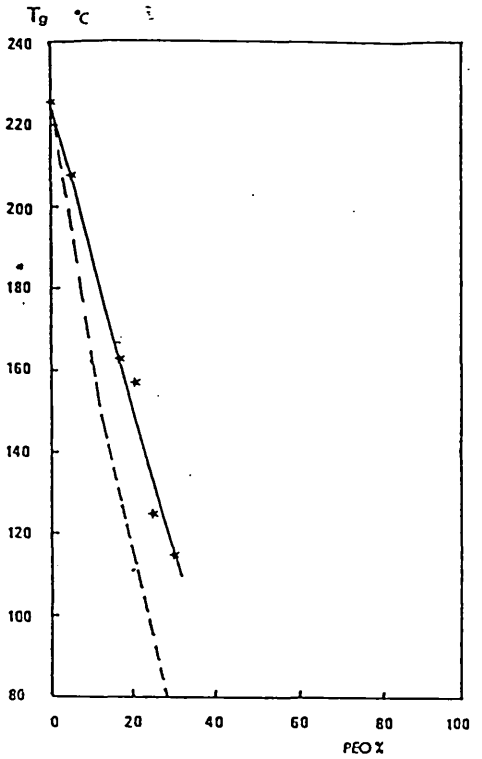


Fig.5.16 Plots of glass transition temperatures of PES/PEO mixtures. The dotted curve is plotted according to Fox equation.

★——— experimental results.

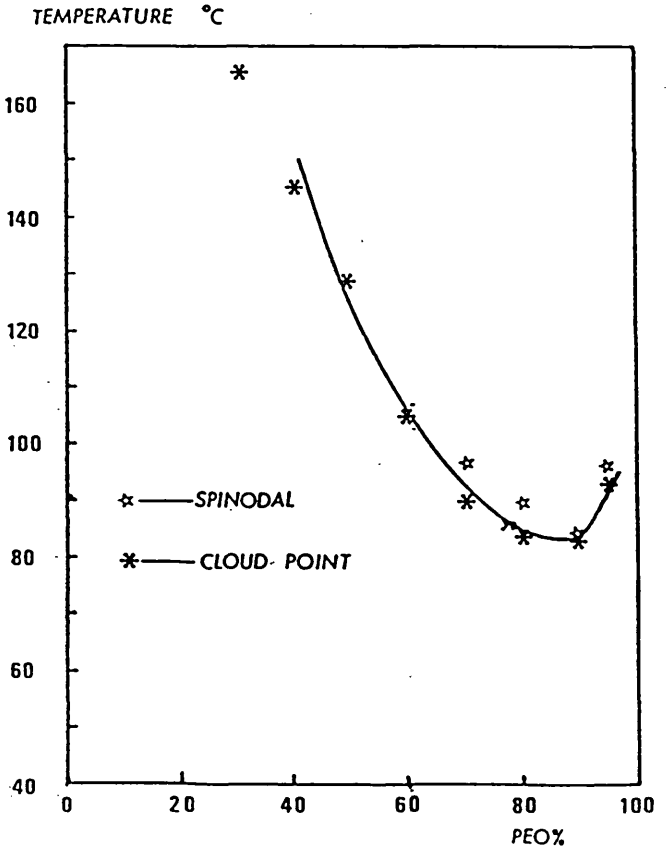


Fig.5.17 The phase boundary of PES/PEO blend.

Also plotted in the figure are the spinodal temperatures measured by observing the development of scattered intensity with time at successive temperatures. One typical plot of this kind is shown in Fig. 5.18. This method is utilised based on the following principle. In the metastable region phase separation should occur according to the nucleation and growth mechanism, while in the unstable region it should occur according to the spinodal decomposition mechanism. The difference of phase separation mechanisms gives rise to the difference in the scattered intensity change with time, as shown in Fig. 5.8. Exponential increase of scattered intensity in the unstable region in contrast with the non–exponential increase in the metastable region is noticed. The temperature where the transition from non–exponential to exponential increase is taken as the spinodal temperature.

The T_g's, cloud points and the spinodal temperatures for this blend are listed in Table 5.5.

5.2.2 Crystallisation and melting behaviour of the mixture

A. Equilibrium melting temperatures

In the study of crystalline polymers one of the major difficulties is the determination of the equilibrium melting temperature T_{me}. Three techniques may be used in obtaining T_{me}. These are:

1. Extrapolation of small molecules of similar chemical structures to polymers
2. Extrapolation of small crystal melting points
3. Melting temperature as a function of crystalline and annealing temperature

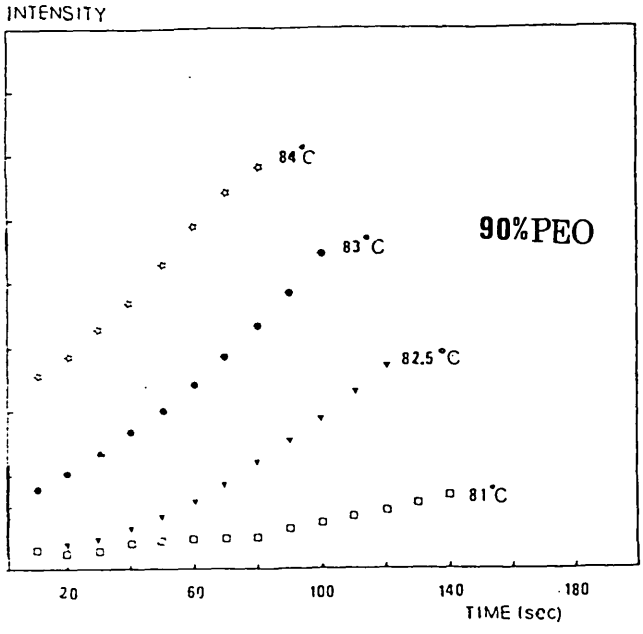


Fig.5.18 Typical plots of intensity against time in the vicinity of spinodal temperature.

Table 5.5 Glass transition temperatures, cloud points and spinodal temperatures for the PES/PEO blends

Concentration PEO %	Cloud points (°C)	Spinodal Temperature (°C)	Tg (°C) Exp.	Fox's
0	-	-	226	226
5	-	-	208	191
20	-	-	157	110
25	-	-	125	89
30	165	-	115	70
40	145	-	93	37
50	127	-	-	11
60	105	-	-	-12
70	90	96	-	-31
80	84	89	-	-48
90	82	83	-	-62
95	93	97	-	-69

Each of the above techniques is unique in its approach and is applicable in different cases. However, when crystallisation of one component in a miscible polymer blend is dealt with the first two methods cannot be utilised because the thermodynamic behaviour of the mixture will be dramatically changed with changing molecular weights and hence the melting behaviour. The last technique is the most popular method available to detect T_{me} of the crystalline components in a mixture.

From the theory of polymer crystallisation one expects a linear relation between the melting point, T_m, and the crystallisation temperature, T_c, corresponding to the equation[161]

$$T_m = T_{me}\left[1 - \frac{1}{n}\right] + \frac{T_c}{n} \qquad (5.12)$$

where $n = l/l^*$ is the ratio of the lamellar thickness l to the thickness l^* of the critical nucleus at T_c. Measurements of T_m and T_c of the mixture conducted in DSC have produced curved lines (Fig. 5.19) in contradiction to the prediction of

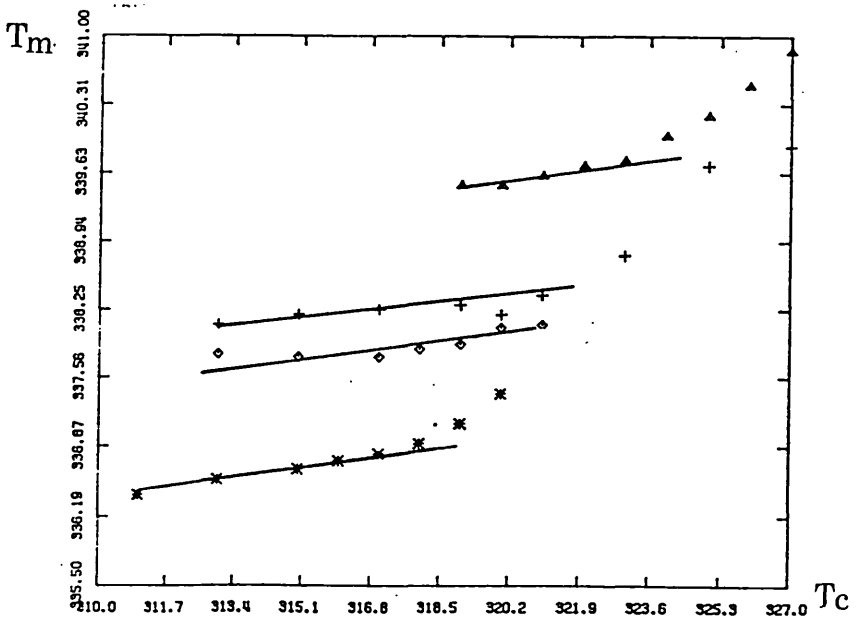


Fig.5.19 The measured melting temperatures as a function of crystalization temperature.

△——PEO,+——95%PEO,◇——90%PEO,✱——80%PEO.

the above equation. At higher T_c deviation from linearity is quite obvious and the T_m's of the mixtures tend to approach the T_{me} of PEO. The deviation may result from the unrealistic assumption of the crystal being perfect and of finite size at T_c in the derivation of the above equation. Similar observations were also made in the PMMA/PEO system[162].

In order to obtain the equilibrium melting point, T_{me}, the linear region at lower T_c is extrapolated to the curve of $T_c = T_m$, where T_{me} can be obtained in accordance with Equation 5.12. The determined T_{me} of the mixture is shown in Fig. 5.20 and Table 5.6. As seen the equilibrium melting temperature is depressed from 67.7°C in pure PEO to 65°C in the mixture with 20% PES. The agreement between values of T_{me} observed here (67.7°C) and other experiments (68°C ± 0.5°C[163]) may support such extrapolation in the linear region.

The depression of T_{me} in mixtures may be due to the morphological effects – the thickness of the crystal is regarded as the major parameter. Runt[164] has formulated an equation which describes the equilibrium melting depression caused by the thickness of the crystal.

$$\Delta T_m = \Delta T_m^0 + \left\{ \frac{T_{MB}^0}{T_{MB}^0 + T_c + \frac{\Delta H_f^0 \delta_B}{2\sigma_e}} - \frac{T_{MB}^0}{T_{MB}^0 + T_c + \frac{\Delta H_f^0 \delta_B}{2\sigma_e}} \right\} \tag{5.13}$$

where δ_B and δ_A are parameters defining the thickness of the crystal in blends and in pure form respectively, and are considered to be independent of blend composition. T_{MB}^0 and T_{MA}^0 are the equilibrium melting temperatures of polymer blends and the crystalline component. σ_e is the folding surface free energy. ΔT_m^0 is considered as the thermodynamic melting depression. The

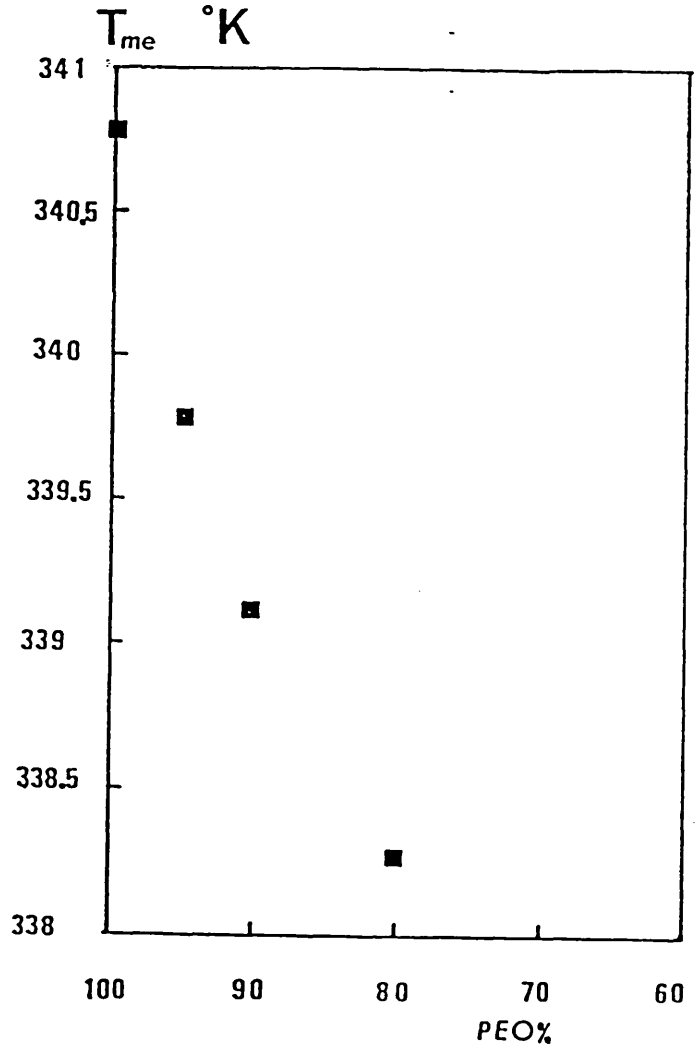


Fig.5.20 A plot of equilibrium melting temperatures against concentration of the PES/PEO (10/90) mixture.

Table 5.6 Equilibrium melting temperatues of the PES/PEO mixtures

PEO Concentration	Tm(°K)	ΔTm(°K)*
Pure PEO	340.82	0
95% PEO	339.83	0.99
90% PEO	339.12	1.70
80% PEO	338.25	2.57

* $\Delta T_m = T_{m(PEO)} - T_m$

calculation[164] has shown that the experimentally observed ΔT_m is considerably less than the thermodynamic melting point depression, ΔT_m^0, on the condition that lamellar thickening at T_c is negligible (n = 1). However when lamellar thickening at T_c is considered such differences between the measured ΔT_m and ΔT_m^0 will decrease with increasing n. The results here have shown that n is in the range of 10 ~ 40 and changes with composition of the mixture. Thus the measured ΔT_m can be considered mainly due to the thermodynamic effects, from which calculation of χ_{12} can be made in next section.

B. Melting point depression

The melting point depression observed in polymer blends is linked to the interaction parameter, χ_{12}, through Equation 2.70 in Chapter 2. Simple mathematical manipulation results in

$$\Delta T_m = - T_{me}^0 \left[\frac{V_{2u}}{\Delta H_{2u}}\right] B\phi_1^2 \qquad (5.14)$$

$$B = RT\chi_{12}/V_{1u} \qquad (5.15)$$

The plot of ΔT_m against ϕ_1^2 is depicted in Fig. 5.21. Linear regression of the plot and the use of V_{1u} = 169 cm^3 mol^{-1}, V_{2u} = 38.9 cm^3 mol^{-1} and ΔH_{2u} = 1980 cal mol^{-1} and densities of ρ_{PES} = 1.379 g/cm^3 and ρ_{PEO} = 1.065 g/cm^3, give a χ_{12} of $-$ 2.33 ± 0.50.

The non–zero intercept in Fig. 5.21 may suggest that the entropic effect occurring during mixing may not be negligible. A value of χ_{12} too large in comparison with the literature data on miscible blends[98,108] may suggest that the Flory–Huggins theory is not adequate to describe the melting behaviour of polymer blends and the technique used to measure T_{me}^0 may not be good enough. Because of the neglect of concentration effects on χ_{12} and the lack of

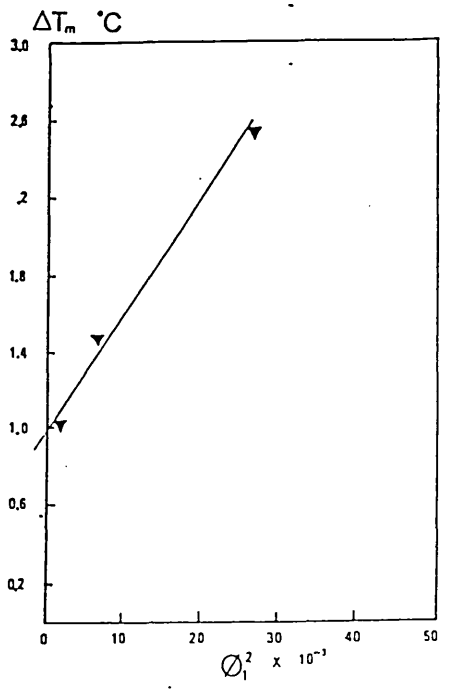


Fig.5.21 Plot of ΔT_m against ϕ_1^2.

full understanding of the morphological change of crystals at different T_c and concentration, the absolute value of χ_{12} has to be taken with caution. Nonetheless, the negative χ_{12} measured from such a simple technique has supported the early observations of PES/PEO miscibility. The discrepancy between this result and Singh's ($\chi_{12} = -0.23$) may be caused by the use of crystallisation temperature depression in Singh's treatement.

C: **Overall rates of crystallisation**

In the earlier discussion we have observed the concentration effects on T_{me}. The addition of PES in PEO can also be noted in its effects on crystallisation rate. Fig. 5.22 shows the melting endothermal area of PEO as a function of concentration of the mixture at the same T_c. Clearly on increasing the amount of PES in the samples the overall crystallisation rate becomes progressively slower. The effect of this can be explained by both the reduction in chain mobility and the changes in composition during crystallisation. When a polymer chain crystallises in the presence of a non–crystallisable component,

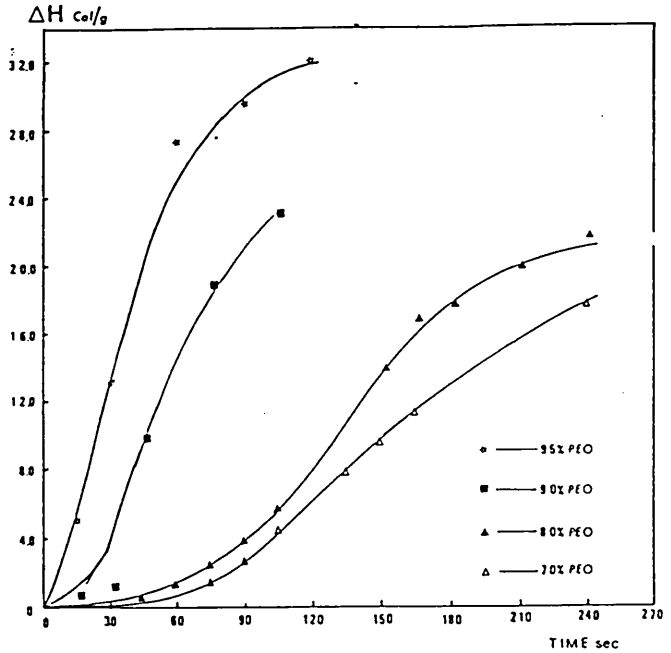


Fig.5.22 Effects of PES on the crystallization behavior of PEO in the mixture.

can be expected that the increasing accumulation of the non–crystallisable component outside the crystalline region will result in a systematic reduction of nucleation rate and the melting point. The addition of PES in PEO increases the glass transition temperature of the system and hence reduces the mobility PEO. The reduction of the chain mobility of PEO will result in a decreasing growth of crystals.

The kinetics of the isothermal crystallisation from the melt of PES/PEO blends have been analysed according to the Avrami equation[165]

$$\chi_t = 1 - \exp(-K_n t^n) \qquad (5.16)$$

where K_n is the overall kinetic rate constant and n is a parameter characterising the type of nucleation and the geometry of growing crystals. X_t is the crystallinity. From the above equation a straight line between $\log[-\ln(1 - X_t)]$ and log t with an intercept of log K_n and slope of n would be expected. One

example of such plots is shown in Fig. 5.23. The observed linear trends indicate that for all the temperature investigated the crystallisation kinetics of these blends follow the Avrami equation until a high degree of conversion where the secondary crystallisation may happen. The mean value of the Avrami index n of each blend changes with T_c and concentration of the mixture. The obtained n for pure PEO is in the range of 1.9 ~ 0.5, as has been measured by other investigators. This value corresponds to a three–dimensional growth of crystalline units according to a crystallisation process developed by heterogeneous nucleation. The increase of n with increasing T_c may indicate the change of crystal morphologies with T_c. While the absence of any correlation between n and mixture concentration may suggest that the type of nucleation and geometry of growing crystals is independent of the concentration of the mixture.

All the results obtained are compiled in Table 5.7.

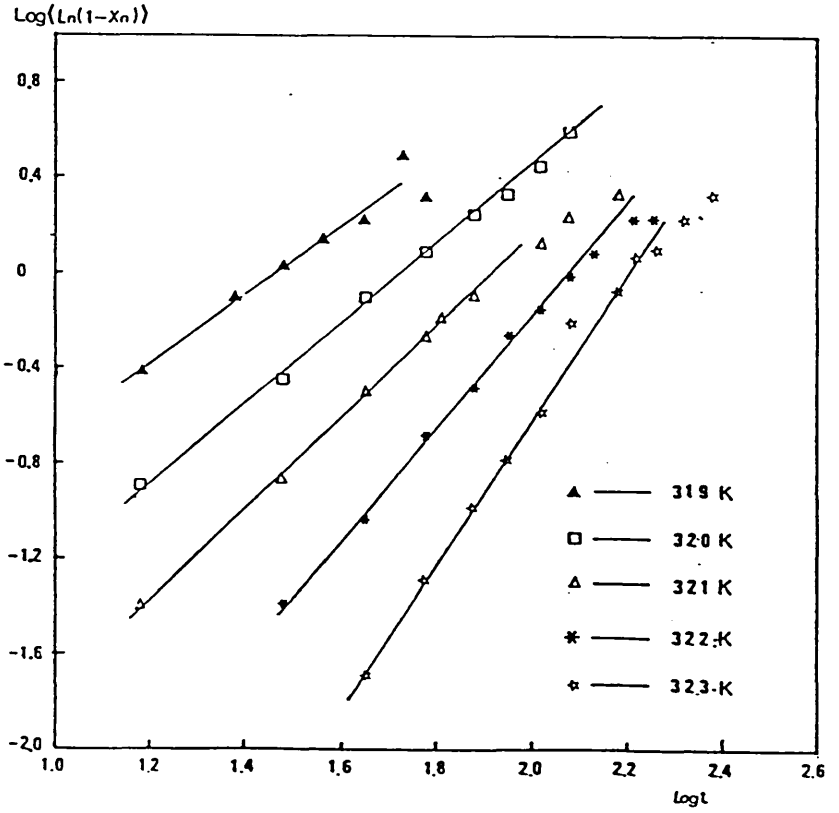


Fig.5.23 One typical plot of log[ln{–(1–Xn)}] against logt for the 70/30 PEO/PES mixture at different T_c.

Table 5.7 Data of overall crystallization study of PES/PEO mixtures

Mixtures	Tc (^{0}K)	Tm' (^{0}K)	Kn	n
PEO	319	339.5	-	-
	320	339.5	-	-
	321	339.6	-	-
	322	339.7	-	-
	323	339.75	-	-
	324	340.0	1.29×10^{-3}	1.87
	325	340.2	5.02×10^{-5}	2.22
	326	340.5	1.07×10^{-6}	2.43
	327	340.85	1.74×10^{-11}	4.36
PEO/PES (95/5)	315	338.2	-	-
	317	338.25	-	-
	319	338.3	-	-
	321	338.4	-	-
	322	338.6	8.91×10^{-4}	1.95
	323	338.8	5.62×10^{-5}	2.28
	324	339.3	8.32×10^{-6}	2.38
	325	339.7	8.51×10^{-7}	2.86
	326	339.8	3.24×10^{-7}	2.25
PEO/PES (90/10)	315	337.9	-	-
	317	337.85	-	-
	318	337.95	-	-
	319	338.0	-	-
	320	338.2	-	-
	321	338.0	-	-
	322	338.3	5.13×10^{-3}	1.46
	323	338.5	1.23×10^{-4}	2.07
	324	338.8	4.17×10^{-6}	2.40
	325	339.0	5.13×10^{-7}	2.65
PEO/PES (80/20)	313	336.55	-	-
	315	336.65	-	-
	316	336.73	-	-
	317	336.8	-	-
	318	336.9	-	-
	319	337.1	10^{-2}	1.34
	320	337.4	3.63×10^{-3}	1.35
	321	-	2.40×10^{-4}	1.88
	322	-	1.41×10^{-5}	2.34
	323	-	2.34×10^{-7}	3.00
PEO/PES (70/30)	309	335.7	-	-
	311	336.05	-	-
	313	336.25	-	-
	315	336.45	-	-
	317	336.85	-	-
	319	337.15	3.02×10^{-3}	1.60
	320	337.65	5.89×10^{-4}	1.80
	321	338.0	9.12×10^{-5}	2.11
	323	338.45	3.89×10^{-7}	2.85

5.2.3. Kinetics of phase separation

Preliminary experiments have shown that phase separation of PES/PEO in the Q range is accessible by light scattering techniques. So, phase separation in this blend was followed using the laboratory built light scattering instruments described in Chapter 3 and carried out as outlined in the experimental section. Within the phase boundary, plots of scattered intensity change exponentially with time in the initial stage (Fig. 5.24) and the corresponding ln(intensity) vs time plot is linear (Fig. 5.25), as expected from the C–H theory. A maximum in the I(q) vs q plot also appears to be time independent in the region where linear lnI vs time is found, and moves to smaller q as phase separation goes on. The movement of Q_m to smaller Q is caused by involvements of ripening and coalescence mechanisms[120-122] in the later stages of the phase separation.

Growth rates, R(Q), obtained from slopes of ln(Intensity) vs time at different temperatures as a function of Q are plotted in Fig. 5.26. A broad peak is observed in the plot and moves to high Q as temperature increases. The increase of Q_m with increasing temperature is caused by increase of $\frac{\partial^2 G}{\partial \phi^2}$ as the phase separation temperature moves away from the spinodal temperature. The Q_m's obtained in these plots are also tabulated in Table 5.8. The initial correlation length obtained from $\frac{2\pi}{Q_m}$ is found to be in disagreement with Van Aartsen's prediction[143] if a value of l in the order of the radius of gyration of components is used. Such a disagreement may be attributed to the F–H interaction parameter, χ_{12}, which is assumed to be composition independent when used in the derivation of Van Aartsen's equation[143].

Unlike the TMPC/PS system, $R(Q)/Q^2$ against Q^2 shows a marked deviation from linearity, especially in the low Q range (Fig. 5.27), as found for

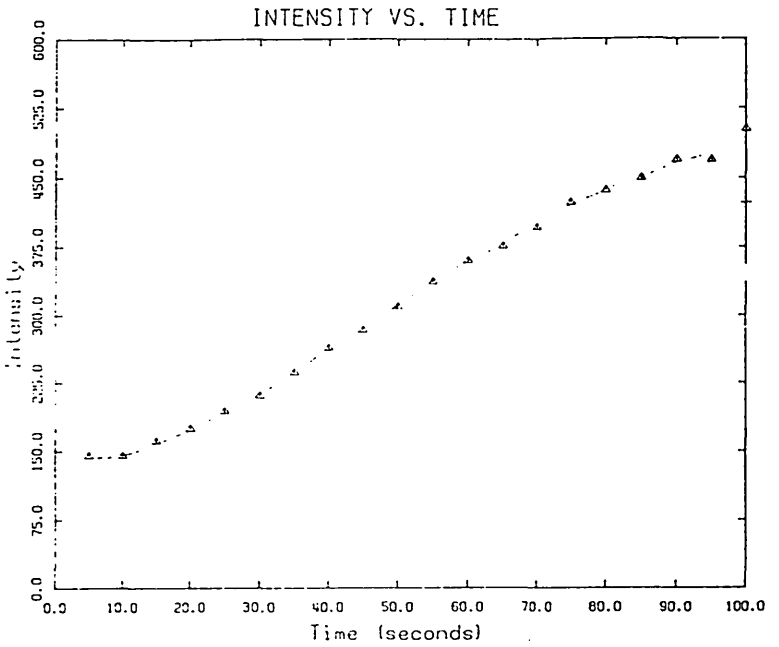


Fig.5.24 A typical plot of scattered intensity against time for PES/PEO(10/90) mixture during phase separation.

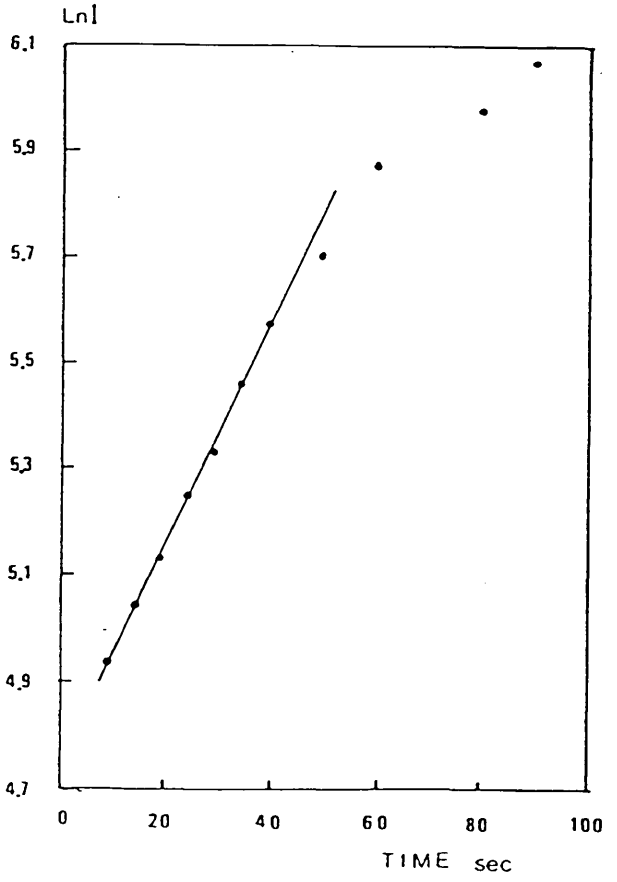


Fig.5.25 A plot of ln(intensity) v. time for the plot shown in Fig. 5.24

Table 5.8 Data of kinetics of phase separation of PES/PEO(10/90) mixture

Temperature (°C)	Dapp (cm^2/sec) 10^{-13}	Q_m[a] (cm^{-1}) 10^5	Q_m'[b] (cm) 10^5	d_{exp}[c] (cm) 10^{-5}	d_{theo}[d] (cm) 10^{-5}	Qc/Qm
86.5	9.27	1.14	1.0	1.34	1.34	1.61
87.7	16.0	1.23	1.2	5.23	0.98	1.45
88.5	19.3	1.21	>1.4	<4.49	0.88	<1.22
89.7	24.0	1.24	>1.4	<4.49	0.76	<1.22

a. From $R(Q)/Q^2$ vs Q^2 plats
b. From R(Q) vs Q plots
c. $d_{exp} = 2\pi/Q_m$
d. From Van Aartsen equation

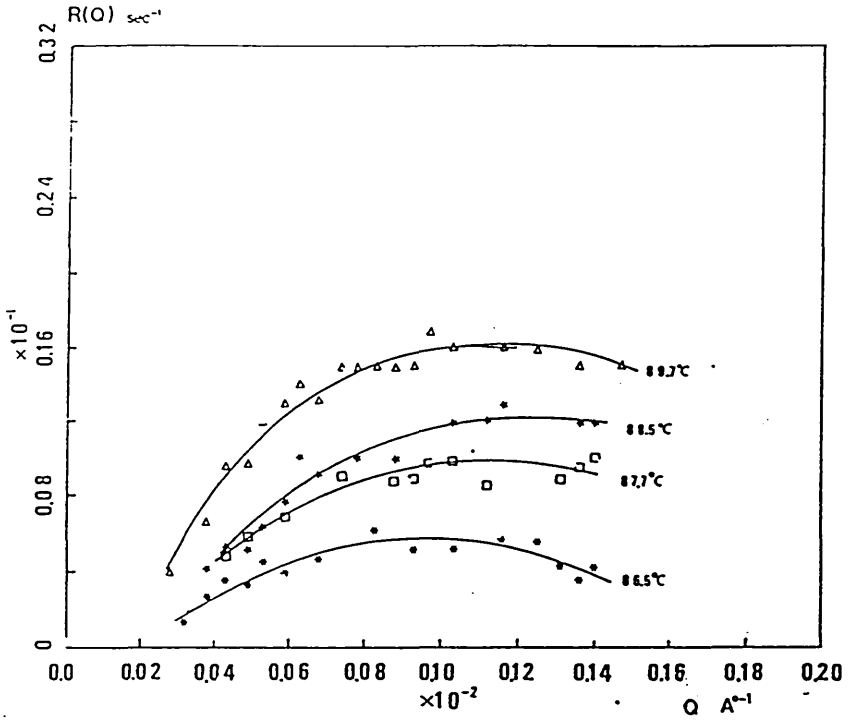


Fig.5.26 Plots of growth rate R(Q) against Q for the PES/PEO (10/90) mixture at different temperatures.

other systems. The curvature of $R(Q)/Q^2$ against Q^2 plots may be attributed to:

1. The omission of the non–linear terms in the simple C–H theory, as considered by Lange[145].
2. The wave–vector dependent diffusional coefficient M, discussed by Pincus[119] and Binder[116].

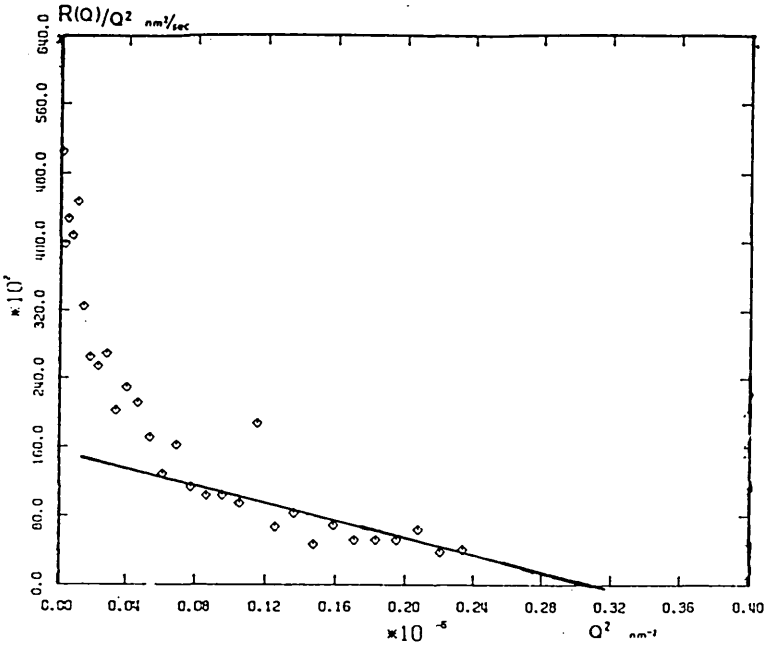


Fig.5.27 A typical plot of $R(Q)/Q^2$ against Q^2 at temperature 87.7°C.

3. The effects of slow relaxing variables associated with glass transition temperatures of the components. These effects have been discussed by Binder[117].

4. The non–instantaneous temperature jump as discussed by Carmesin[125].

5. The thermal fluctuation force[115] occurring in the phase separation process.

The first two reasons are very unlikely since the data presented here meet the requirements of $2R(Q_m).t > 1$ and $R_g^2Q^2 >> 1$, set respectively for the two reasons. The third reason is considered less important, at least until other reasons are ruled out.

Carmesin[125], via computer simulation, has demonstrated that the non–instantaneous temperature quench will result in a non–linear $R(q)/Q^2$ vs Q^2 plot. Because long wavelength fluctuations are amplified first during the continuous quench, the resulting peak would be broadened. The broad peak observed in the R(Q) vs Q plot may indicate the existence of such effects.

The effects of the thermal fluctuation force has been vigourously pursued both experimentally and theoretically. Han[94] has claimed that such effects have

been observed in the spinodal decomposition of PS/PVME mixtures when the quench depth ΔT is less than 0.4°C. Higgins *et al* [105,108] have stated that the disagreement between the simple C–H theory and the experimental results for PMMAM–SAN and TMPC/PS may be a result of the involvement of thermal fluctuations. Although the quench depth , ranging from 1°C ~ 8°C, used in this study is much greater than 0.48°C in the case of the PS/PVME system, thermal fluctuations may still be present in this case, since a limit on quench depth below which the effects of thermal fluctuations occur may be a system dependent parameter.

The apparent mutual diffusional coefficient, D_{app}, is calculated from the intercept of the straight line drawn in the high Q range of $R(Q)/Q^2$ against Q^2 plots and the calculated D_{app}'s at different temperatures are presented in Table 5.8. The value of D_{app}, in the order of $10^{-12} \sim 10^{-13}$ cm^2/sec, is comparable with PS/PVME mixtures. Considereing that the phase separation temperatures are far below the glass transition temperatures of PES and far above the T_g of PEO, it would be most probable that the phase separation in this mixture is mainly controlled by the fast moving component, PEO.

If the mobility of polymers does not change significantly with temperature and the phase separation is brought about by the entropy term, the plot of D_{app} should be linear and extrapolate to the spinodal at $D_{app} = 0$. The plot of D_{app} against temperature is shown in Fig. 5.28. Least squares fit gives a T_s value of 85°C which agrees well with the spinodal temperature obtained from static experiments described in Section 5.2.2.

Providing K, the energy gradient term in the C–H theory, is known, the knowledge of Q_m has enabled us to calculate $\frac{\partial^2 G}{\partial \phi^2}$, using the thermodynamic driving force of spinodal decomposition. By using equation 5.6 ,K is calculated

to be 34.7Å^2, with the use of $\left[\frac{R_g^2}{M_w}\right]^{\frac{1}{2}}_{PEO} = 0.310$[30] and $\left[\frac{R_g^2}{M_w}\right]^{\frac{1}{2}}_{PES} = 0.265$. Here the value of $\left[\frac{R_g^2}{M_w}\right]^{\frac{1}{2}}_{PES}$ for PES is taken to be the one for poly[sulfonly–(phenyl ethylene)][30]. According to Equation 5.5, $\frac{\partial^2 G}{\partial \phi^2}$ equal to -2.14×10^{-4} is obtained at temperature 89.7°C.

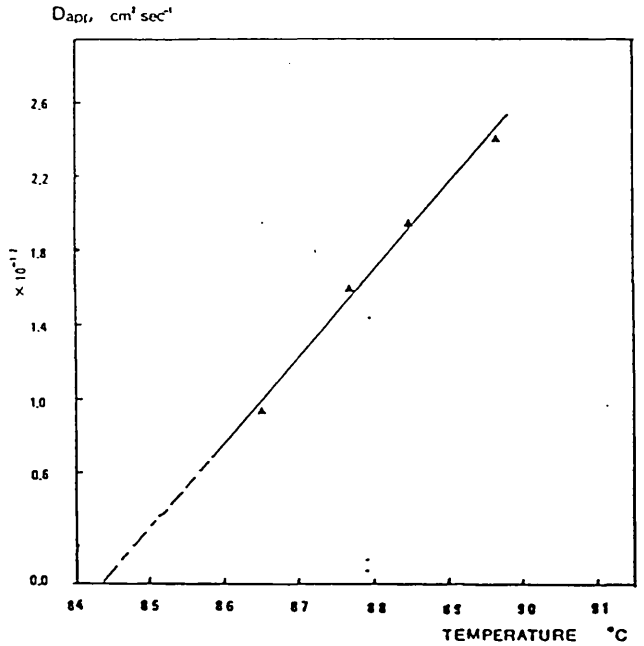


Fig.5.28 The apparent diffusion coefficient D_{app} plotted against temperature of phase separation.

By applying the equation of state theory, $\frac{\partial^2 G}{\partial \phi^2}$ is calculated to be -48.7 at T = 90°C, according to Equation 2.44. Parameters used for the calculation are listed in Table 5.9 and taken from references[154].

The observed difference in values of $\frac{\partial^2 G}{\partial \phi^2}$ calculated from two different methods is too great to be possibly compensated by probable errors of K and Q_m in the determination. Thus the use of the equation of state should be carefully considered. The possible reasons could be:

1. The parameters used in the calculation are not representative of the real system at high temperatures. Values of thermal expansion coefficient, thermal pressure coefficient at high temperature are calculated from

Table 5.9 Parameters used for the calculation of $\frac{\partial^2 G}{\partial \phi^2}$ from the equation of state

Components	Thermal expansion coefficients $10^{-4}K$	Thermal pressure coefficients $(Jcm^{-3}K^{-1})$	Density g/cm^3
PES	2.00	1.40	1.37
PEO	5.50	1.20	1.065
X12 = -40 J/cm^3	Q12 = -0.048	S2/S1 = 1.2	

values at room temperature. Such calculation may introduce large errors in the value.

2. X_{12} obtained from heat of mixing measurement of oligomeric materials may differ from the real value for the polymer blends.

3. The equation of state may be inadequate to quantitatively describe the thermodynamic behaviour of polymer blends.

Chapter 6

OPTICAL QUICK–RELEASE PRESSURE CELL

6.1 Introduction

To perform the experimental study of kinetics of phase separation of polymer blends via a pressure jump, a special pressure cell is required. In this chapter the design requirements for the cell are laid down. The choice of the cell and manufactured cell are described and characterised.

6.2 Design requirements

6.2.1 Window materials

In the design of optical pressure cells, the window is considered to be the most important part. The material used must fulfill the following two basic requirements. Firstly, it must have a good transmission in the electro–magnetic region of the radiation of interest, secondly it must be able to withstand the highest pressure required in the experiments.

Higher pressure normally requires smaller window area, while a smaller window area may worsen the signal to noise ratio in the study. Thus these two requirements generally have to be compromised in most cases.

There are many window materials available for different purposes. In Table 6.1 the characteristics of some of the window materials are presented[167].

As discussed before, the study of kinetics of phase separation of polymer blends is usually accomplished by scattering techniques. Among the techniques

Table 6.1 Characteristics of window materials used in various optical pressure cells.

Material	Spectral range (μm)	Refractive index at λ (μm)	Modulus of runpture (psi)	Young's modulus (psi)	Compressive strength (psi)	Hardness Knoop number	Solubility (g per 100 g H_2O)
Sodium chloride (NaCl)	0.2-15	1.52 at 4 1.4 at 10		5.8×10^6		15.2-18.2	35.7 (0°C)
Lithium fluoride (LiF)	0.11-6	1.35 at 4 1.1 at 10		9.40×10^6		102-113	0.27 (18°)
Irtran 1 (MgF_2)	1-8	1.35 at 4	21,800	16.6×10^6	157,600	576	0.0076 (18°C)
Calcium fluiride (CaF_2)	0.13-9	1.41 at 4		$11-15 \times 10^6$		158	0.0016 (18°C)
Irtan 3 (CaF_2)	1-10	1.41 at 4 1.34 at 8.3	5,300	14.3×10^6		200	Insoluble
Irtran 2 (ZnS)	2-14	2.25 at 4 2.20 at 10	14,100	14×10^6	121,200	354	0.00069 (18°C
Irtran 4 (ZnSe)	0.5-20	2.5 at 4 2.4 at 10	6,100	10.3×10^6		150	Insoluble
Magnesium oxide (MgO)	< 6.8	1.7 at 2.2 1.66 at 4.3		3.6×10^6		690-692	0.000012
Irtran 5 (MgO)	1-8	1.67 at 4 1.60 at 6	19,200	48.2×10^6		640	0.00062
Sapphire (Al_2O_3)	< 5.5	1.73 at 2.2		50.56×10^6		1,370 1,525-2,000	9.8×10^{-5}

Table 6.1 (continued)

Material	Spectral range (μm)	Refractive index at λ (μm)	Modulus of runpture (psi)	Young's modulus (psi)	Compressive strength (psi)	Hardness Knoop number	Solubility (g per 100 g H_2O)
Diamond type I	2-4, 5.7 10-16	2.4173				7,000	Insoluble
Diamond type II	0.26-4; 5.5 through FIR						
Ceramic barium titanate ($BaTiO_3$)	< 6.9	2.4 at 2.2, 4.3		16.50×10^6			
Calcite ($CaCO_3$)	0.2-5.5	$\simeq$ 1.7					
Germanium	1.8-2.3	$\simeq$ 4.0					
Silicon	1-9	3.43 3.42					
Fused silica SiO_2 (Corning 7905, GE type 101-100, Infrasil)	0.3-3.5	1.43					
NBS F158 SiO_2	4.5	1.80					
Calcium aluminate ($CaO-Al_2O_3$) and similar materials							
RIR-2	4.5	1.75					
RIR-10, 11, 12	5.0	1.62					
RIR-20	5.5	1.82					

available light scattering is the most commonly used technique, however, for some of the polymer blends[108,105] phase separation proceeds at a smaller scale that is not accessible by light scattering, or not enough refractive index contrast exists in the system. X–ray scattering might have to be used. Therefore the window used in this optical pressure cell must have a good transmission to both visible light (6823 Å) and X–rays.

Preliminary experiments showed[90,93] that for most polymer blends the critical temperatures increases with pressure at a rate of about 20^{0}C/kbar. By considering the phase separation temperatures for most of the miscible polymer blends (normally less than 200^{0}C) and the degradation temperatures of most polymers (about 300^{0}C) a pressure range of 0–5 kbar is required for the pressure cell. So the window used and the structure of the cell must be strong enough to withstand this pressure.

6.2.2 Quick pressure–release mechanism

The proposed pressure jump requires a quick pressure–release mechanism accommodated in the pressure cell. Also the jump must be quicker than temperature jumps which have been used in kinetic experiments. Temperature jumps[94,96,98,107] used in the past typically range from a few seconds to a few minutes. Thus, the pressure jump should be accomplished in less than a second.

In order to comply with safety regulations in the X–ray experiments the jump must be able to be remotely controlled.

6.2.3 Heating system

For kinetic experiments a stable control of sample temperature is essential. Since phase separation temperatures of most polymer blends of interest occurs below 200^{0}C a maximum temperature of 250^{0}C is proposed for the design of a heater for the pressure cell. A temperature ramp is required to control the temperature. It should be able to maintain the temperature constant within an error of ±0.2^{0}C and to increase (or decrease) the temperature at required rates which range from 0.2^{0}C/min to 2^{0}C/min.

Since the heating system is an integrated part of the pressure cell consideration should be given to the accommodation of the heater in the cell and ways of placing thermocouples near the sample, in order to measure the temperature of the sample under study.

6.2.4 Exit of scattered light

In the laboratory–built light scattering equipment (described in Chapter 4), the photodiode array spans over an angle range of 60^0. Therefore an exit for the scattered light in the pressure cell should have an angle of 120^0.

In summary, the requirements for the pressure cell are:

1. A pressure range from 1 bar to 5 kbar and pressure control within an error of ±100 bar.
2. The window should have good transmission for both light and X–rays and withstand 5 kbar pressure.
3. A quick pressure–release mechanism must be accommodated in the cell and enable the pressure jump to be accomplished in less than a second. the pressure jump must be remotely operated in the X–ray experiments.

4. A maximum temperature of 250°C in the heater is required. The temperature must be easily measured and steadily controlled within an error of 0.2°C.

5. Small size and compact design are highly desirable due to limited space available in X–ray and light scattering apparatus. An exit of the scattered beam in the cell should have an angle of 120 degrees.

6.3 Pressure cells and the choice

Many different optical pressure cells have been constructed and used in different experiments. Despite the variations involved in each individual case they can be classified into six basic designs.

1. Fluid media cells into which pressure is piped from an external generator.
2. Liquid media cells in which the pressure is generated *in situ.*
3. Solid media cells of a piston–in–cylinder type.
4. Solid media cells of a multiple–anvil type.
5. Sliding anvil cells.
6. The diamond–anvil cell.

There are advantages and disadvantages for each of these cells. The detailed discussion can be found in references[166,167]. In brief, the main disadvantages of the first five categories are their bulkiness and the use of pressure transmitting media, which may interfere with the polymer mixtures. Thus the Diamond–Anvil Dell (DAC) was chosen for the quick pressure–release optical cell.

The DAC was first discovered by workers[168] at the National Bureau of Standards in 1959 and has been extensively used in materials research under

pressure. In the polymer field, X–ray diffraction of poly(ethylene) and PTFE crystals under pressure was studied by using DAC[169,170]. A good reference to studies of materials using DAC can be found in several reviews and books[167,168].

The advantages of DAC are its compact size, high pressure and good transmission for both light and X–ray. According to the requirements the quick pressure–release DAC cell was designed and constructed by Dr David Adams at the University of Leicester.

6.4 Description of the cell

The optical diamond–anvil cell (DAC), shown in Fig. 6.1, consists of two diamond anvils which are glued to the two polished stainless steel plates. The alignment of the two diamonds is achieved by translation and rotation of the lower diamond. Three equally spaced set screws are used for the translational adjustment and the other three are used for the rotational

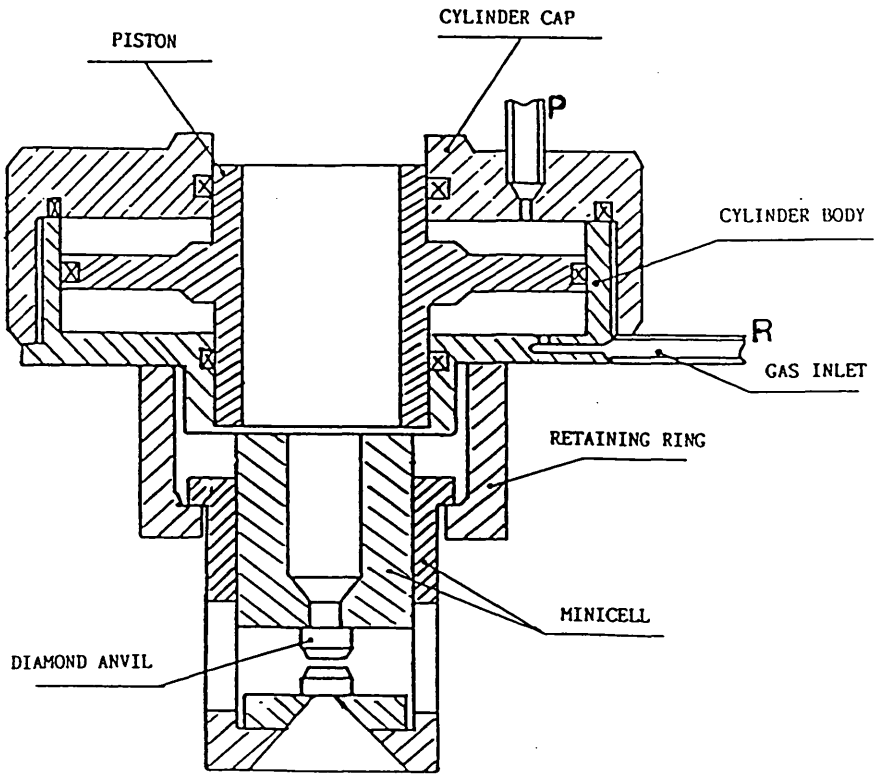


Fig.6.1 A schematic drawing of the diamond anvil cell.

adjustment. Two diamonds are forced into contact (or away from contact) with each other by the gas driven piston. The gas chamber with two gas inlet tubes is connected through a five–part valve to a nitrogen gas cylinder. The flow directions of gas is schematically shown in Fig. 6.2. By operating the handle of the valve, the gas can either go through the R tube or the P tube. When it flows in the P tube, the piston forces the bottom diamond up into contact with the top one and pressure is produced between the two diamond anvils. In order to gently apply pressure on the anvils a restrictor is assembled in the supply line. Switching the toggle on the valve to the opposite position, gas will go through the R tube and the piston is forced to move downward with a quick release of pressure. This process can normally be operated in a fraction of a second. A cone–shaped hole is machined in the bottom plates for the incident light. An exit hole with an angle of 120^0 is provided for the scattered light on the top plate. Type I diamonds with a 0.9 mm facial diameter and a 1.73 mm height are used. Between the two plates a 3 mm thick ring–heater is placed in order to heat the sample up to the required temperature. The manufacture of the ring–heater will be described later in this chapter.

Two side slots are machined in the cell to lead out the wiring for the heater. They can also be used to load samples into the cell if the heater is not used.

A precision pressure gauge is assembled between the cylinder and the valve. This gauge has a range of $0 - 100$ psi, with an accuracy of 0.25%. Nylon tubing (O.D. 1/4 in, I.D. 0.17 in) is used for the gas supply line which is long enough to allow operations of the valve outside the X–ray beam room.

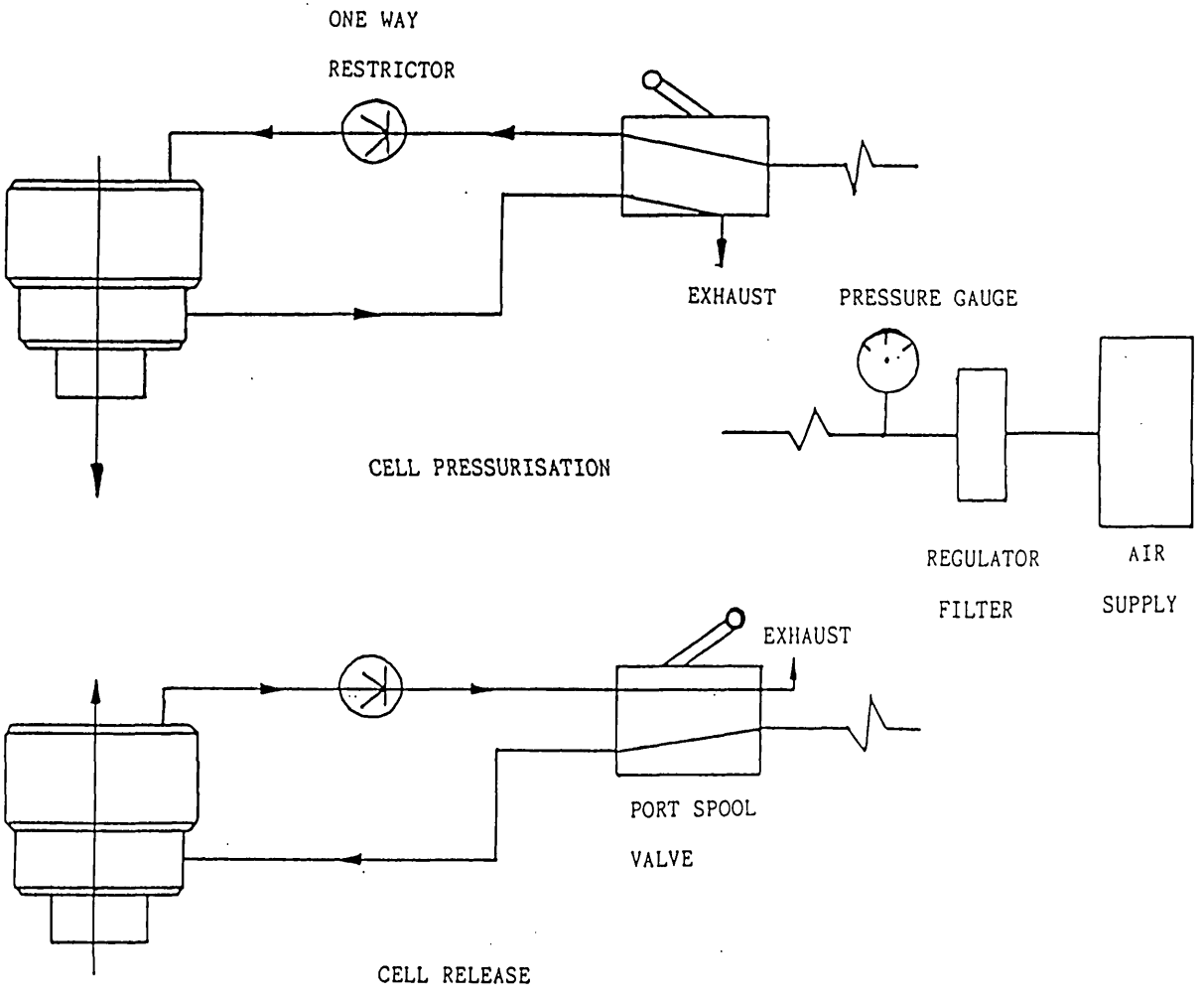


Fig.6.2 The gas flow charter in the operation of DAC.

6.5 Some problems

Despite constant requests to accommodate all the requirements for the design of the cell into the manufacture of the cell, several problems, some serious, were found in the use of the cell as provided.

1. The heater provided for the cell was too thick to be mounted between the anvil–mounting plates. Thus pressure could not be applied on the anvils. This problem was eventually solved by thinning the heater with abrasive papers.
2. The heater was finally placed between the plates and pressure applied. The maximum temperatures obtained by placing a thermocouples near the sample through the gap left in the exit of the cell was about 75^{0}C, in contrast to the manufacturer's claim of a maximum temperature of 250^{0}C. In discussion with the manufacturer it was confirmed that the claimed maximum temperature of 250^{0}C was taken in a more favourable condition than in the cell. Larger heating mass and poor insulation in the cell probably contributed to the above discrepancy. Poor design of the heater also contributed to the earlier breakage of the lead wire of the heater. Thus a modified heater was made.
3. In the design of the cell no consideration was made of the secure mounting of the heater in the pressure cell. In experiments the heater practically has to rest loosely on one of the anvil–mounting plates. Since modification of this part of the cell would lead to a total reconstruction of the cell and need an unacceptably long time, such modification was not attempted. A temporary heater mounting method was used in later experiments.

4. No account was taken of the fixing of the thermocouple for the temperature measurements of the sample. The earlier attempt of placing the thermocouple through the gap in the exit of the cell was hardly adequate in the light scattering experiments since the existence of the thermocouple wire in the exit would introduce unwanted parasitic scattering and this method was also difficult to exercise. This problem was eventually solved in the new heater built in this laboratory.

6.6 Design of the heater

The design of a heater depends on many factors, such as the configuration of the heater and the characteristics of the heating elements. Many of the factors involved in the design cannot be easily accounted for by simple calculations and many have to be compromised. Limited space available in the pressure cell has prevented us from using large amounts of resistance wires in the heater and the low–surface loading resistance wire. The restricted availability of fibre glass insulated resistance wires provided us no chance of trying different wires for the heater. All such difficulties have hindered efforts at making a heater to achieve a maximum sample temperature of 250^{0}C. The heater with a maximum sample temperature of 150^{0}C described in the following section, although it is not ideal, has enabled us to conduct some preliminary experiments.

The heater is schematically shown in Fig. 6.3. Stainless steel is used to make the ring with an O.D. of 14 mm and an I.D. of 10 mm. The thickness of the heater is 3 mm, comparing with the 3.17 mm gap left between the two diamond–anvil mounting plates. Magnin resistance wires (diameter = 0.2 mm) with fibre glass sleeve (O.D. = 0.5 mm) are wound around the ring. The wound

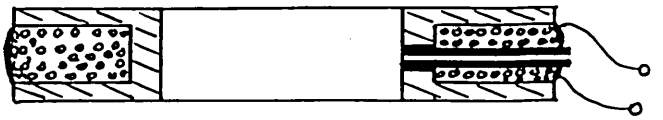


Fig.6.3 A schematic drawing of the ring heater.

wires were finally sealed by Autostick. A 0.7 mm hole is drilled in the lateral side of the heater. A fine aluminium tube (O.D. – 0.7 mm, I.D. = 0.4 mm) was fitted into the hole and thermocouples can be pushed through the tube in order to measure the temperature near the sample. The total measured resistance of the heater is 7.8 Ω and the total length of the wound wire is about 60 cm. The characteristics of the heater made are discussed in Section 6.8.

6.7 Pressure calibration of the DAC

6.7.1 Introduction

The application of diamond anvil cell (DAC) in the scientific investigation makes the accurate pressure determination necessary. The earlier work performed in DAC was done on solids pressed between the diamond anvils without using a gasket. These experimental conditions were firstly demonstrated to be non–hydrostatic by Van Valkenburg[171]. The pressure gradient existing under these conditions was claimed to be parabolic in nature, with pressures in the centre reaching 1.50 times those on the edge. Thus any pressure measured under these conditions was basically an average value.

The problem of the pressure gradient presence in the DAC was solved[172] by using a gasket between the diamond anvils and immersing the solids of interests in a fluid. This technique virtually achieved a hydrostatic condition for the solid to certain pressures. However some debate exist as to whether

simply using a gasket between the diamond anvils and the fluid provides sufficient hydrostatic conditions. It is probably true that the use of a gasket will reduce the pressure gradient more than if no gasket is used.

Over the years of DAC application several methods of pressure calibration of DAC have been developed, but accurate measurements of pressure in DAC continue to be a major problem in this field.

6.7.2 Methods of pressure calibration

Various methods of pressure calibration involving DAC have been based on the determination of pressure from:

1. an applied load,
2. frequency dependence of certain vibrations in various materials,
3. phase transitions at known pressures,
4. shifts of optical absorptions with pressure, and
5. lattice constant dependence on pressure of NaCl and other crystals as determined by means of X–ray.

In the following sections each of the methods above will be discussed.

A. Pressure calibrated from applied load

This method was used at the beginning of the DAC application. The force applied on the DAC was obtained by a force gauge and the contact area was determined from photomicrograph of the anvils. The pressure calculated from the relationship :

$$P = F/A$$

F being the force and A the area.

This method, though simple, lacks accuracy in measurements. And moreover when a gasket is used it is impossible to determine the pressure because the exact contact area and the load absorbed by the gasket are unknown.

B. Pressure dependence of certain vibrations in various materials.

This technique is incorporating various materials in a liquid in a gasketed DAC. The pressure dependence of certain absorption bands were followed versus liquids with known freezing pressures. Then a relationship between the wavelength of the vibration and pressure can be established.

Different materials have been applied in this method by various scientists[173,174] ,however none of the materials tested is being generally accepted by all users. This technique also requires complex equipment and chemicals used for the calibration may interfere with the materials under investigation.

C. The ruby scale

The ruby scale was developed by workers[175] at the National Bureau of Standards and has been generally accepted to be the most reliable method for pressure calibration of DAC. In this technique pressure dependence of the sharp ruby fluoresence lines are followed with pressure. The fluoresence is induced by an Ar^+ or Cd–He laser. Due to the spin transition $^2E \leftarrow {}^4A_2$ Cr^{3+} in a cubic field would show a single band. However in ruby the Cr^{3+} occupies an Al^{3+} site, but being of different size, it assumes a lower symmetry. Splitting of the ^2E level is caused by the removal of degeneracy due to spin–orbit coupling. This splitting results in the excitation of two fluoresence lines having a difference of 1.4nm (R1 692.8nm, R2 694.2nm).

Since its discovery this technique has improved steadily with the application of new technology and the pressure range covered by this technique has extended to 2.3Mbar[176,177]. The obtained quantitative relation between the shift of wavelength of the ruby fluoresence and pressure is presented as :

$$P\ (\text{Mbar}) = 3.808\left[\left[\frac{\Delta\lambda}{6942} + 1\right]^{5} - 1\right] \qquad (6.1)$$

where $\Delta\lambda$ is the shift of wavelength of the fluoresence in Å. The advantages of this technique are its rapidity and dependability due to high intensity per unit volume of ruby, sharp linewidth and acceptable pressure dependence. Thus it is regarded as the best scale available in this field. However it also has several disadvantages, such as larger temperature coefficient and thermal brodening. It, therefore, cannot be used for precision measurements at temperatures above 200°C. Since the shift below 10kbar is very small, extemely sensitive instruments are required to measure this shift.

D. Pressure calibration from phase transition

Under certain pressure a substance may change from one phase to another phase. The phase transition results in a difference in the indices of refraction, birefringence, light absoption and other properties, which can be observed by means of different techniques, especially microscopy. The transition pressure determined can be used in the pressure calibration of the DAC.

Many substances have been utilised and several DACs have been calibrated by this method[178-180]. Although this method is not as popular as it used to be it still serves as a good alternative to the ruby scale at low pressures.

E. **Pressure calibration from lattice constant of crystals with pressure by using X–rays.**

In this technique the lattice structure of certain crystals is measured by X–ray diffraction at different pressures in the DAC, from which the pressure is calculated from the equation of state of the crystal. The most commonly used crystal is NaCl.

The merits of using NaCl in the calibration is that a vast amount of data is easily available. However since the compressibility of NaCl is very small and the change of interplanar spacings is therefore minimal, this method is not very accurate at low pressures. It has been reported[169] that the use of NaCl as a pressure standard will introduce an error of at least 44% at 3kbar in pressure calibration. Due to this, other crystals, such as hexamethylene tetramine (HMT), have been developed[169].

6.7.3 Pressure calibration for the present DAC

Each technique discussed above is unique in its own approach and can be applied in particular cases. Often instrumental restraints have to be compromised with the ultimate accuracy of the measurements. In this study three methods of pressure calibration were attempted. In the beginning of the experiments gaskets made of steel, aluminum and bronze were used; however none of the materials was found to have a desirable durability in the required pressure range. Thus the calibration followed afterwards was conducted without using gaskets. Such a calibration may not be very ideal, but it may be more suitable to the real experimental conditions since the scattering experiments on the phase separation of polymer blends can not be implemented in the presence of a gasket which will produce unwanted parastitic scattering.

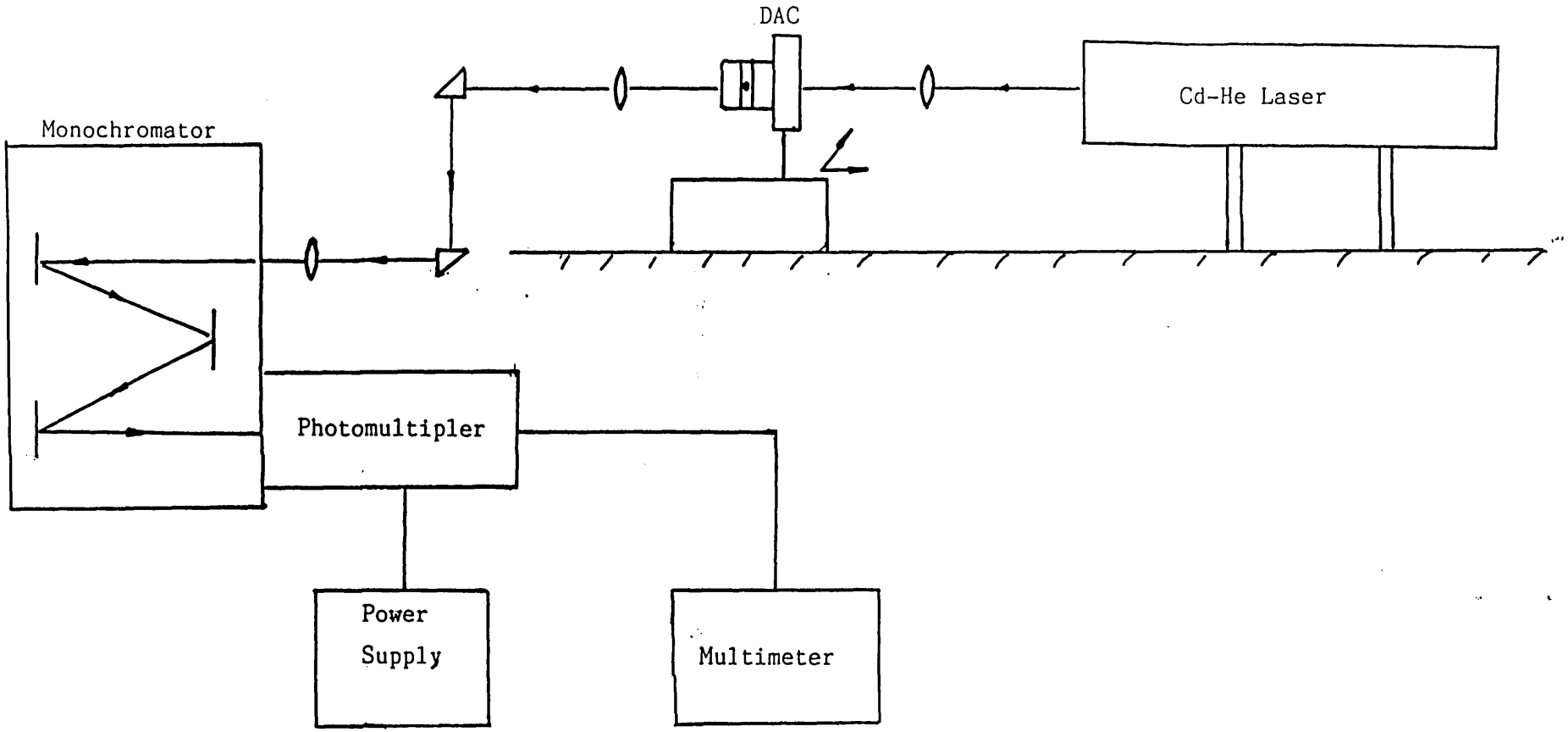


Fig.6.4 A schematic diagram of the set–up used for the pressure calibration of DAC by the ruby scale.

In the following section pressure calibration procedures of three methods are described.

A. The ruby scale

This measurement was conducted in the set–up schematically shown in Figure 6.4. Briefly the blue laser (λ = 4679 Å) beam is focused on the DAC where a piece of ruby chip is placed. The emmission from the ruby chip is then focused on a prism and lead into the monochromator by a lens in order to maximise the intensity of the emmision. The incoming beam is split inside the monochromator and lead out through a pinhole. A photomultiplier is positioned near the pinhole and the intensity of the radiation at different wavelengths is measured by the output current from the photomultipler. The wavelength of the monochromator is calibrated using a He/Ne laser with a wavelength of 6328 Å. The spectra of Cd/He laser showed that besides the main radiation at 4679 Å peaks were also found in the region of 6600 Å to 7100 Å. Because the ruby fluoresence occurs in this region such impure radiation has to be eliminated.

Two methods were tried to eliminate the unwanted spectra in the Cd/He laser beam. Prisms were introduced in an attempt to split the main beam from the unwanted spectra, however limited space available in the set–up restricted the effectiveness of this method. Thus light filters were used instead. Blue film filters reduced the intensity of unwanted radiation by 50%, while at the same time it also reduced the intensity of the main beam by 30% due to light absorption of the filters. Filters made of saturated $Cu_2SO_4.2H_2O$ solution eliminated the unwanted radiation by 90%, only reducing the main beam by 13%. The use of saturated solution as a filter is certainly an improvement over

film filters, however the reduced intensity of the main beam has worsened the noise to signal ratio.

In order to increase the signal to noise ratio a low voltage was applied to the photomultiplier since high voltage could introduce noise in the measurement. A noise filtering circuit was also made for current measurements. These have enabled us to achieve a S/N ratio of 5:1 in measurements. When a ruby chip was loaded in the DAC and spectra were taken, the ruby fluresence was not observed. The failure was attributed to the low intensity laser beam available and the inadequate detecting instruments of the weak fluoresence.

B. **Pressure calibration from applied load**

This calibration curve (Fig. 6.5) was provided by the manufacturer of the pressure cell. The relation obtained between the gas pressure and the pressure on the diamond anvils is:

$$P = 0.2\ P_{gas}$$

where P is the pressure on the diamond anvil cell in kbar and P_{gas} the gas pressure in psi.

C. **Pressure calibrated from phase transition**

The characteristics of the substances used and the observed behaviour in this measurement are listed in Table 6.2. For the measurements a microscope (made by Vicker Instruments) was fitted with a 10 w tungsten lamp to illuminate the sample and modified to increase the magnification (from 4 to

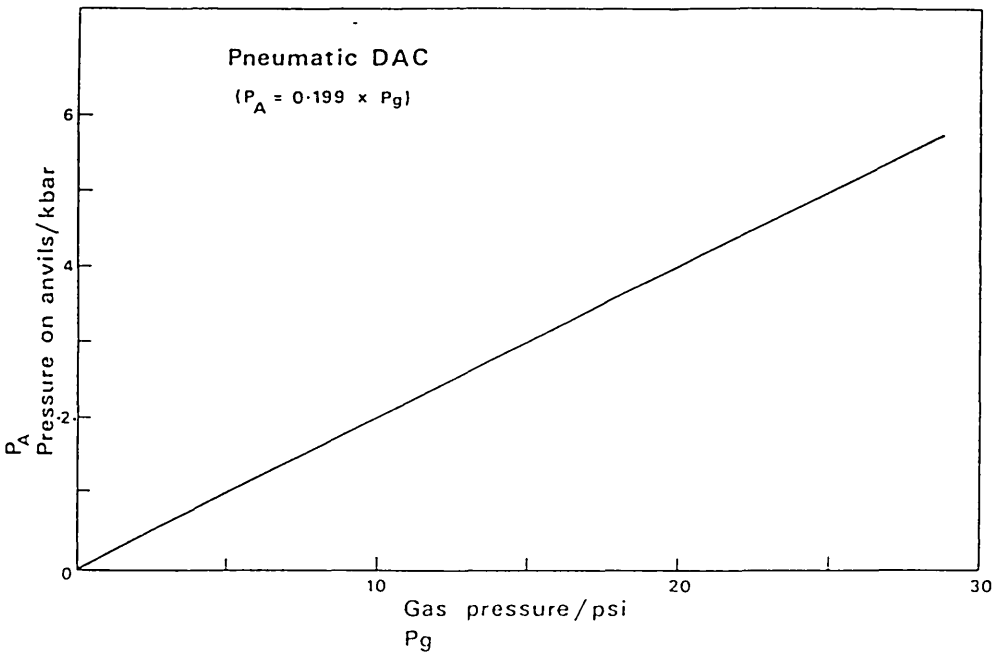


Fig.6.5 The calibration curve provided by the manfacturer.

10). The mobile sample stage on the original instrument was altered to accommodate the DAC.

Samples were loaded and the microscope was focused on the sample. Pressurised gas was introduced and applied on the diamond anvil cell. The gas pressure was obtained from the pressure gauge with an accuracy of 2.5%. When pressure reached the transition pressure of the sample changes could be observed under the microscope. In the begnning of the transition the new phase was observed as an island emerging at the center of the diamond anvils. With increasing pressure the island broke up and spread out forming a ring that represents a boundary between two phases that have diffferent indices of refraction. This observation demonstrated the existence of pressure gradient in the DAC which is depicted in Figure 6.6 by ploting the size of the ring against the gas pressure. From the diagram it is clear that the boundary line expands more slowly towards the diamond edges, indicating that the pressure gradient becomes steeper as the edge is approached. Due to the existence of pressure

Table 6.2 Characteristics of chemicals used in the pressure calibration of the DAC

Chemicals	P_{tran}(kbar)	P_{gas} Psi	Notes
KNO_3	2.3	9.5	Aragonite structure ($P_{nma} = D_{2h}^{1.6}$ Z = 4) ⇒ larger cell unit (z = 10) polar and low symmetry C_{zu}^{7} Ref. 178
AgI	2.4	10.5	Crystal structure change (yellow ⇒ dark brown) Ref. 171 (p.88)
AgI	2.9	16.0	Structure change (dark brown ⇒ transparent light brown) Ref. 171 (p.88)
$HgBr_2$	6.0	27.5	C_{2v}^{12}, Z = 2, Ref. 167 (p.86)
$AgNO_3$	9.8	45.5	Orthorhomic ⇒ Rhombohedral Ref. 178
HgI_2	13.0	60	Crystal structure change (red ⇒ yellow) Ref. 167 (p. 87)

gradient the pressure P indicated in Figure 6.7 is an average value. The obtained calibration curve (Figure 6.7) agrees well with Figure 6.5 in the low pressure range. Due to various errors involved the accuracy of the curve is estimated to be about 15%.

6.8 Characteristics of the ring heater

6.8.1 Relationship between the supplied volatge and the temperature

Figure 6.8 shows the experimental relation between the supplied voltage and the temperature of the ring heater. The temperature was measured by placing the Type K thermocouple in the centre of the ring heater. The voltage was supplied by a standard power supply unit and measured using a R–V–I multimeter with an accuracy of 1%. The temperature has an accuracy of 0.2^{0}C. As expected, temperature increases with rising voltage. Because of the maximum current that the resistant wire can stand, voltages above 10 V were not used.

6.8.2 Temperature gradient

Due to the radiating nature of the ring heater a temperature gradient may exist inside the ring heater. This was observed in one of the experiments. Figure 6.9 shows the simulated environment where the ring heater is sandwiched between two stainless steel plates. On one of the plates three holes were drilled for the placing the thermocouple. The temperature at each hole was measured after the temperature of the system became stable. The results indicated that temperature difference between hole A and C was about 0.4^{0}C, however the difference between B and C was about 15^{0}C. Thus the temperatures measured as near the sample as possible should represent the sample temperature.

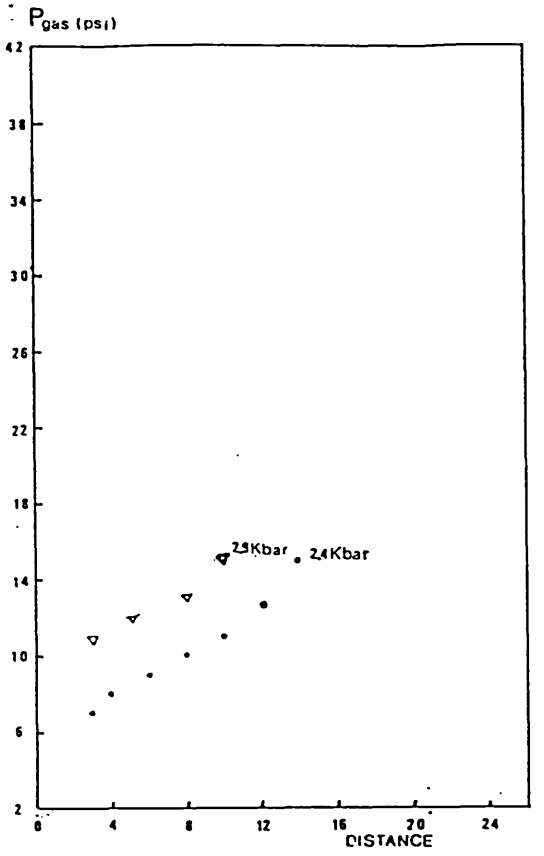


Fig.6.6 Plots of the transition ring size at different pressures.

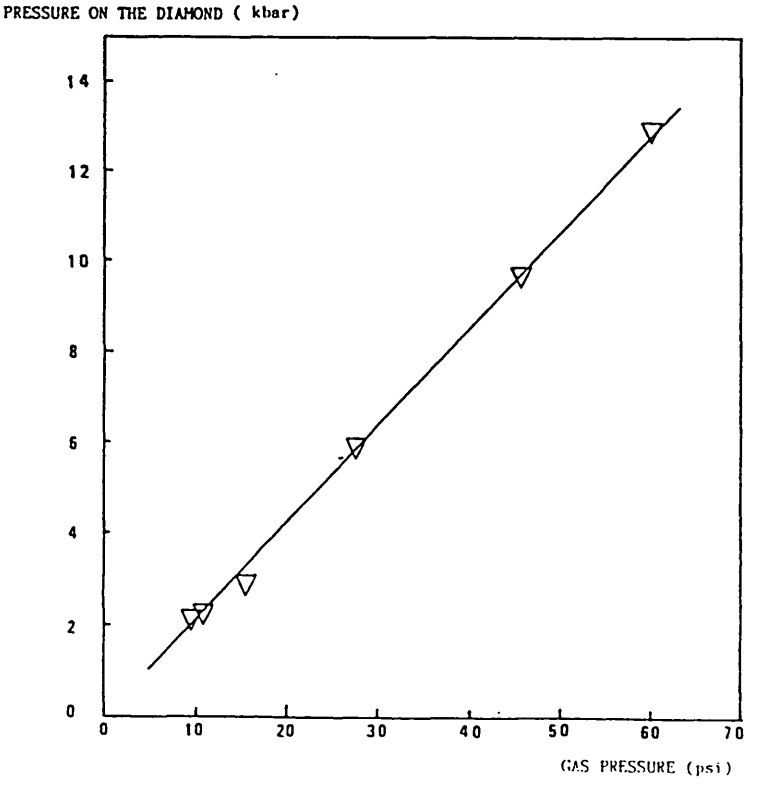


Fig.6.7 The calibration curve obtained from phase transition measurements.

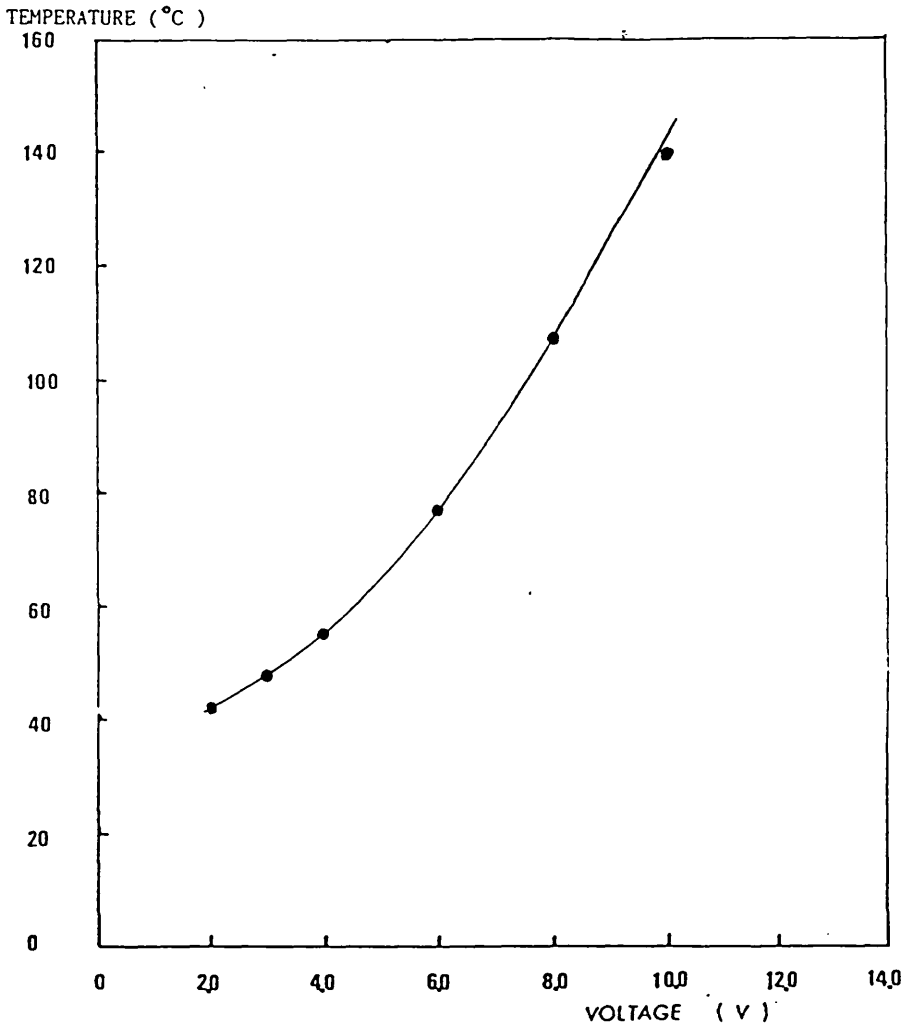


Fig.6.8 The relation between voltage applied and the temperature achieved in the ring heater.

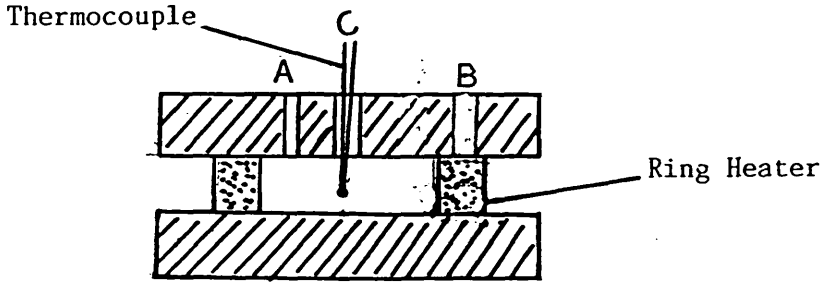


Fig.6.9 The simulated environment for the measurements of temperature gradient in the ring heater.

6.8.3 Temperature control

The temperature control mechanism of the ring heater is schematically shown in Figure 6.10. Because the temperature ramp has no temparature

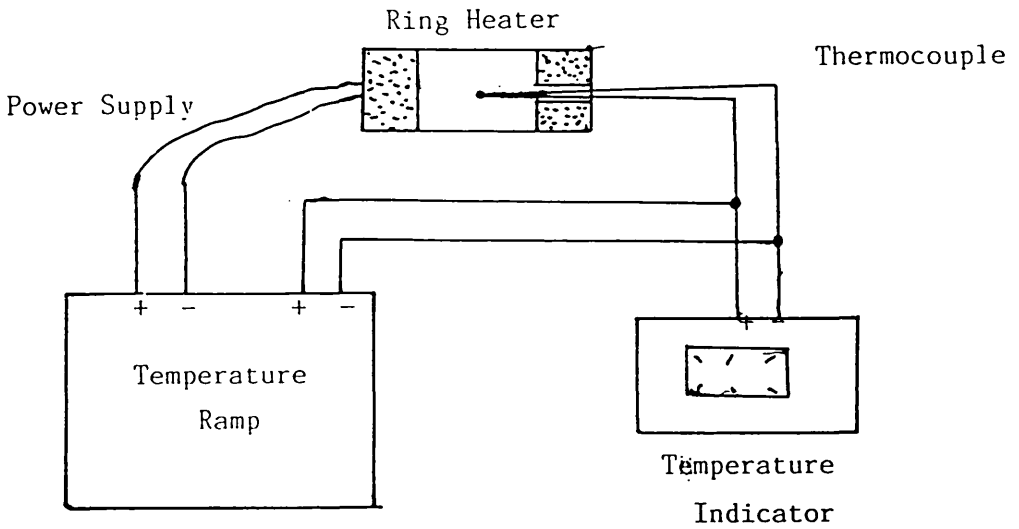


Fig.6.10 A schematic diagram of temperature control mechanisms of the ring heater.

indicator a separate digital thermometer is used. In order to save space for the ring heater the thermocouple for the digital thermometer is placed inside the ring heater and the one for the temperature ramp is connected with the digital thermometer. Experiments show no difference in temperature between this arrangement and the normal connection.

6.8.4 Temperature fluctuation

Under the condition of constant power supply temperature of a heated system will depend on the heating mass and the heating environment. In the experiment of pressure jump temperature fluctuation was noted. One typical plot of temperature against time after pressure jump to zero pressure is shown

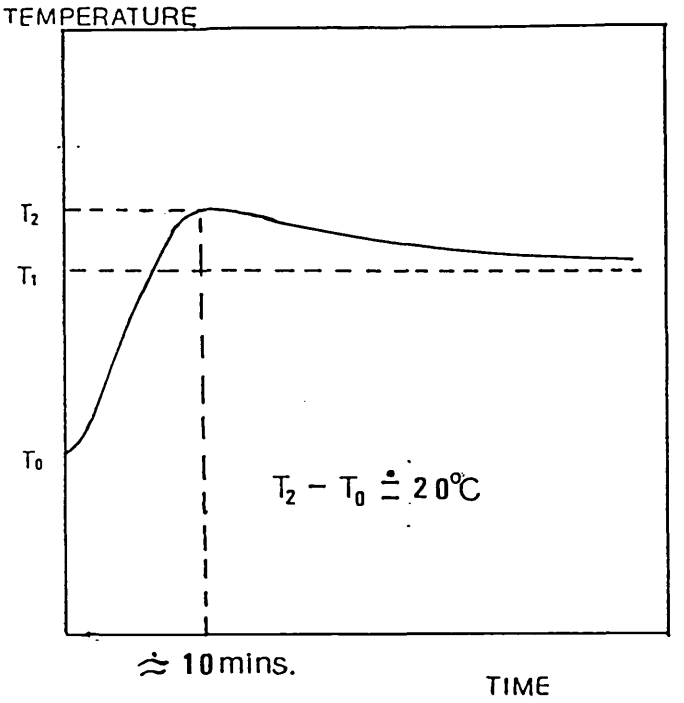


Fig.6.11 Temperature fluctuation after a pressure jump to zero pressure.

in Figure 6.11. The initial temperature increase after the pressure jump is due to the reduced heating mass when the bottom diamond mounting plate is off contact with the heater. The small decrease in the later time is due to the heat loss to the environment. This indicates that measures are required to maintain the temperature when a pressure jump to zero is used.

6.9 Characteristics of the optical system

6.9.1 Distortion of scattering angle

The use of lens and diamond anvils has changed the scattering angle as shown in Figure 6.12. The change of scattering angle due to the condensing effects of lens is θ. And

$$\tan \theta = \frac{x}{I}$$

since x, being half of the beam size (0.4 mm), is small, l the focus length (50 mm) is large, θ therefore can then be neglected.

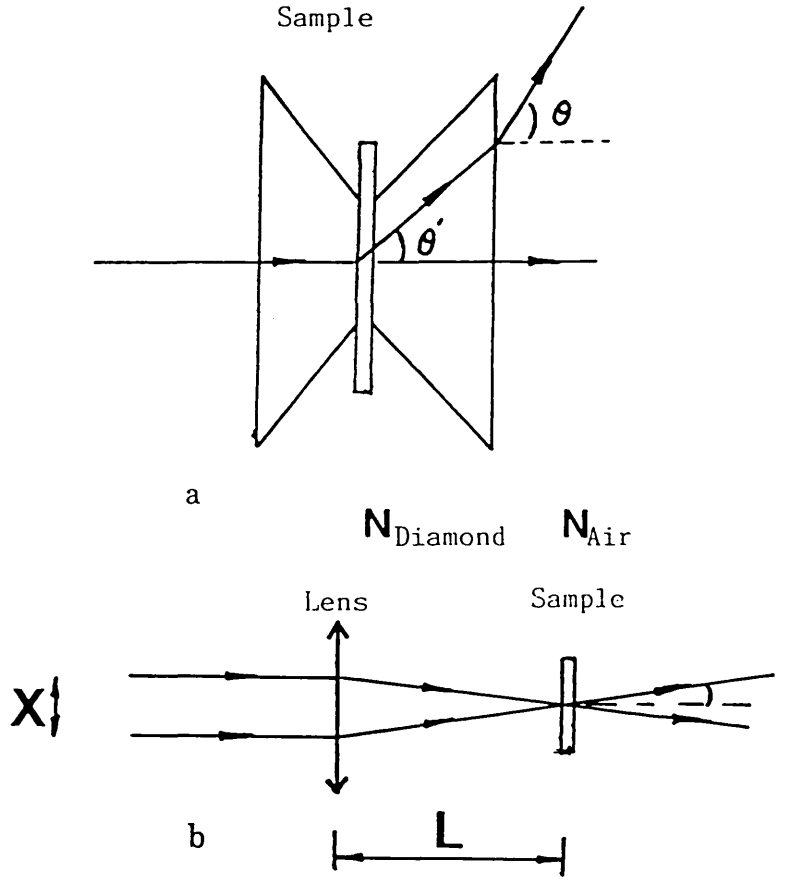


Fig.6.12 Distortion of scattering angles due to the presence of diamond anvils and a lens. a) Diamond anvils, b) lens.

The change of scattering angle due to the presence of diamond can be obtained from the simple relation of light refraction.

$$-\frac{\sin\ \theta'}{\sin\ \theta} = \frac{1}{n_{diamond}} = \frac{1}{2.38}$$

Here θ is the distorted scattering angle and θ' the true scattering angle.

$N_{diamond}$ is the refractive index of diamond

6.9.2 Statistics of the scattered intensity

The small diamond anvil face and therefore small samples for the study have deteriorited the signal to noise ratio of the detecting system. In order to reduce the noise level a capacitor was connected between two ends of the power supply unit of the photodiodes and the measured scattered intensity was averaged after 30 counts by the computer. Comparing with an error of about 30% when no such measures were taken, such measures have reduced the error to less than 10%.

Chapter 7

Preliminary experiments with the use of the pressure cell

7.1 Pressure effects on the cloud points of polystyrene and poly(vinyl methyl ether) system

In this experiment polystyrene with Mn = 3.9 x 10^5 (Mw/Mn = 2.5) and poly(vinyl methyl ether) with Mn = 8.9 x 10^3 (Mw/Mn = 9.8) were used. The sample with a concentration of 50/50 was prepared by the usual method of solvent casting from a toluene solution. A square piece of the prepared film was loaded into the pressure cell, the cell was then assembled and pressure applied. After connecting the heater with the ramp and placing the thermocouple in position the temperature of the sample was increased at a rate of 0.4°C/min and the scattered intensity was collected. The cloud point was taken as described before. The measured cloud points at different pressures are plotted in Figure 7.1. Clearly pressure has increased the cloud point of the system. A value of 13°C/Kbar is obtained for $\frac{dT}{dP}$.

The value of $\frac{dT}{dP}$ obtained here is less than has been determined by Mbamali[93], however the extrapolated cloud point at zero pressure is in agreement with the above author. This observation probably indicates that the present set–up is capable of studying pressure effects on cloud points, but the measured value in this apparatus may be different from other measurements due to the existence of pressure induced shear in the sample. The presence of moisture in the sample may also contribute to the lower $\frac{dT}{dP}$. The lower cloud points observed in this experiment may be indicative of the moisture presence in the sample.

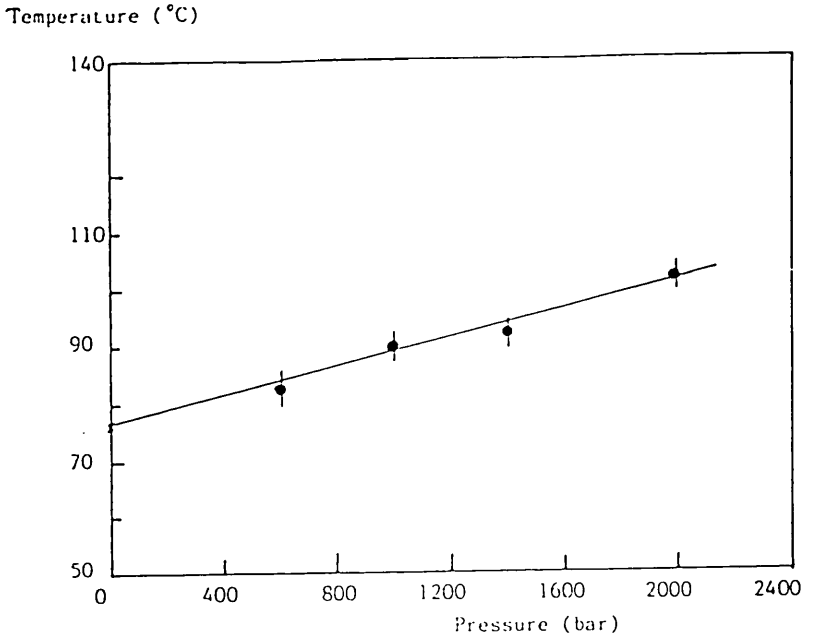


Fig.7.1 The determined cloud points of PS/PVME (50/50) at different pressures.

7.2 Experiments on mixtures of Solution Chlorinated Polyethylene (SCPE) with Ethylene Vinyl Acetate copolymer (EVA)

A: Miscibility of the SCPE/EVA system

Due to the limitation of maxmimum temperature in the present set–up efforts have been made to find a system which phase separates around 90°C and is suitable for studies in the pressure cell. Extensive studies[32,33,107,109] in this laboratory have shown that the phase separation temparature of SCPE/EVA mixture can be easily altered by changing the chlorination of SCPE. Thus this system is chosen for the preliminary study of kinetics of phase separation via a pressure jump.

SCPE's with different chlorination levels are made in this laboratory using the well documented procedure[32]. In order to make large quantities of such material a few modification were made to the operation, which is described in detail in an internal report[182]. The chlorine content is measured by

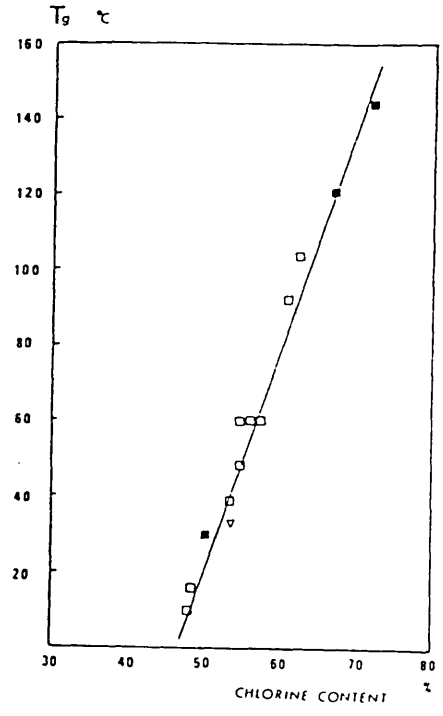


Fig.7.2 The glass transition temperature of SCPE at different chlorine contents. □ ——this experiment, ■ —— R.Hill's results

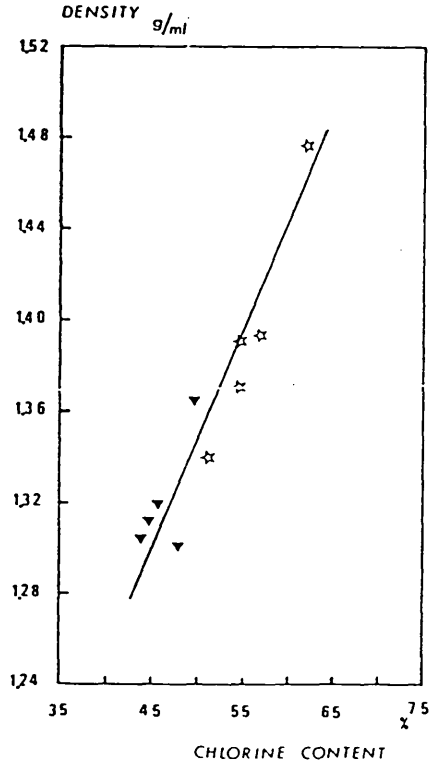


Fig.7.3 The density of SCPE at different chlorine contents.
☆—— this experiment, ▲—— Zhai's results.

Table 7.1 Characteristics of SCPE's and EVA-45

Material Code	Chlorine Content	Molecular Weight*	Tg (°C)	Density g/cm³
SCPE-3-2	54.8%	Mw = 2.89 x 10^5 Mn = 7.72 x 10^4	48	1.3685
SCPE-4-2	53.5%	Mw = 3.41 x 10^5 Mn = 1.11 x 10^5	39	-
SCPE-11	54.6%	Mw = 3.87 x 10^5 Mn = 9.74 x 10^4	60	1.3893
SCPE-12	57.1%	Mw = 3.05 x 10^5 Mn = 6.72 x 10^4	60	1.3935
SCPE-14	56.6%	Mw = 2.43 x 10^5 Mn = 6.18 x 10^4	60	-
SCPE-15	61.2%	Mw = 1.41 x 10^5 Mn = 4.99 x 10^4	90	1.3994
SCPE-13	62.2%	Mw = 3.05 x 10^5 Mn = 9.67 x 10^4	103	1.4771
SCPE51	51%	Mw = 6.75 x 10^4 Mn = 5.66 x 10^4	23	-
EVA45	45% ethylene vinyl acetate	Mw = 1.14 x 10^5 Mn = 4.75 x 10^4	-30	-

* Polystyrene equivalent

elemental analysis and the glass transition temparature is obtained in DSC measurements with a heating rate of 20°C/min. The relation between the chlorine content and Tg of SCPE is depicted in Figure 7.2. A linear dependence between them is found. The density of each SCPE was also measured in the same way described by Zhai[32] and a linear relationship between the density and chlorine content is found (Figure 7.3). All these results together with characteristics of the materials used in this study are compiled in Table 7.1.

Mixtures of SCPE and EVA45 were prepared by solvent casting using THF as a common solvent. The cloud points of the mixtures were obtained by the usual procedure with a heating rate of 0.4°C/min. The results obtained are shown in Figure 7.4.

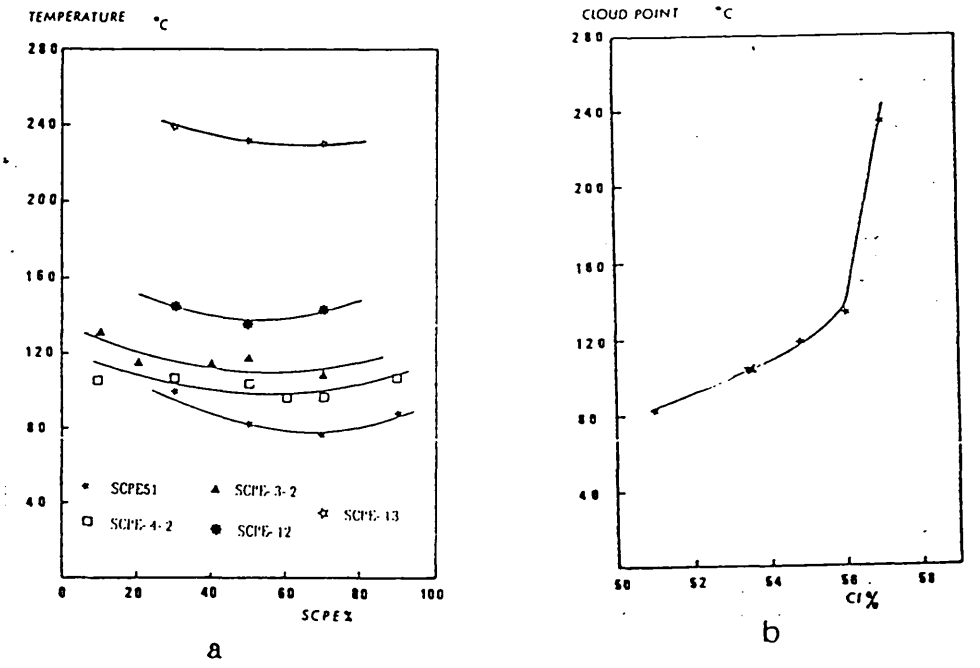


Fig.7.4 a) The cloud point curves of SCPE/EVA 45 mixtures at different chlorination level of SCPE.

b) Clond points of 50/50 SCPE/EVA 45 mixtures against chlorine contents.

As expected the cloud point increases with rising chlorine content and eventually SCPE and EVA become completely miscible. (This means that phase separation is not observed before severe degradation of the component polymers.) The increase may be attributed to the enhanced specific interaction between the –H group in SCPE and the –C=O group in EVA when chlorine content is increased. Over the range of chlorine content tested here a ratio of 10^0C per chlorine content is obtained.

B: Kinetics of phase separation via a pressure jump

In this measurement a 50/50 mixture of SCPE–51/EVA–45 is used since this mixture has a cloud point of 82^0C. When the pressure cell is loaded with the sample (a 4mm x 4mm x 0.2mm film) and assembled, a pressure P1 is applied and sample temperature is increased. The combination of pressure P1 and the chosen temperature to ensure that the sample in study is in the one phase region. When temperature reaches the chosen temperature T_0 and becomes stable, pressure is quickly reduced to P2 the sample will then be in the two phase region and start to phase separate. The pressure change on the pressure gauge takes about 5 seconds. Inside the pressure cell such change may be much quicker than this because the mechanism of pressure measurements in the pressure gauge slows down the reponse to pressure change. A plot of scattered intensity against time at $P_2 = 800$ bar is shown in Figure 7.5. From this figure we can see that the scattered intensity exponentially increases with time in the early stages of phase separation and levels off in the later stages as has been observed before. However the time range of the phase separation has risen from about 400 sec. when pressure is not applied to about 1200 seconds at pressure of 800 bar. Such change indicates that pressure has dramatically slowed down the phase separation process in this blend.

A plot of Ln(intensity) against time, corresponding to Fig.7.5 is depicted in Figure 7.6. From the slope of the straight line between 400 sec to 1200 sec the rate of phase separation R(Q) can be obtained. R(Q) against wavevector Q at 800 bar is shown in Figure 7. 7. In this plot it is observed that the Qm is outside the Q range of the present equipment. This observation is in agreement with the determination of Fernandez *et al*[108]. The application of pressure may also contribute to this because Qm will rise with pressure as the absolute value of $\frac{\partial^2 G}{\partial \phi^2}$ increases with increasing pressure. The much smaller R(Q) observed (in the order of $10^{-4} \sim 10^{-5}$ sec^{-1}) than in normal conditions (R(Q) in the order of $10^{-2} \sim 10^{-3}$ sec^{-1}) again shows that pressure has reduced the rate of phase separation process.

According to the C–H theory a plot of $R(Q)/Q^2$ against Q^2 shoud give a straight line. The plot of such at 800 bar is shown in Fig.7.8.

A linear relation between $R(Q)/Q^2$ and Q^2 is observed. Similar behaviour at other pressures was also found. From the intercept and the slope of this plot the apparent diffusion coefficient, D_{app} and MK are determined. The results are listed in Table 7.2. In Figure 7.9 and Figure 7.10 the obtained values of Dapp and MK are plotted against pressure. In both cases rather curved plots are found.

The changes of both Dapp and and MK with pressure are related to the decrease of the free volume of the system under pressure. The decrease of the free volume will in turn affect both the interaction between the two components (i.e. $\frac{\partial^2 G}{\partial \phi^2}$) and the diffusional processes (i.e.M). The relationship between M and pressure can be deduced from the dependence of the diffusion coefficient on the fractional free volume[70] and the effects of pressure on the fractional free volume. The obtained equation is:

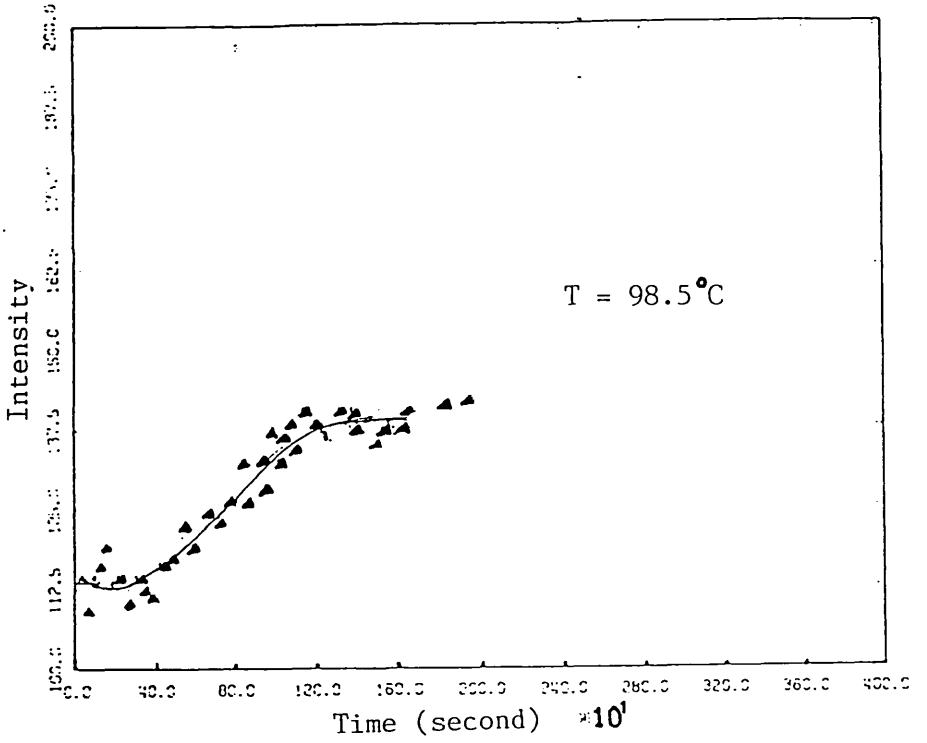


Fig.7.5 A plot of scattered intensity against time at pressure 800 bar.

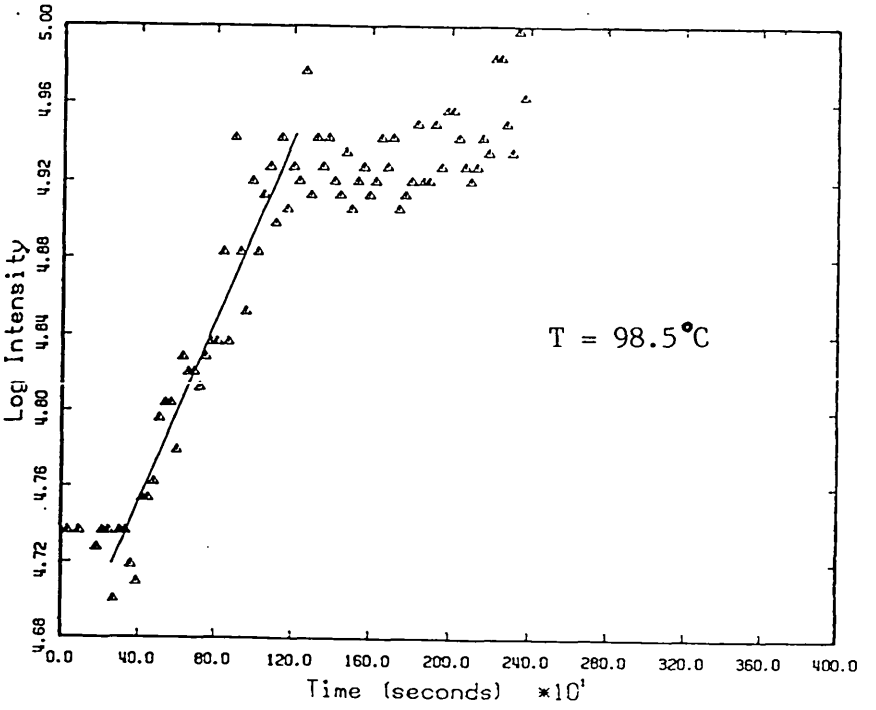


Fig.7.6 A ln (intensity) against time at pressure 800 bar.

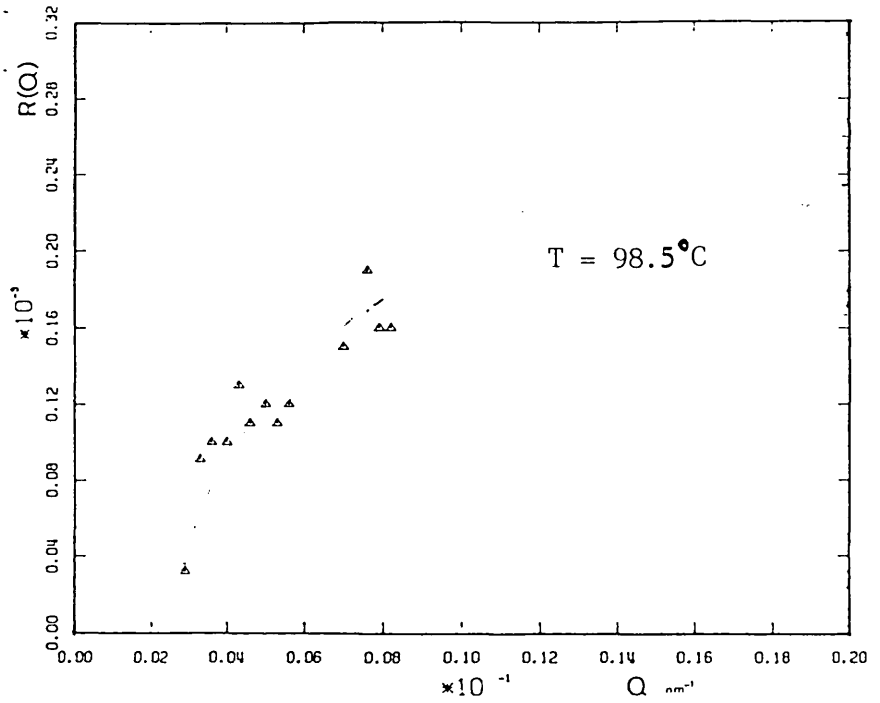


Fig.7.7 A plot of R(Q) against Q at pressure 800 bar.

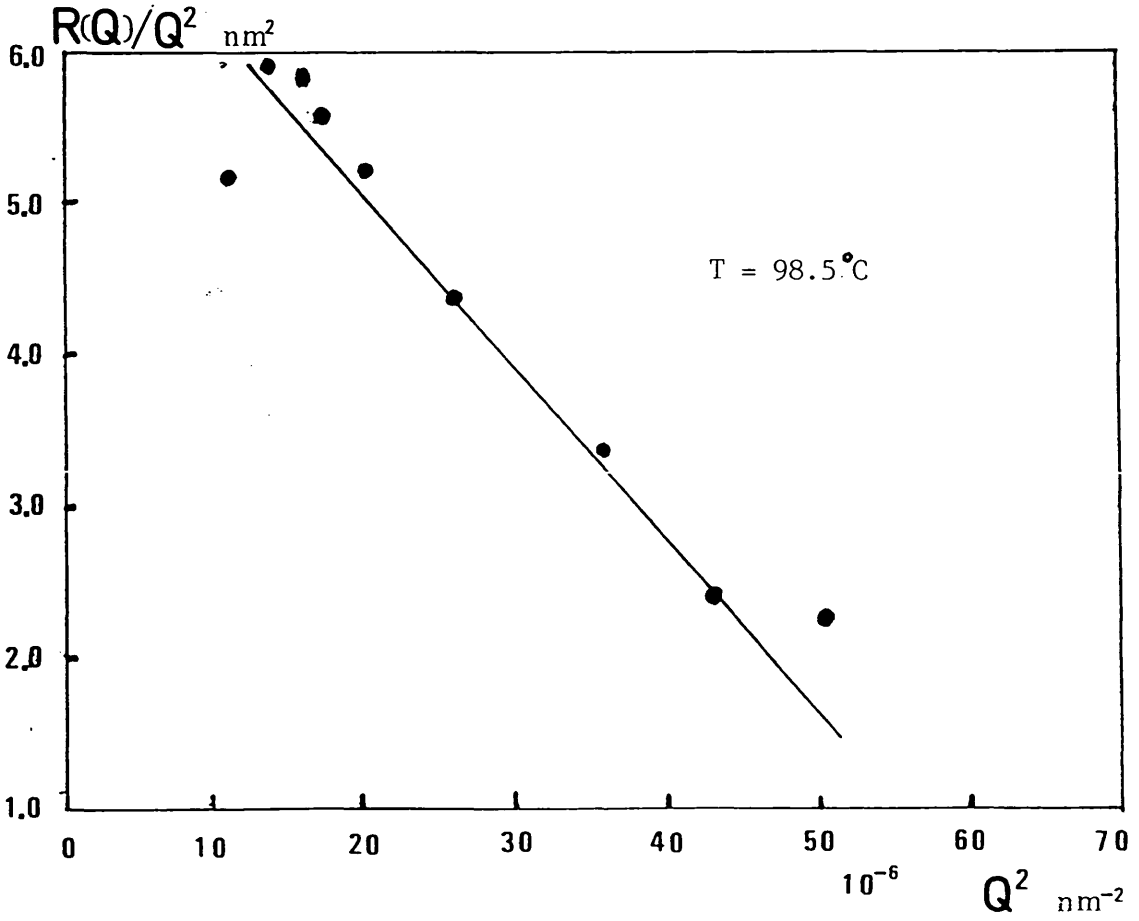


Fig.7.8 A plot of $R(Q)/Q^2$ against Q^2 at pressure 800 bar.

Table 7.2 Data of kinetics of phase separation of SCPE51/EVA45(50/50) under pressure

Pressure (bar)	Temperature (^{0}C)	Dapp nm^2/sec	MK nm^4/sec	Dapp/MK nm^{-2}
0*	95.6	6.3×10^2	2.56×10^7	0.246×10^{-4}
600	94.5	6.77-7.07	0.995×10^5	0.695×10^{-4}
800	94.5	0.372	0.618×10^4	0.60×10^{-4}
1000	94.5	0.397	0.128×10^4	3.1×10^{-4}
800	98.5	7.54	0.43 x10	1.75×10^{-4}
1000	98.5	0	0	-
800	101.5	4-5	-	-
1000	102.0	-	-	-

* Taken from Ref. 107

$$M = A_d\, 10^{-\frac{C}{f_0 - \beta_f(p - p_0)}} \qquad 7.1$$

Where A_d, C (= 1/2.303) are constant, f_0 the fractional free volume at an arbitary chosen temperature (normally at the glass transition temperature Tg), and equal to 0.025, P the pressure, β_f is the compressibility. Within a small pressure range it can be treated as a constant.

The change of K with pressure depends on the effects of pressure on the radius gyration of the components. Experiments[76,77] conducted for polymer solutions have indicated that the change of the radius gyration of polymers with pressure are quite small. Thus K can be considered as independent of pressure.

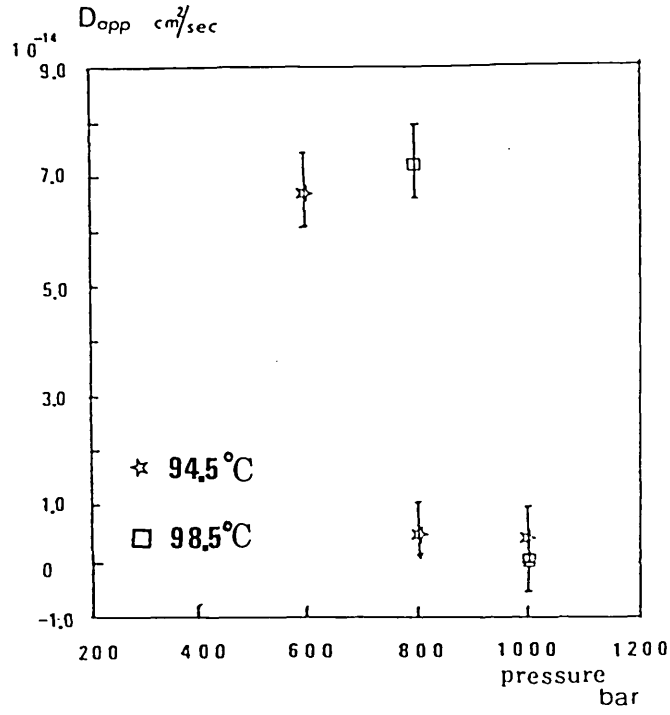


Fig.7.9 A plot of the apparent diffusion coefficient, D_{app}, against pressures.

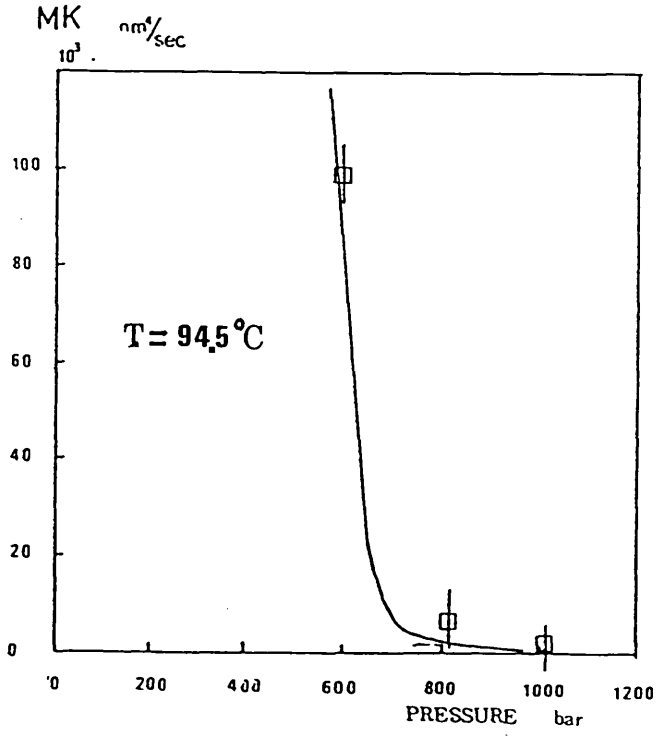


Fig.7.10 A plot of MK against pressure.

The solid line is drawn according to equation 7.1 with

Ad = 7.17 x 10^{27} nm^4/sec and β_f = 1 x 10^{-5} atm^{-1}

Since K is considered as constant in this case the change of MK with pressure observed here reflects the effects of pressure on M, the diffusion coefficeint. The solid curve in the plot in Figure 7.10 is drawn according to Equation 7.1 with the use of $A_d = 7.17 \times 10^{27}$ nm^4/sec and $\beta_f = 1 \times 10^{-5}$ atm^{-1}. A fairly good agreement between the experimental points and the curve is found. This indicates that the equation is able to describe the pressure effects on the diffusion coefficient.

In order to look at the effects of pressure on the thermodynamic driving force of $\frac{\partial^2 G}{\partial \phi^2}$. A plot of Dapp/MK against pressure is shown in Figure 7.11. The trend of this plot indicates that $\frac{\partial^2 G}{\partial \phi^2}$ is becoming more negative with increasing pressure. However limited data and poor statistics have prevented us from doing further detailed analysis.

The dependence of $\frac{\partial^2 G}{\partial \phi^2}$ on pressure can be described by the simple F–H theory if we assume the pressure effects on $\frac{\partial^2 G}{\partial \phi^2}$ is confined to the interaction parameter χ_{12}. Following Koningsveld's treatment we have:

$$\frac{\partial^2 G}{\partial \phi^2} = \left[\frac{\partial^2 G}{\partial \phi^2}\right]_{p_0} - D(p - p_0) \qquad 7.2$$

where D is a concentration dependent constant.

In Figure 7.11 the solid curve is plotted with $D = 4.4 \times 10^{-4}$ bar^{-1}. Here an agreement between experimental points and Equation 7.2 is found. This idicates that the effects of pressure on $\frac{\partial^2 G}{\partial \phi^2}$ can be empirically described.

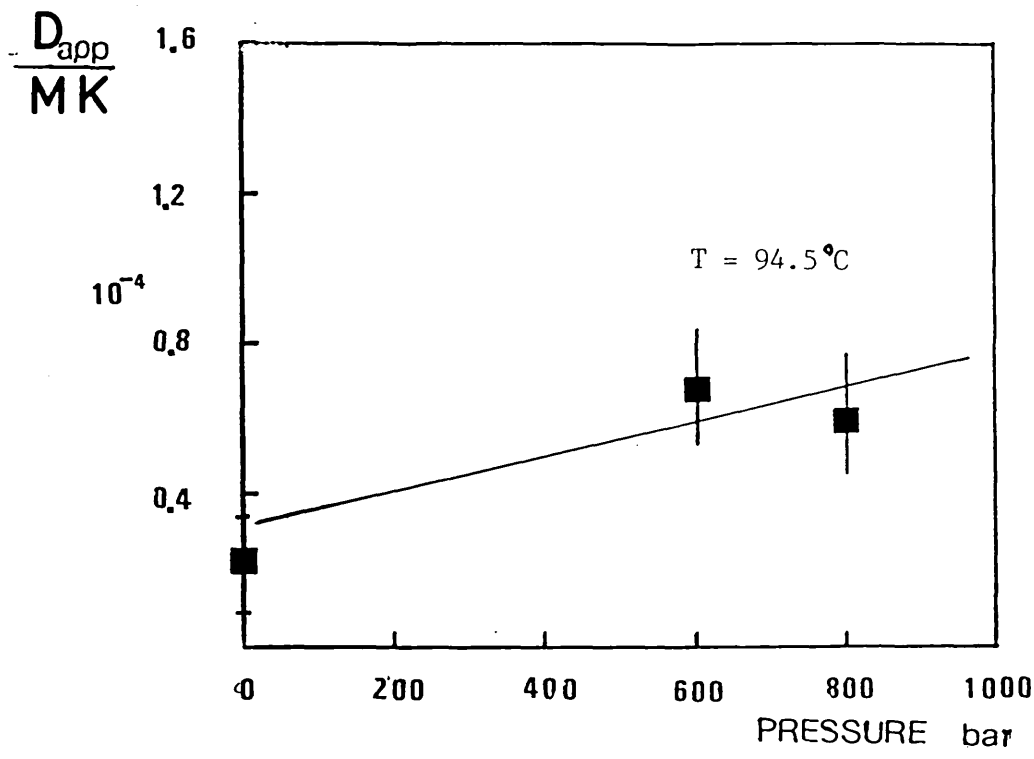


Fig.7.11 A plot of D_{app}/MK against pressures. The solid line is drawn with $D = 4.4 \times 10^{-4}\ bar^{-1}$

Chapter 8

Conclusions and Recommendations

8.1 TMPC/PS system

8.1.1 Miscibility

This study has confirmed earlier observations that TMPC and PS are miscible when they are mixed in ethylene chloride. The relevant observations are single glass transition temperature in the mixture, and the cloud points. The miscibility of TMPC and PS is solvent dependent. LCST observed in this system is found to be dependent on the experimental heating rate, the molecular weight of PS and the sample thickness. The obtained phase boundary is symmetrical with a critical temperature of 235^{0}C.

8.1.2 Kinetics of phase separation

Due to the slow diffusion the early stages of spindal decomposition was followed in this study. During the early time period the following features predicted by the C–H theory were observed for the TMPC/PS 50/50 mixture.

1. Development of a scattering maximum.
2. Exponential growth of the most rapidly growing wavevector.
3. An approximately time invariant correlation length, and
4. Observation of an interconnected structure.

The $R(Q)/Q^2$ vs Q^2 plot was found to be apparently linear as predicted by the C–H theory, however the obtained Q_m from such plots neither agrees

with the one obtained from R(Q) vs Q plots ,nor shows a correct temperature dependence. Moreover the observed ratio of Q_c/Q_m is always greater than the predicted value of $\sqrt{2}$. Such disagreements may be mainly attributed to the effects of thermal fluctuation on the phase separation of this blend.

The obtained diffusion coefficient D_{app} in the order of 10^{-15}~10^{-16} is smaller than those observed in other systems. The difference may result from the small thermodynamic driving force $\frac{\partial^2 G}{\partial \phi^2}$ seen in this blend (in the order of 10^{-5}). The small $\frac{\partial^2 G}{\partial \phi^2}$ may be associated with the peculiar specific interaction observed in this blend. The D_{app} was found to be a linear function of phase separation temperature within the tested temparature range, and the extrapolated spindal temperature agrees well with the obtained cloud point.

The correlation length obtained cannot be predicted by the Van Aartsen's equation, and may be rightly so, since the original F–H theory used in the deduction of this equation has failed to describe the thermodynamic behaviour of polymer blends, let alone the special phenomena in this system.

In conclusion the simple C–H theory can qualitatively predict the behaviour of the early stages of spinodal decomposition in this blend. Quantitative description may require the inclusion of thermal fluctuation effects in the theory.

8.2 PES/PEO system

8.2.1 Miscibility

Clear evidences of a single glass transition temperature of the mixtures and existence of LCST in the system again support observations of miscibility between PES and PEO. The observation of a negative interaction parameter,

χ_{12}, from the melting point depression measurements supports such a claim. Being different from Singh's observation, cloud point temperatures larger than the glass transition temperatures of the mixture were observed in this study (Figure 8.1). Spinodal points were also determined in this study. A good agreement between the spinodal point and the cloud point was found at the critical concentration.

8.2.2 Crystallization behaviour of PEO in the mixture.

Contrary to the prediction of the Hoffman's equation, curved plots of T_m against the annealing temperature T_c were observed. The curvature of the plot may indicate that the morphology of the crystal (especially the crystal thickness) is changing with T_c. The determined equilibrium melting temperature by extrapolating the linear region of the T_m vs T_c plots was found to decrease with increasing PES concentration. Treatments of the melting point depression data, based on the equation outlined in Chapter 2, have resulted in a negative interaction parameter χ_{12} between PES and PEO. The large value of χ_{12} determined may indicate the inadequacy of the Hoffman's equation for determining the equlibrium melting temperature, and the simple F–H theory. Larger errors involved in the determination and the neglect of concentration effects on χ_{12} make the absolute value of χ_{12} little importance.

The Avrami equation could be used to describe the crystallization behavior of PEO in the mixture. With the addition of PES in the mixture a steady decrease of crystal growth was observed due to reducing mobility of PEO chains. The results indicated a three dimensional crystal growth with N ranging from 1.9 to 4.0.

8.2.3 Kinetics of phase separation

The rapid phase separation of PES/PEO system has made the observation of early stages of spinodal decomposition more difficult. Nonetheless, the following features predicted by the simple C–H theory were observed in this study, indicating that such study was conducted in the early part of spinodal docomposition.

1. Development of a scattering maximum.
2. Exponential growth of the most rapidly growing wavevector,and
3. An approximately time invariant correlation length.

However the obtained $R(Q)/Q^2$ vs Q^2 plots were not linear, which is in obvious disagreement with the C–H theory. The determined Q_c/Q_m also disagrees with the predicted value of $\sqrt{2}$. The non–instaneous temperature jump and thermal fluctuation may be to blame for the disagreements.

8.3 Studies with the pressure cell

8.3.1 Experiments

Among the variety of pressure cells a diamond–anvil pressure cell was chosen and constructed according to the requirements. This cell was proven to be able to achieve a maximum pressure of 5 kbar. The heater fitted with the cell was capable of raising the sample temperature up to 150^{0}C. Subsequent pressure calibration using three different methods produced a pressure calibration curve with an accuracy of 15%, which was then used in the study of polymer systems of PS/PVME and SCPE/EVA.

Measurements of cloud points of PS/PVME (30/70) at different pressures, using the present set–up, haveshown that the cloud points rise with increasing pressure at a rate of 13^{0}C/kbar. The disagreement between this result and the one obtained by Mbamali was interpreted as the results of different techniques being used and the presence of moisture in the sample. The possibility of shear on the sample in this study may also play a part.

Studies of phase separation of SCPE–51/EVA45 (50/50) at different pressure showed that the present apparatus was capable of performing kinetic studies via a pressure jump. Measurements demonstrated that phase separation of this blend was substantially slowed down by the application of pressure due to the decrease of thermodynamic driving force and the mobility of polymers with rising pressure. The obtained relation between D_{app} and pressure was in qualitative agreement with existing theory.

8.3.2 Recommendation on further pressure experiments

The present set–up, although applicable in conducting experimental study of polymer blends, is not ideal. Further improvements are required to make it more efficient. Recommendation for such improvements is as follows.

1. A newly designed heating system is highly required to achieve a higher working temperature and more stable control of temperature when pressure is released. Such a system should preferbly consist of two parts with one ring heater inside the pressure cell and the other heater fitted outside the cell. The ring heater inside is to heat the sample to the required accurate temperature, while the outside heater is mainly to reduce the heat loss and to keep the sample temperature stable.

2. A new assembly of the ring heater is needed to replace the present method. The best available solution to this problem would be to machine a cylinder in the bottom diamond mounting plate and fit the ring heater on the cylinder. This will ensure a more reliable assembly and allow a thicker ring heater to be made.

3. A more accurate pressure calibration curve is highly desirable. Among the methods and materials available calibration using tetra methylamine crystal deformation under pressure should be the first choice.

4. To further reduce parasitic scattering from the optical system modification of the present assembly is necessary.

5. Further detailed studies on pressure effects on phase boundaries of polymer blends, together with improvement of theoretical treatment, are required. Pressure effects on the spinodal decomposition of polymer blends should be included in various theories and the spinodal decomposition of polymer blends under pressure and morphologies of polymer blends should be studied.

REFERENCES

1. C.B. Bucknall,
   "Toughened Plastics", Applied Science Publishers Ltd, London 1977.
2. J.A. Manson and L.H. Sperling,
   "Polymer Blends and Composites", Heyden, 1976.
3. A. Dobry and F. Boyer–Kawenoki,
   J. Polym. Sci., 2,90 (1947).
4. R.J. Kern and R.J. Slocombe,
   J. Polym. Sci., 15,183 (1955).
5. O. Olabisi, L.M. Robeson.,and M.T. Shaw,
   "Polymer–Polymer Miscibility", Academic Press, N.Y., 1979.
6. D.R. Paul and S. Newman, Eds.
   "Polymer Blends", Academic Press, 1978.
7. D.J. Walsh and S. Rostami,
   Ad. Polym. Sci., 70,119 (1985).
8. J.W. Barlow and D.R. Paul,
   Poly. Eng. and Sci., October v21 N15 985 (1981).
9. A.R. Shultz and B.M. Beach,
   Macromolecules 7, 902 (1974).
10. P.J.Flory,
    J. Chem. Phys., 9,660 (1941).
11 P.J.Flory,
   J. Chem. Phys., 10,51 (1942).
12. M.L.Huggins,
    J. Chem. Phys, 9,440 (1941).

13. M.L.Huggins,
Ann. N.Y. Acad. Sci., 43,1 (1942).

14. H.Tompa,
"Polymer Solutions" Butterworth, London, 1956.

15. R. Koningsveld and L.A. Kleintjens
J. Polym.Sci., Polymer Symposium 61,221 (1977).

16. P.J. Flory, R.A. Orwell and A. Vrij
J. Am. Chem. Soc., 86,3507 (1964).

17. P.J. Flory,
J. Am. Chem. Soc., 87:9, 1833 (1965).

18. L.P.McMaster,
Macromolecules, 6,760 (1973).

19. D. Patterson and A. Robard,
Macromolecules, 6,690 (1978).

20. D.J. Walsh and S. Rostami,
Polymer, 26,418 (1985).

21. S. Rostami and D.J. Walsh
Macromolecules, 17,315 (1984).

22. O.Olabisi,
Macromolecules, 8,316 (1975).

23. G.ten Brinke, A. Eshuis, *et al*,
Macromolecules, 14,867 (1981).

24. D.J. Walsh and J.G. McKeown,
Polymer, 21,1330 (1980).

25. L.E.Nielsen,
J. Polymer Sci., 42,357 (1980).

26. C.D. Doube and D.J. Walsh,
Polymer, 20,115 (1979).

27. C.C. Hsu and J.M. Prausnitz,
Macromolecules, 7,320 (1974).

28. M. Bank, J. Lettingwell and C. Thies,
Macromolecules, 4,43 (1971).

29. A.R. Shultz and A.L. Young,
Macromolecules, 13,663 (1980).

30. L. Bohn,
"Polymer Handbook", J. Brandrup and E.H. Immergent, Eds.,Wiley, N.Y., 1975.

31. S.L. Rosen,
Polymer Eng. Sci., 7,115 (1967).

32 Z.Zhai,
Ph.D Thesis, Imperial College, 1983.

33. S. Rostami,
Ph.D. Thesis, Imperial College, 1985.

34. C.K. Sham, PhD Thesis, Imperial College, 1985.

35. S.B. Newman,
"Analytical chemistry of Polymers" (G.M. Kline, Ed.), Vol3, P261.

36. D. Heikens and W. Barensten,
Polymer, 18,89 (1977).

37. T.G. Fox,
Bull. Am. Phys. Soc., (2) 1,123 (1956).

38. J.R. Fried, F.E. Karasz and W.J. MacKnight,
Macromolecules, 11,150 (1979).

39. W.M. Prest and R.S. Porter,
J. Polym. Sci., Phys.Ed., 10,1693 (1970).

40. D.R. Paul and J.O. Altamirando,
Adv. Chem Ser., 142,371 (1975).

41. R.E. Wetton, *et al*,
Macromolecules, 11,158 (1978).

42. J.E. Rabek,
"Experimental Methods in Polymer Chemistry", Wiley (1980).

43. M. Kimnra, R.S. Porter and G. Salce,
J. Poly. Sci., Poly. Phys. Ed., 21,367 (1983).

44. T. Nishi and T.T. Wang,
Macromolecules, 8,909 (1975).

45. J. Stoelting, F.E. Karasz and W.S. MacKnight,
Polym. Eng. Sci., 10(3),133 (1970)

46. J.E. Guillet, in
"Progress in gas chromatography", (J.H. Purnell, Ed.), P187, Wiley (Interscience), N.Y., 1973.

47. T.K Kwei, T. Nishi and R.F. Roberts,
Macromolecules, 7,667 (1974).

48. S Ichihara, A. Komatsu and T. Hata,
Polym. J., 2,640 (1971).

49. F.B. Khambata, *et al*,
J. Polym. Sci., Poly. Phys. Ed., 14,1391 (1976).

50. T.P. Russell and R.S. Stein,
J. Polym. Sci., Poly. Phys. Ed., 20,1594 (1982).

51. J.S. Higgins and P.E. Tomlins
Polymer, 26,1554 (1985).

52. C.A. Cruz–Ramos and D.R. Paul,
Macromolucules, 22,1289 (1989).

53 J.F. Parmer, L.C. Dickinson, J.C.W. Chien and R.S. Porter,
Macromolecules, 22,1078 (1989).

54. M. Kerker,
"Scattering of Light and Other Electromagnetic Radiation", AP, N.Y., 1969.

55. M.B. Huglin,
"Light Scattering from Polymer Solutions", AP, London, 1972.

56. H.B. Stuhrmann in
Chapter 15, Spectron Radiation, Eds. H. Winnick and Doniach, Plenum Press, N.Y., 1908.

57. O. Glatter and O. Kratky,
"Small Angle X–ray Scattering", AP, N.Y. 1982.

58. K.D. Pae,
J. Poly. Sci., Poly. Phys. Ed., 21, 1195 (1983).

59. G.D.Patterson, *et al*,
J. Polym. Sci., Poly. Phys. Ed., 21, 605 (1983).

60. J.J.Curro, *et al*,
J. Polym. Sci., Poly. Phys. Ed., 21,1785 (1983).

61. Y. Miyamoto,
Polymer, 25,63 (1984)65

62. E.N. Dalal and D.J. Phillips,
Macromolecules, 16,1754 (1983).

63. D. Crofton and R.A. Pethrick,
Polymer, 23,1609 (1982).

64. G.Fytas,

Macromolecules, 18,993 (1985).

65. R.G. Priest,

Macromolecules, 18, 1504 (1985).

66. E.A. DiMarzio and J.H. Gibbs, *et al*,

Macromolecules, 9,763 (1976).

67. J.D. Ferry,

"Viscoelastic Properties of Polymers", 3rd Ed. John Wiley & Son Inc, N.Y., 1980.

68. D.C. Bassett and B. Tuner,

Nature Phys. Sci., 246,146 (1972).

69. D.C. Bassett, S. Block and G.J. Piermarini,

J. Appl. Phys., 45,4146 (1974).

70. H. Tanaka and T. Takamura,

Polym. J., V12,355 (1980).

71. B.S. Hsiao, M.T. Shaw and E.T. Samulski,

Macro., 21,544 (1988).

72. S.K. Bhateja and K.D. Pae,

J. Macromol. Sci.; Rev. Macromol. Chem., C13,77 (1975).

73. G.V. Schulz and M. Lechner,

J. Poly. Sci. A–2, Vol 8, 1885

74. S. Claesson, et al,

J. Poly. Sci., Poly. Phys. Ed., 21,1873 (1983).

75. H. Geerissen, et al,

J. Appl. Poly. Sci., 27,1277 (1982).

76. D. Gaeckle and D. Patterson,

Macromolecules, 5,136 (1973).

77. J. Roots and B. Nystrom,
Macromolecules, 15,553 (1982).

78. R.E. Robertson,
Macromolecules, 18,2239 (1985).

79. J.A.R. Renuncio and J.M. Prausnitz,
Macromolecules, 9,324 (1976).

80. S. Saeki,
Polymer, 16,445 (1975).

81. M. Ishizawa, et al,
Macromolecules, 11,871 (1978).

82. S. Saeki and N. Kuwahara,
Macromolecules, 19,2353 (1986).

83. S. Saeki, et al.
Polymer, 17,685 (1976).

84. S. Saeki, et al,
Macromolecules, 9,101, (1976).

85. G.V. Schulz and B.A. Wolf,
Makromol. Chem., 184,1303 (1983).

86. L. Zeman, J. Biros and D. Patterson,
J. Poly. Chem., 76,1206 (1972).

87. L. Zeman and D. Patterson,
J. Phys. Chem., 76,1214 (1972).

88. M.J. Onodera,
J. Poly. Sci., Poly. Symp., 61,271 (1977).

89. P. Ehrlich and J.J. Kurpen,
J. Polym. Sci., Part A, 1,3217 (1963).

90. J.B.P. Tripithi,
PhD Thesis, Imperial College, 1979.

91. S. Rostami and D.J. Walsh,
Macromolecules, 18,1228 (1985).

92. D.J. Walsh and S. Rostami,
Macromolecules, 18,216 (1985).

93 G.Mbamali,
PhD Thesis, Imperial College, 1989, (In Preparation).

94 M. Okada and C.C. Han,
J. Chem. Phys., 85(9),5317 (1985).

95. C.C. Han, M. Okada, et al,
Polymer Engineering and Science, 26, No1,3 (1986).

96. H.L. Snyder and P. Meakin,
J. Polym. Sci., Polym. Symp., 73,217 (1985).

97. H.L. Snyder, P. Meakin and S. Reich,
Macromolecules, 16,757 (1983).

98. T. Hashimoto, J. Kumaki and H. Kawai,
Macromolecules 16,641 (1983).

99. H. Yang, M. Shibayama and R.S. Stein, et al,
Macromolecules, 19,1667 (1986).

100. T. Hashimoto, M. Itakura and H. Hasegawa,
J. Chem. Phys., 85(11),6773 (1986).

101. T. Hashimoto, M. Itakura and H. Hasegawa,
J. Chem. Phys., 85(10),6118 (1986).

102. S. Takahiro and C.C. Han,
J. Chem. Phys., 88 (3),2057 (1988).

103. M. Takenake, T. Izumitani and T. Hashimoto,
Macromolecules, 20,2257 (1987).

104 H. Fruitwala,
PhD Thesis, Imperial College, 1988.

105. J.S. Higgins, H. Fruitwala and P.E. Tomlins,
Submited for Polymer, 1988.

106. B. Chu,
"Laser Light Scattering ", Applied Science, London, 1984.

107. R.Hill,
PhD Thesis, Imperial College, 1985.

108. J.S. Higgins, H. Fruitwala and P.E. Tomlins,
British Polymer Journal, submitted

109. M.Fernandes and J.S. Higgins.
Polymer, 30,3 (1989)

110. R.S. Stein, J. Gilmer and N. Goldstein,
J. Polym. Sci., Poly. Phys. Ed., 20,2219 (1982).

111. G.R. Strobl, J.T. Bendler, R.P. Kambour and A.R. Shultz,
Macromolecules 19,2683 (1986).

112. H. Meier and G.R. Strobl,
Macromolecules, 20,649 (1987).

113. J.W. Cahn and J.E. Hillard,
J. Chem. Phys., 31,688 (1959).

114. J.W. Cahn,
Acta.Metall., 14,1685 (1966).

115. H.E. Cook,
Acta.Metall., 18,297 (1970).

116. K. Binder,

J. Chem. Phys., 79(2),6387 (1983).

117. K. Binder et.al,

J. Chem. Phys., 85 (3),1505 (1986).

118. P.G. de Gennes,

J. Chem. Phys., 72,4756 (1980).

119. P. Pincus,

J. Chem. Phys. 75,1996 (1981).

120. I.M. Lifshitz and V.V. Slyozo,

J. Phys. Chem., Solids 19,35 (1961).

121. S. Tomotika,

Proc. Roy. Soc., London, 150,332 (1935).

122. E.O. Siggia,

Phys. Rev., A20,595 (1979).

123. K. Kawasaki and T. Ohta,

Prog. Theor. Phys., 59,362 (1978).

124. H.K. Synder and P. Meakin,

J. Chem. Phys., 79(11),5588 (1983).

125. H.O. Camesin, D.W. Heermann and K. Binder,

Z. Phys.B.– Condensed Matter, 65,89 (1986).

126. J. Crank and G.S. Park

"Diffusion in polymers", Academic Press, London, 1968.

127. P.T. Gilmore and R. Falabella,

Macromolecules, 13,880 (1980).

128. F. Kiepen and W. Borchard,

Macromolecules, 21,1784 (1988).

129. G. Allen, G. Gee and J.P. Nicholson,
Polymer, 2,8 (1961).

130. R. Koningsveld, L.A. Kleintjens and H.M. Schoffeleers,
Pure Appl.Chem., 39,1 (1974).

131. W.J.C. Orr,
Trans. Fara. Soc., 40,320 (1944).

132. E.A. Guggenheim,
Pro. Roy. Soc. (London), A, 183,203 (1944).

133. M.L.Huggins,
J. Am. Chem. Soc. 64,1712 (1942).

134. A.R. Miller,
Proc. Cambridge Phil. Soc., 39,54 (1943).

135. E.L. Alkin, L.A. Kleintjens and R. Koningsveld,
Makromol. Chem., 185,377 (1984).

136. I. Prigogine, N. Trappeniers and V. Mathot,
Diss. Fara. Soc., 15,93 (1953).

137. B.E. Eichinger and P.J. Flory,
Trans. Fara. Soc., 64, 2035,2053,2061,2065 (1968).

138. R. Koningsveld,
"Partial Miscibility of Multicomponent Polymer Solutions" in Advances in Colloid and Interface Science, MS743/68.

139. T. Swelheim, J. de Swaan Arons and G.A.M. Diepen,
Rec. Trav. Chim., 84,261 (1965).

140. I. Sanchez and D. Marzio,
Macromolecules, 4, 677(1971).

141. P.J. Flory,
"Principles of Polymer Chemistry", Cornell University, 1953.

142. S. Rostami, Private Communication.

143. J.J. Van Aartsen,
Europ. Poly. J., 6,919 (1970).

144. J.P. Gunton, M. San Miguel and P.S. Sahni,
"Phase Transition an Critical Phenomena"
C. Domb and J.L. Lebowitz, Eds, A.P.N.T., 29 (1983).

145. J.S. Langer,
Physical Review A, VII No.4 1414 (1975).

146. G.R. Stroble,
Macromolecules, 18,558 (1985).

147. M.T. Shaw,
J. Appl. Poly. Sci., 18,449 (1974).

148. R. Casper and U. Marbitzer,
Macromol.Chem., 1,58,159 (1977).

149. A.F. Yee and M.A. Maxwell,
J. Macro. Sci. Phys., 17,543 (1980).

150. A.C.Fernandes, J.C. Barlow and D.R. Paul,
Polymer, 27,1789 (1986).

151. M.G. Brereton. et al,
J. Chem. Phys., 87(10),6144 (1987).

152. Eur. Pat. Appl., EP 37,181 (1981)
ICI plc inv. A.B. Newton,
Chem.Abstr., 96,7553 (1982).

153. Jpn. 8235906 (1982), Kararay Co. Ltd.,
A. Suenka, Y. Hamatoto.,
Chem. Abstr., 97,25085 (1982).

154. B.Singh,
PhD. Thesis, Imperial College, 1985.

155. S.T. Wellinghoff, J.L. Koenig and E. Bare,
J. Polym. Sci., Polym. Phys. Ed., V15,1913 (1977).

156. T.E. Schinchtel and K. Binder,
In Press.

157. E.J. Kramer, P.F. Green and C.J. Palmstrom,
Polymer, 25,473 (1984).

158. U. Murschall, E.W. Fischer, et al,
Polym. Sci., Polym.Lett., 24,191 (1986).

159. R.J. Composto and E.J. Kramer et al,
Private Communication to Dr J.S. Higgins

160. W.W. Park, A.R. Cooper and A.H. Hener,
Scripta. Met., 9,321 (1975).

161. J.D. Hoffman and J.J. Weeks,
J. Res. Nat. Bur. Std., 66A,13 (1962).

162. E Martuscelli, M Pracella and Wang Ping Yue,
Polymer, 25, 1097 (1984).

163. B. Wunderlich, "Macromolecular Physics",
Vol. 3 "Crystal Melting", Applied Science, 1980.

164. P.B. Rim and J.P. Runt,
Macromolecules, 17,1520 (1984).

165. M. Avrami,
J. Chem. Phys., 8,212 (1941).

166. W.F. Sherman and G.R. Wilkson,
Adv. Infrared Raman Spectroscopy, (1980).

167. J.R. Ferraro,

"Vibrational spectroscopy at high external pressure", 1984.

168. C.E. Weir and G.R. Lippincott et al,

J. Res. Natl. Bur. Stand., Sec. A63 55 (1959).

169. T.P. Shaw, B.A. Newman and V.D. Pae,

J. Material. Sci., 12,771 (1977).

170. H.D. Flack,

J. Polym. Sci., 10, A2,1799 (1972).

171. A.Van Valkenburg,

"High pressure measurements", Butterworth, London, 1963.

172. A. Van Valkenburg,

Ind. Diamond Rev. 24, Special Suppl., 17, (1964).

173. H.W. Davies,

J. Res. Natl. Bur. Stand. Sect. A72, 149 (1968).

174. R.M. Hill and S.D. Christian,

Appl.Spectrosc., 36,302 (1982).

175. R.A. Forman, G.J. Piermarini and J.D. Barnett and S. Block,

Science 176, 284 (1972).

176. H.K. Mao and P.M. Bell,

Science, 191,851 (1976).

177. K.A. Goettel, H.K. Mao and P.M. Bell,

Rev. Sci.Instrum., 56 (7),1420 (1985).

178. (a) D.M. Adams and S.K. Sharma,

J. Chem. Soc. Faraday Transaction 2, 72,1344 (1976).

(b) D.M. Adams and S.K. Sharma,

J. Chem. Soc. Faraday Trans., 2, 72,848 (1976).

179. B.M. Riggleman and H.G. Drickamar,
J. Chem. Phys. 38,2721 (1963).

180. R.N. Schock and S. Katz,
J. Chem. Phys., 48,2094 (1968).

181. D.L. Dekker,
J. Appl. Phys. 36,157 (1965).

182. W.Guo,
PhD First Year Report, Imperial College, March 1987.